

Valentin Url, BSc

Graz University of Technology

Methods for Morphing Human Body Models

MASTER'S THESIS to achieve the university degree of
Master of Engineering

Master's Degree Program:

Submitted to

Graz University of Technology

Reviewer: Univ.-Prof. Dipl.-Ing. Dr.techn. Hermann Steffan

Supervisor: Dipl.-Ing. Felix Ressi, BSc

Vehicle Safety Institute

Graz, May 2022

AFFIDAVIT

I declare that I have authored this thesis independently, that I have not used other than the declared sources/resources, and that I have explicitly marked all material which has been quoted either literally or by content from the used sources. The text document uploaded to TUGRAZonline is identical to the present master's thesis.

Graz, _____

Signature

DANKSAGUNG

Zu Beginn möchte ich mich bei Dipl.-Ing. Felix Ressi für die Betreuung während meiner Masterarbeit bedanken. Durch sein Fachwissen und seine konstruktive Kritik hat er mich bei der Erstellung meiner Arbeit wesentlich unterstützt. Des Weiteren gilt mein besonderer Dank allen Kolleginnen und Kollegen am Institut für Fahrzeugsicherheit, die mir im Laufe meiner Arbeit durch ihre Ratschläge und Anmerkungen sowie bei Fragen zur Seite gestanden sind.

Außerdem möchte ich mich für die langjährige Unterstützung bei meiner Familie bedanken. Vor allem bei meinen Eltern, die mir das Studium ermöglicht haben und jederzeit ein offenes Ohr für mich hatten.

Bei meinen Freunden und Kommilitonen möchte ich mich ebenfalls für deren Unterstützung während meines Studiums bedanken. Im Besonderen bei Jasmin Loris, Markus Koch, Maximilian Hribernig und Thomas Schrammel, die mich schon seit vielen Jahren auf meinem Weg begleiten und auf die ich mich stets verlassen kann.

Valentin Url

Graz, 17.05.2022

ABSTRACT

Nowadays, the main testing device to assess and compare occupant safety in passenger cars are crash test dummies. In addition to physical testing, simulations with finite element human body models are also performed. For this purpose, virtual human models are used together with virtual vehicle models in finite element simulations. The human body models needed for these simulations can be positioned in different ways. On the one hand, they can be transferred into the desired position from existing models with the help of positioning simulations. On the other hand, they can be created by means of geometric interpolation starting from a baseline model. This is done by a purely geometric manipulation of the model. This interpolation, the so-called called morphing, allows not only a change of the body posture but also a change of the anthropometry of the baseline model to represent a wider range of the population. In this thesis work, morphing approaches for virtual human models were investigated. The VIVA+ finite element model of version 0.3.0 should be positionable analogous to the already positioned models of the previous generation 0.2.5. For this purpose, a morphing script was created using Python. The interpolation using landmark-based radial basis function turned out to be well suited. In contrast, interpolation using free form deformation or inverse distance weighting turned out to be unsuitable.

The computational time for morphing was significantly reduced compared to positioning simulations. However, the model quality of the models created by morphing could not match that of conventionally positioned models. The number of solid elements with total or partial negative volume was consistently higher in them. The mesh quality of the morphed models was compared to that of the respective baseline model and the conventionally positioned model. Specifically, the aspect ratio, skewness, Jacobian deviation, warping and internal element angle were chosen as criteria for the comparison. Using these criteria to assess mesh quality, the conventionally positioned models also outperformed the morphed models. It was found that the quality of the morphed model was often better when there were no large differences in body posture between baseline and target model. Intersections and initial penetrations were observed for both, the models positioned via simulations and via morphing, which currently has to be corrected manually. In the future, this could be additionally implemented into the python script. For this, however, information about node affiliation to different parts would have to be known in the Python script. If node affiliation were known, this could also be used to perform a volume check. This would allow solid elements with negative volume to be corrected subsequently.

TABLE OF CONTENTS

1	INTRODUCTION	1
1.1	Motivation	5
1.2	Overview of current human body models	6
1.3	Review of literature	7
1.4	VIVA+ Human Body Model	9
1.5	Objectives	17
2	METHOD	18
2.1	Integration of the VIVA+ model	22
2.2	Calculations for the transformation	23
2.3	Applying transformation from version 0.2.5	35
2.4	Calculating the transformation directly in version 0.3.0	39
3	RESULTS	42
3.1	Comparison to initial model	46
3.2	Comparison of different positions and body proportions	58
3.3	Use of different PC systems	63
4	DISCUSSION	65
4.1	Intrusions, mesh quality and elements with negative volume	66
4.2	Limitations and outlook	70
5	CONCLUSIONS	75
6	REFERENCES	76
A	APPENDIX	1
A.1	Node sets and landmarks for morphing	2

A.2 Detailed morphing results	6
--------------------------------------	----------

LIST OF FIGURES

Figure 1: VIVA+ Model Family (VIVA+, 2021)	9
Figure 2: File structure VIVA+ (VIVA+, 2021)	10
Figure 3: Cortical femur head	11
Figure 4: Detailed femur head with removed elements and visible nodes	12
Figure 5: Shell element quality criteria (BETA CAE Systems, 2021)	13
Figure 6: Solid element quality criteria (BETA CAE Systems, 2021)	14
Figure 7: LS-DYNA keyword structure for nodes.....	15
Figure 8: LS-DYNA keyword for shell elements	15
Figure 9: LS-DYNA keyword for solid elements	16
Figure 10: LS-DYNA keyword for node set	16
Figure 11: Models used in the Python script	18
Figure 12: Overview of body regions	21
Figure 13: Relevant include files	22
Figure 14: General morphing process	26
Figure 15: Landmarks with associated node set	27
Figure 16: Using the free form deformation on femur head	28
Figure 17: Baseline and CT image femur head.....	29
Figure 18: Femur head morphing using IDW and power=0	30
Figure 19: Model comparison approach in chapter 3.1	33
Figure 20: Model comparison approach in chapter 3.2	34
Figure 21: Scheme - Transformation from 0.2.5	35
Figure 22: Exemplary representation le. femur	36
Figure 23: Exemplary representation le. femur - detailed	37
Figure 24: Scheme - Transformation from 0.3.0	39
Figure 25: Previously morphed nodes on the left thigh.....	40
Figure 26: Results from first approach on femur head 1/2.....	43
Figure 27: Results from first approach on femur head 2/2.....	45
Figure 28: Baseline models of v. 0.3.0	46
Figure 29: Morphing the 50F standing baseline model	47
Figure 30: Morphed 50F standing to 50M standing and 50F TB024 pedestrian.....	48
Figure 31: Morphed 50F standing to 50F cyclist left leg down	48
Figure 32: Morphing the 50F seated baseline model	49
Figure 33: Morphed 50F seated to 50F cyclist left leg down	50
Figure 34: Morphed 50F seated to 50F TB024 pedestrian.....	50
Figure 35: Morphed 50F seated to 50F standing	51
Figure 36: Morphing the 50M standing baseline model.....	52

Figure 37: Morphed 50M standing to 50F standing.....	53
Figure 38: Morphed 50M standing to 50M TB024 pedestrian	53
Figure 39: Morphed 50M standing to 50M cyclist left leg down	54
Figure 40: Morphing the 50M seated baseline model	55
Figure 41: Morphed 50M seated to 50F seated.....	56
Figure 42: Morphed 50M seated to 50M TB024 pedestrian	56
Figure 43: Morphed 50M seated to 50M cyclist left leg down	57
Figure 44: Comparison of morphed 50F cyclist model with regards to baseline models	59
Figure 45: Comparison of morphed 50F TB024 model with regards to baseline models	60
Figure 46: Comparison of morphed 50M cyclist model with regards to baseline models.....	61
Figure 47: Comparison of morphed 50M TB024 model with regards to baseline models	62
Figure 48: Mesh quality of 50F cyclist with left leg down	66
Figure 49: Mesh quality of 50F TB024 pedestrian	67
Figure 50: Solid elements with total/partial negative volume in 50F cyclist left leg down	68
Figure 51: Initial penetrations in the morphed left leg down cyclist position of 50F (a) and 50M (b)	68
Figure 52: Morphed 50F TB024 pedestrian from 50F seated and standing baseline models.....	69
Figure 53: Mass difference compared to conventional positioned model	72

LIST OF TABLES

Table 1: Overview of currant human body models	6
Table 2: Morphing order of independent body parts	20
Table 3: Morphing order of dependent body parts	21
Table 4: Implemented basis functions from PyGeM	25
Table 5: Selected basis function	26
Table 6: Femur mesh quality criteria - VIVA+ (VIVA+, 2022)	29
Table 7: Mesh quality criteria for comparison	32
Table 8: Parts that apply a transformation from v. 0.2.5	38
Table 9: Apply a calculated transformation from v. 0.2.5 to v. 0.3.0 in upper body skin	38
Table 10: Parts that calculate a transformation directly in v. 0.3.0	41
Table 11: Transformation for v. 0.3.0 from prev. morphed nodes in head and neck	41
Table 12: PC systems for comparison	63
Table 13: Results from several morphing passes	63
Table 14: Results using different cluster configurations	64

1 INTRODUCTION

As shown from WHO (2018) the cause of death from traffic crashes is the 8th leading cause of death worldwide with 1.35 million deaths per year. Although the number of fatalities per 100,000 population remains at a relatively constant level, the absolute number of fatalities caused by traffic accidents is steadily increasing worldwide. This is due to steadily increasing world population figures, rising social status and the associated individual mobility.

With the aim to enable safe traffic, an interaction of safe road and roadsides, vehicles, speed and road users is essential. In addition to improved driver training and safe road conditions, which should in principle prevent a vehicle crash, accident avoidance measures that a vehicle can take itself to avoid an accident (active vehicle safety), there are also important measures to reduce the consequences of an unavoidable accident (passive vehicle safety). (*Safe System Principles | Road Safety Manual - World Road Association (PIARC), 2022*)

Legally prescribed tests for evaluating vehicle safety depend on the market in which the vehicle is to be sold. Examples include the Regulations of the United Nations Economic Commission for Europe (UN/ECE, Europe) and the Federal Motor Vehicle Safety Standards (US).

In these prescribed tests, an accident scenario and limits of certain injury criteria are specified. Anthropometric test devices (short ATDs or dummies) are used to record the loads that occur during the crash test. Examples of these scenarios are the Full-Width-Frontal (UN R137), the Offset-Frontal (UN R94), the Side-Barrier (UN R95) and the Side-Pole (UN R135) tests. In addition to the test scenarios for determining occupant safety, there are also tests for determining pedestrian safety, for example UN R127. All of these tests have their own test protocols that must be followed in order to receive approval. The exact positioning and data processing of the recorded data of the dummies is also precisely specified. (Economic Commission for Europe of the United Nations, 2011, 2012a, 2012b, 2015, 2020)

In addition to the legal requirements that must be met in order to obtain vehicle approval, there are also consumer information tests. These tests can be used by end customers to make decisions when buying a car.

Different investigations are made with the use of crash test dummies for consumer information by independent institutions, for example the European New Car Assessment Program (Euro NCAP). These crash test dummies are equipped with high-resolution sensors. They are used to record for example accelerations, displacements, forces and torques. The tests carried out are intended to reflect, in a simplified way, the road accidents that occur most frequently in real road traffic. For adult occupants, two anthropomorphies of dummies are currently mainly used for these tests. These are an average

male (which was originally based on a study by Schneider et al. (1983)) and an average female (*Protocols / Euro NCAP, 2022*). Typically, consumer tests have a lower threshold of injury criteria than the tests required by law. Based on the results, a vehicle rating is then created, which allows the customer to compare different vehicles. In addition, these consumer test institutes are often much more dynamic in terms of considering new scenarios than the legislator. As a result, consumer tests not only examine passive vehicle safety, but also focus on determining active vehicle safety. (*Euro NCAP / Roadmap 2025*)

In addition to the above-described evaluation of vehicle safety based on specific measured values during a crash test, further investigations were carried out based on real road traffic. Bose et al. (2011) have shown that the annual miles traveled by male drivers are 33% higher than by female drivers (for the year 2009). Although the accident frequency for female drivers is higher compared to male drivers, male drivers are exposed to a higher accident risk due to the higher mileage. However, due to changes in e.g. driver behavior and more and more kilometers driven by female drivers, the trend is that people of both sexes can be involved in an accident with similar probability. In the study mentioned above, however, it was shown that for female drivers the probability of a serious injury was about 47% higher than for a male driver in a comparable accident (both drivers were wearing seat belts). Due to these facts, special attention should be paid to ensure that restraint systems in vehicles (seat belts, airbags, ...) equally protect persons of both sexes. However, since these restraint systems have different effectiveness depending on body size, weight, body structure and other biological characteristics that differ between the sexes, as well as age, and the current systems have been adapted to the average male driver, the protective effect on female drivers is apparently not as high. (Bose et al., 2011)

Besides, Kullgren and Krafft (2010) also found that real-world rear-end crashes result in different whiplash injuries for female and male occupants. Consequently, devices designed to protect occupants from severe whiplash injury were more effective for men than for women. These devices were found to reduce the risk of severe whiplash injury for men by 60% and for women by 45%.

In Fu et al. (2021), differences in accident severity between male and female occupants were also considered. The main focus was on the change in accident risk for females in vehicles from 2003 onwards (from this year it became mandatory to have a female dummy occupant for frontal crash tests). Before 2003, female occupants were 40.9% more likely to be seriously injured than male occupants. For vehicles built from 2006 onward, the probability differed between male and female occupants by 17.2%. Consequently, an improvement in passive vehicle safety was found with respect to gender. However, the need for further improvement of female vehicle occupants was also pointed out. (Fu et al., 2021)

In fact, until 2003, only male anthropometry crash test dummies were used, even though it had been known since the 1980s that male and female vehicle occupants exhibit different behavior in a crash. However, the female dummy introduced afterwards was also only a scaled-down male dummy and could only represent the 5th percentile female (this is also used as a teenage dummy). Thus, there is still no dummy in use which represents actual differences in the biological physique of the two sexes. (Consumer Reports, 2019)

As Ressi et al. (2019) and Boin (2018) have shown, the restraint systems commonly used in vehicles today are designed for current standardized seating positions. As the level of automation of vehicles (self-driving vehicles) progresses, it is very likely that there will be new occupant seating positions for comfort reasons. The changed seating positions and the associated changed loads during various accident scenarios are critical to future vehicle safety. Consequently, physical anthropometric devices are also needed for these new types of load cases, which can determine the loads occurring in them. The problem is that the currently used dummies are only validated for specific load cases. For example, the 50th percentile male Hybrid III dummy is validated for the frontal crash. (National Highway Traffic Safety Administration, 2008) Also, the side-impact test dummy (World-SID) is validated to a lateral accident scenario (Hynd et al., 2004). Górnjak et al. (2022) also addressed the issue of non-validated ATDs for reclined seat settings deviating from the standard. In more detail, the seating position in a frontal accident was investigated. To test the influence of this modified seat configuration, a 50th percentile male Hybrid III dummy was used. The interactions at different crash pulses (3, 4 and 5 g) and backrest angles (110°, 130° and 145°) were investigated. Górnjak et al. (2022)

Another approach compared to physical testing using real crash tests, is the use of virtual human body models (HBM) in computer simulations. These models, created with the aid of computer-aided design (CAD) and finite element analysis (FEA), combined with a virtual vehicle model, allow a deeper insight into the injury process. Furthermore, it is possible to reduce the required physical tests and save costs. Currently, there are already several types of virtual models. When exemplarily looking at the available models from Humanetics, their already wide range becomes apparent. There are different types of models for frontal, side and rear impact assessment. Additionally, there are also models for occupants of automated vehicles and for children. Furthermore, finite element models are also available for representing a powered two-wheeler dummy and for pedestrian evaluations. Many of these models also exist as physical ATDs, but the future trend is clearly towards increased virtual testing. Accordingly, the availability of these physical test objects as virtual models is of great importance. (Humanetics, 2022). However, even the nowadays available models represent only a small portion of the real world population.

A special test method, which Euro NCAP is currently conducting with respect to virtual human models, is used to determine pedestrian safety. The simulation with a human body model is used to determine whether active safety measures for pedestrians may be activated or must remain deactivated for further tests of pedestrian safety. For this simulation, the HBM must be placed in a specified position. The specifications are given in Technical Bulletin 024 (short TB024) for Pedestrian Human Model Certification of Euro NCAP. The designation TB024 is used in the further course as pedestrian position. (Euro NCAP, 2021)

In contrast to the problems of the ATDs for application in non-conventional seating positions, the use of virtual human models seems promising. For example, the Total HUMAN Body Model for Safety (THUMS) has been validated by a large number of independent component tests (Kitagawa and Yasuki, 2014). Likewise, the model developed by the Global Human Body Models Consortium (GHBMC) has also been widely validated by independent component testing and can consequently be used in simulations for possible future accident scenarios. (Park et al., 2016)

Another point not to be neglected in connection with HBMs is that certain models have already implemented active muscle movement (Kimpura et al., 2016; Kato et al., 2018). These can be used in the pre-crash phase and in low acceleration maneuvers to better represent human behavior. This can result in a change in the occupant's body posture even before the initial impact. The reason for this is that the occupant can prepare for the accident. For example, the driver can try to avoid an obstacle by steering strongly, or he can try to avoid a collision by applying the brake and performing an emergency braking maneuver (Iwamoto et al., 2015). In Östmann and Jakobsson (2016), the combination of an active human body model with automatic brake assist and electric reversible seat belt pretensioner was investigated. A frontal accident with an initial speed of 64 km/h was simulated. The SAFER A-HBM of the 50th percentile male occupant was used as model. The automatic braking function reduced the initial speed once to 56 and once to 39 km/h. This resulted in occupant accelerations reduced by 15-45% and 60-70%, respectively, compared to the unbraked accident. The SAFER A-HBM was able to reproduce the pre-collision phase well due to the active muscle modeling. (Östmann and Jakobsson, 2016)

1.1 Motivation

Based on the literature reviewed above, different aspects of vehicle safety related to personal accidents can be identified. This applies not only to vehicle occupants (driver or passengers) but also to persons outside the vehicle, so-called vulnerable road users, or VRU for short (e.g. pedestrians, cyclists, powered two-wheelers). The increased focus on virtual testing (see also *Euro NCAP / Roadmap 2025*) and the associated virtual HBMs needed in the future mean that the handling of these HBMs is of great importance.

The creation of a new HBM is time-consuming. In order not to have to build a new one for every desired variant of this model a workaround is needed. Therefore, it would be time-saving to derive several desired models from one already created model. These can either have different postures or differ by altered anthropometry. The derivation from an existing model can be done in different ways. On the one hand, one can reposition the pose of the previously created model using a positioning simulation specifically used for this purpose (for an example see <http://www.piper-project.eu>). In this simulation approach, sometimes referred to as marionette method, the model is brought into the desired final position by the use of spring elements. However, if the pose is changed significantly, it may be necessary to split this positioning into several simulation steps to achieve the desired result. The creation and execution of these positioning simulations are relatively time-consuming. On the other hand, a derivation of the existing model can be performed by means of an approach called morphing. Different options can be used for this process. An interpolation by means of free form deformation (FFD), inverse distance weighting (IWD) or using a surface interpolation with landmark based radial basis function (RBF) are available. In this context, landmarks are known geometry points, that occur in both the base model and the targeted model. Morphing can therefore also be used to change the geometry of the base model. The usage of morphing for human body models was already shown in different studies (see chapter 1.3). A more detailed description of this procedure is given in chapter 2.2. Morphing allows the geometric manipulation to be theoretically very large without requiring an intermediate step. Since no finite element simulation is necessary, a time saving can be the result. However, both approaches may require manual rework. For these reasons, this master's thesis investigates possibilities to derive further virtual human models by the morphing procedure from an existing HBM.

1.2 Overview of current human body models

Today, there is already a wide range of virtual human models. For the most part, however, these only represent the same anthropometries as conventional crash test dummies. Table 1 shows an overview of a few currently available models, which are also referred to in the next section.

Table 1: Overview of current human body models

Name	Total Human Model for Safety (THUMS)			Global Human Body Models Consortium (GHBMC)	VIVA+
	THUMS v4	THUMS v5	THUMS v6		
Provided by	1			2	3
Size/sex	3YO, 6YO, 10YO, AF05, AM50, AM95	AF05, AM50, AM95	AF05, AM50, AM95	AF05, AM50, AM95, 6YO	AF50 (50F), AM50 (50M)
Position	Occupant/ Pedestrian	Occupant	Occupant	Occupant/ Pedestrian	Seated/ Standing
# of elements	approx. 1.9 million	approx. 285,000	approx. 1.9 million	from approx. 360,000 (simplified) to approx. 2.3 million (detailed) ⁴	approx. 769,000
# of nodes	approx. 762,000	approx. 185,000	approx. 766,000	from approx. 300,000 (simplified) to approx. 1.3 million (detailed) ⁴	approx. 535,000

¹ Toyota Motor Corporation & Toyota Central R&D Labs., Inc. Source of THUMS models: *THUMS | Toyota Motor Corporation* (2021).

² The Global Human Body Models Consortium consist of FCA US LLC, General Motors Holdings LLC, Honda R&D Co., Hyundai Motor Co., Nissan Motor Corp. Ltd., PSA Groupe, Renault s.a.s., and Joyson Safety Systems. Ford Motor Co., NHTSA (National Highway Transportation Safety Administration) and Autoliv Inc. Source of GHBMC: GHBMC (2022).

³ The VIVA+ Model was created as part of the VIRTUAL project (see <https://projectvirtual.eu>). Additional source of VIRTUAL project: Linder et al. (2020).

⁴ Decker, et al. (2018)

1.3 Review of literature

An early application of surface interpolation using the radial basis function (see chapter 2.2 equation (1)) was demonstrated by Carr et al. (1997). This involved using the radial basis function to produce cranial implants from computed tomography (CT) images. These implants were to be used to repair damage to the skull bone. Interpolation using RBF was used to map the transitions between the skull and the damaged areas. Subsequently, a plastic mold was created from this image using computer numeric controlled (CNC) milling. The implant was then formed from this mold and a thin titanium sheet in a hydraulic press. The computing power required to calculate this mathematical function was limited at the time. As a result, only fewer than 300 interpolation points could be calculated. (Carr et al., 1997)

Hwang et al. (2016) demonstrated the application of the morphing process with a human body model. The mid-sized-male of the THUMS 4.01 model family was used as the base model. The goal was to create new HBMs from the base model depending on desired age, body mass index, gender and posture. The entire morphing process took 2-3 hours and could be performed on a standard PC. The calculation of the transformation for mesh morphing was based on the radial basis function. This function calculated the transformation based on the change of so-called landmark nodes. These landmark nodes occur in the base model and in the target model. The target model consisted of statistical body surfaces and skeletons, which were subsequently merged. Finally, the base model was morphed into the target model using these landmarks and then the mesh quality was compared with that of the baseline model. Only a slight deterioration of the mesh quality was found. Special reference was made to the advantage of considerable time savings compared to the time-consuming creation of a new HBM. Finally, it was pointed out that in this study only the changed geometry due to age, sex, BMI and stature was considered. No influence of different materials or biologically dependent material properties was considered. It was also noted that the baseline model was only morphed into the driver position and that problems may arise if the geometry of the target position is very different from that of the baseline model. (Hwang et al., 2016)

Another use case of morphing was presented by Hu et al. (2016). The influence of size, age and BMI in a frontal accident was determined. The Global Human Body Models Consortium mid-sized-male model was used as the baseline model. Statistical models of skin and skeleton were used as targets. A total of 12 human body models were created using morphing. Height (1750 and 1880 mm), age (30 and 70 years) and BMI (25, 30 and 35) were varied. The morphed models were then integrated into a US NCAP crash simulation. This was used to simulate the 35 mph frontal crash with a generic vehicle interior on a sled. Head injury criterion (HIC), chest deflection, neck force, and femur force values were evaluated from each run. It was also pointed out that the morphing process only takes into account the geometric influences from age, body size, BMI and gender and not the changes in materials. (Hu et al., 2016)

Hu et al. (2019) considered 100 frontal occupant crash simulations intended to represent the real-world U.S. adult population. The FE model used was the medium height male occupant simplified version (M50-OS) from Global Human Body Models Consortium. This was morphed to a total of 100 individuals based on different age, gender body type and body mass index. For this, a 3D interpolation using the radial basis function was used, which could perform the morphing process on a conventional computer in about 10 minutes per model. For this landmark based process, statistical target models for thorax, pelvis, femur, tibia and outer body contour were used. The morphed models were positioned in a vehicle model as the driver and a US NCAP frontal crash was simulated. Head Injury Criterion, Brain Injury Criterion (BrIC), neck force, chest deflection and femur force were determined as relevant injury criteria. Different correlations were found. For example, lighter and heavier individuals experienced a higher HIC than medium occupants. Another finding was that female occupants were at higher risk of chest injury and also exhibited a greater aging influence compared to male occupants. (Hu et al., 2019)

1.4 VIVA+ Human Body Model

The virtual human body model used for this master's thesis is the VIVA+ model. It was developed within the VIRTUAL project and is subject to the LGPL v3 license terms. This means that the model is available free of charge and users are also able to modify the model as they wish.

The virtual human model is built from finite elements (FE) accordingly it is also called FE model. The elements are again built up by nodes and can be assigned to a specific component/part. The part definition also contains information about section and material. Furthermore, several parts can be assigned to one body region and this procedure enables a clear model structure.

The VIVA+ model family consists of the 50th percentile male (50M) and 50th percentile female (50F), each in sitting and standing position, where all models are derived from the sitting 50th percentile female. Figure 1 shows the current VIVA+ model family in which the model of the standing male is not shown. The derived models consist of the same parts as the baseline model, but the nodes of the parts are in different positions.

The creation process of the models, as well as the kinetic and kinematic response to blunt impacts, was described by John et al. (2022). The occupant model and the standing model were used for this purpose. Frontal, lateral and rear impact directions were investigated.

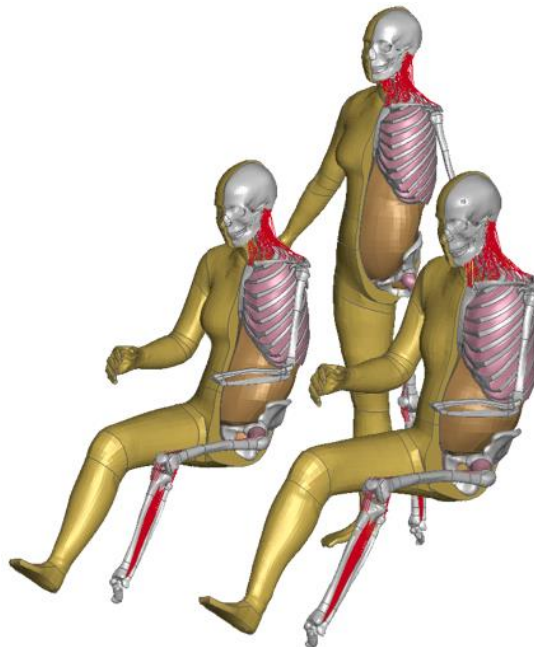


Figure 1: VIVA+ Model Family (VIVA+, 2021)

In order to be able to use information from the VIVA+ model in this work, the file structure of the model is essential. Figure 2 shows a schematic representation of the data structure. It can be seen that the model is built up via a main file and several include files. (VIVA+, 2021)

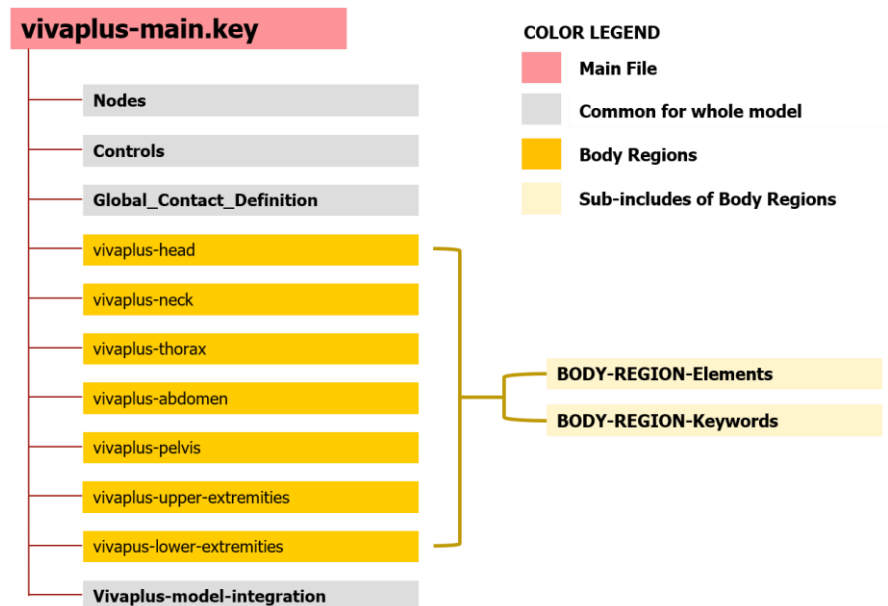


Figure 2: File structure VIVA+ (VIVA+, 2021)

Currently there are two model versions of the VIVA+ model family with the designations version 0.2.5 and version 0.3.0. Thereby v. 0.3.0 is a revised and partly extended version of v. 0.2.5. Both of them have the same model file structure. The models of the VIVA+ model series were created using LS-DYNA commands. The finite element solver LS-DYNA is used for simulations of problems in different application areas. These can be linear or non-linear, static or dynamic. It is also capable of performing implicit and explicit simulations (Ansys LS DYNA, 2022).

Although there are individual include files for the different body regions, all nodes of the entire model are in a common file called 'Nodes'. The advantage of this is that it prevents having to manage nodes across several files, and facilitates editing the nodes (e.g. for positioning) separately.

With respect to be able to calculate and apply the transformation in the next section, a short explanation about the structure of some parts is given here. The upper part of the right femur bone will be used as an example. Therefore, Figure 3 comes from the standing 50F model of v. 0.3.0. In it, the external parts of the femoral head are visible. A more detailed view showing the individual elements and their defining nodes is shown in Figure 4. Figure 3 shows the anterior view (a) and the posterior view (b) of the proximal part of the femur. The differently coloured areas of the bone represent different parts of which it is composed. In both images, only those parts that lie on the surface (cortical bone) are visible.

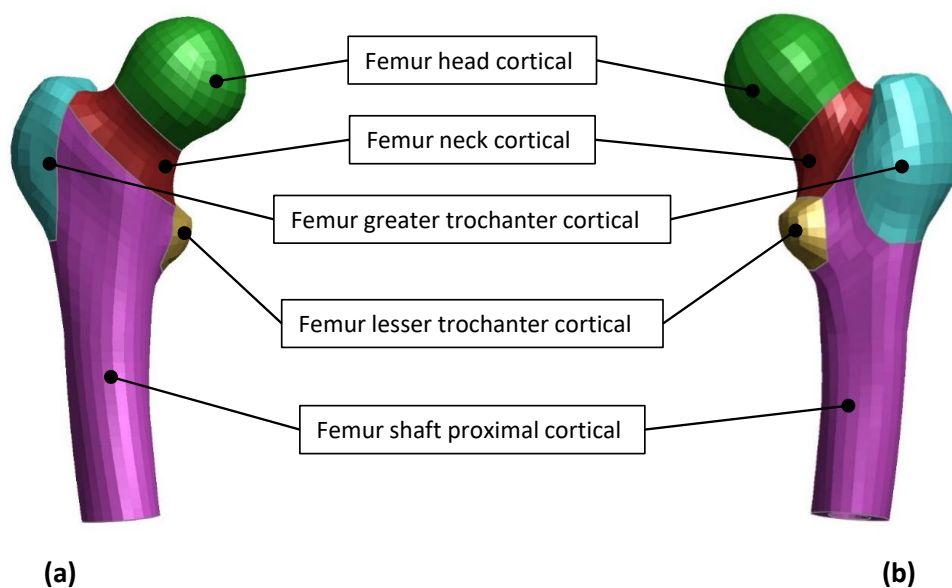


Figure 3: Cortical femur head

As can be seen from this, the femur is not made up of a single part, but of several. Similar to the cortical bone portions shown above, the bone portions that are not at the surface (trabecular bone portions) are also modelled as separate parts. The different parts of the cortical and trabecular bone can have different layer thicknesses and materials, as they are defined as individually.

As can already be recognized to some extent in the figure above, a grid can be seen on the surface of the parts. This grid is also called mesh or FE mesh. Each of these grid elements (or short elements) is built from its vertices. Depending on the element type, two-dimensional (2D) and three-dimensional (3D) elements are distinguished.

Figure 4 shows a three-dimensional view of the femur bone (cortical and trabecular). In it, the mesh is clearly drawn. In addition, a few elements (cuboidal in this case) have been hidden to show the buildup of the parts into the depths. In it, the outermost layer of the elements of the femur shaft can be seen in magenta, the second layer in blue, and the innermost layer in yellow.

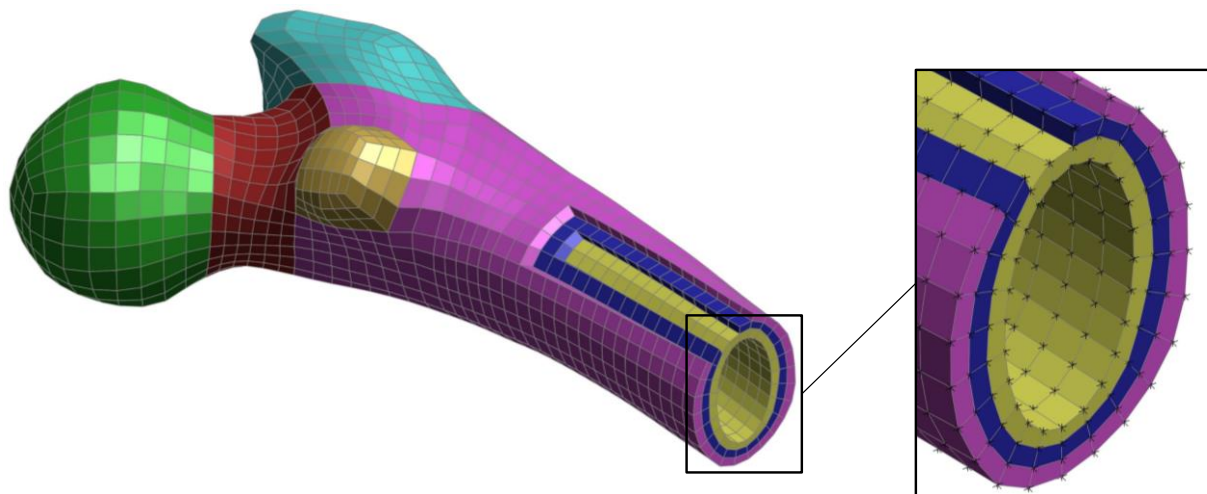


Figure 4: Detailed femur head with removed elements and visible nodes

When enlarging the image and visualising the nodes, the structure of the elements can clearly be recognized. This is shown in Figure 4 on the right-hand side. It is shown that the vertices are defined by nodes (in the figure the nodes are marked with an asterisk). It is also visible that some nodes are used for more than one element at the same time. For example, nodes between the innermost and middle layers are used to define elements from both layers. The result is that when the location of one of these nodes is changed, not only one element is modified, but possibly several. This also applies to the transition between two or more parts. If a node is located exactly at the transition between different parts, not only elements of one part are changed, but possibly also elements of several parts.

After the visualization from the large parts to the elements building them has been carried out so far, a more detailed consideration of the elements themselves will take place here. Depending on the element used, they can be further described with certain quality criteria. The criteria for the description of the FE mesh are different for solid and shell elements. These element types will be described later with their respective LS-DYNA keyword. The FE pre-processor software 'ANSA v21' was used for the recording of certain criteria (see also <https://www.beta-cae.com>). The included function of the 'Deck Report' allowed a clear and complete recording of all elements with additional information regarding their criteria. The element criteria can be defined manually and elements that do not meet the quality criteria are further referred to as 'OFF - elements' (solids-off and shells-off).

The quality criteria listed here were used in the rest of the work. They were used to evaluate the morphing quality and to compare models with each other.

Figure 5 shows the following shell element criteria: Aspect Ratio (a), Skewness (b), Jacobian Deviation (c), Warping (d) and Angle (e).

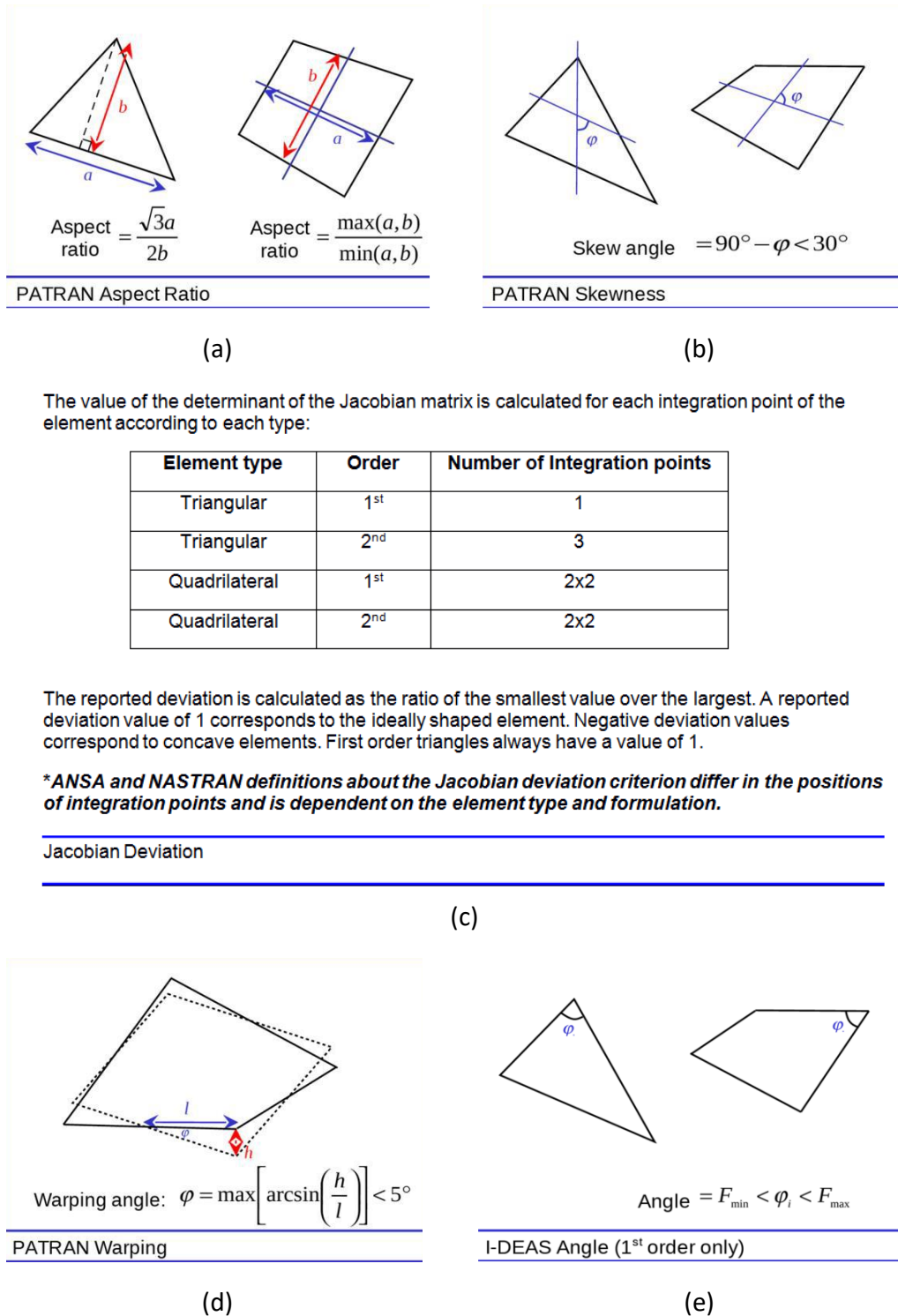
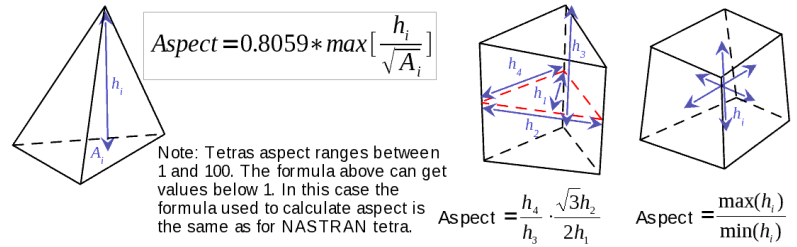


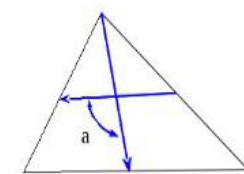
Figure 5: Shell element quality criteria (BETA CAE Systems, 2021)

Figure 6 shows the following solid element criteria: Aspect Ratio (a), Skewness (b), Jacobian Deviation (c), Warping (d) and Angle (e).



PATRAN Aspect

(a)



$$Skew = 90^\circ - a$$

PATRAN Skewness calculates each solid facet with the shells PATRAN calculation method and keeps the worst value.

PATRAN Skewness

(b)

The value of the determinant of the Jacobian matrix is calculated for each integration point of the element according to each type:

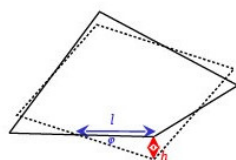
Element type	Order	Number of Integration points
Tetrahedral	1 st	1
Tetrahedral	2 nd	4
Pentahedral	1 st	3x2
Pentahedral	2 nd	3x2
Hexahedral	1 st	2x2x2
Hexahedral	2 nd	2x2x2

The reported deviation is calculated as the ratio of the smallest value over the largest. A reported deviation value of 1 corresponds to the ideally shaped element. Negative deviation values correspond to concave elements. First order triangles always have a value of 1.

**ANSA and NASTRAN definitions about the Jacobian deviation criterion differ in the positions of integration points and is dependent on the element type and formulation.*

Jacobian Deviation

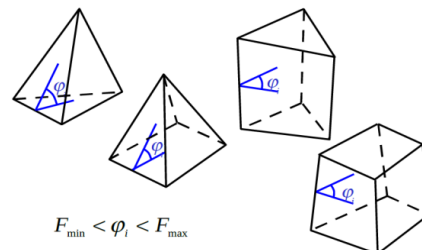
(c)



$$\text{Warping angle: } \varphi = \max \left[\arcsin \left(\frac{h}{l} \right) \right] < 5^\circ$$

PATRAN Warping

(d)



ABAQUS Angle – applicable to 1st and 2nd

(e)

Figure 6: Solid element quality criteria (BETA CAE Systems, 2021)

As already briefly noted above, the model was built to be used with LS-DYNA. Here an overview of a few of the commands, referred to as keywords, in order to understand their meaning is given.

The definitions of the nodes were made with the LS-DYNA keyword `*NODE`. It is structured the following way. Each node has a unique seven-digit node identification number (abbreviation: NID) and the X, Y and Z coordinates defining the node. Figure 7 shows the schematic structure of this function (Livermore Software Technology Corporation, 2016).

LS-Dyna keyword	unique node-ID	x-, y- and z-coordinates		
<code>*NODE</code>				
	1090000	58.754	0.	1512.844
	1100000	66.68	-63.4870.	1481.807

Figure 7: LS-DYNA keyword structure for nodes

A uniquely assigned NID is not only important for the FE model to be consistent, but also because it allows each node in the Python script of this master's thesis to be identified and its coordinates to be changed. In addition, this ID is also used to define elements. Furthermore, the nodes are assigned to so-called node sets by means of the NID, which will be described in more detail later.

The next command is used to create elements. Depending on the type of the desired element, different commands are available. Only the relevant ones for creating shells and solid elements are shown here. However, the general structure of this command type is always the same. Each element must be assigned a unique element ID (short EID). In addition, the element must be assigned to a part – this is done by entering the part ID. Finally, the nodes defining the element are specified using their corresponding node IDs.

Shell elements can consist of three or four nodes. In addition, it is also possible to build shell elements from six or eight nodes, but these do not occur in the VIVA+ model. The keyword is called `*ELEMENT_SHELL` and the structure of it can be seen in Figure 8 (Livermore Software Technology Corporation, 2016).

LS-Dyna keyword	unique element-ID	assigned part-ID	IDs of the defining Nodes	
<code>*ELEMENT_SHELL</code>				
	1100009	103002	1117661	1117663 1117662 1116965

Figure 8: LS-DYNA keyword for shell elements

Three-dimensional solid elements can consist of four (tetrahedron) or eight (hexahedron) nodes. The keyword is called `*ELEMENT_SOLID` and it is shown in Figure 9 (Livermore Software Technology Corporation, 2016).

LS-Dyna keyword	unique element-ID	assigned part-ID										
<code>*ELEMENT_SOLID</code>												
	1100011	103001										
	1105349		1105351	1105361	1105362	1100000	1100002	1117868	1117869	0	0	

Figure 9: LS-DYNA keyword for solid elements

Another important keyword that is relevant for this thesis is used to create so-called node sets. The node sets generated in the process have the following structure. They consist of a uniquely assigned set ID (seven digits, abbreviation: SID), a self-assigned title and the node IDs added to the set. The node sets were created using the LS-Dyna keyword `*SET_NODE_LIST_TITLE`, the structure is shown in Figure 10 (Livermore Software Technology Corporation, 2016).

LS-Dyna keyword	given set-name	unique set-ID	IDs of the included Nodes							
<code>*SET_NODE_LIST_TITLE</code>										
	femur_r_surface									
		2100511	0.0	0.0	0.0	0.0				
			7263478	7136559	7258935	7136562	7258150	7259184	7144734	7144736
			7158111	7136560	7136560	7136563	7258140	7259187	7144735	7144737

Figure 10: LS-DYNA keyword for node set

Only the node IDs are stored in the node set as shown. It does not contain any information about their coordinates. The advantage of using node sets is that once they have been created, all the nodes they contain can easily be processed together. For example, they can be assigned to rigid bodies or used for contact definition.

1.5 Objectives

As briefly mentioned in chapter 1.1, the handling of an HBM is already very important and will become even more important in the future. For this reason, the aim of this master's thesis is to investigate possible ways of model maintenance of the VIVA+ model. In particular, the processing of the model generation v. 0.3.0 is to be facilitated. For this purpose, a Python code is to be created which, utilizing the already pre-positioned models from generation v. 0.2.5, can also morph the new model into these final positions. Possibilities and limitation of the morphing process should be revealed. Furthermore, a comparison of the morphed model to the base model regarding the element quality should be established. In addition, the morphing process should be evaluated in contrast to conventional positioning options and a comparison in terms of computation time, workload and manual rework should be made.

This leads to the following specific research questions:

- How can morphing based on previously positioned model versions be used for model maintenance?
- What differences can arise between morphed models and conventionally positioned models in terms of model quality, computation time and manual pre- and post-processing?
- What are the possibilities and limitations of model processing using morphing?

2 METHOD

To change the geometry of the baseline model, a Python script was created that changes the node coordinates using a morphing process. The Python script was built on several steps and works with information from three models. The baseline model (Figure 11 a) and the target model (Figure 11 b) of the model version 0.2.5 and the baseline model of the HBM v. 0.3.0 (Figure 11 c). The aim was to morph the baseline model of version 0.3.0 using the target model of the previous model generation. In Figure 11, for example, the baseline model is the 50th percentile female seated (50F seated) and the target is the 50th percentile female in the cyclist position with left leg down (50F cyclist l down). The Python script has been uploaded to the TUGraz GitLab server and can be found at <https://gitlab.tugraz.at/vsi-all/hbm-morphing>.





Model version 0.2.5	Baseline (a) 	Target (b) 
Model version 0.3.0	Baseline (c) 	Morphed 

Figure 11: Models used in the Python script

First of all, the node files of the three models are read in. Then the nodes are read from the include file of the node sets from the base model and from the target model of the previous model generation. From these nodes (in the following called landmarks) the transformation between baseline and target is calculated using the radial basis function. In the last step, the calculated transformation is applied to the corresponding nodes of the model of the new model generation.

This way, the skin and skeleton are morphed according to the transformations based on the models of v. 0.2.5. Since the number of parts located between bone and skin (e.g. soft tissue) differs in the model versions, they are subsequently morphed only between the already morphed nodes.

The processing of the data in the Python script is mainly done by arrays, which were created with the help of the NumPy Python package (*NumPy*, 2022). The calculation of the transformation, in particular the calculation of the radial basis function, is carried out with the help of the PyGeM Python package (*PyGeM 2.0.3 documentation*, 2021). The Python library Matplotlib (*Matplotlib — Visualization with Python*, 2022) was used to display the diagrams.

The following Table 2 shows the morphing sequence of independent body parts and Table 3 shows the morphing order of dependent body parts. The coloured fields represent the different body parts. The colour scheme is chosen to match the colouring in chapter 2.3 and chapter 2.4 for a better overview. The numbering of the body parts shows the rough order. Each body part consists of one or more parts, which in turn are morphed in the order shown. The only requirement of the independent body parts is that the skin of the upper body is morphed first, as this is used in the further course or transitions to the outer body parts are taken into account.

The order of the remaining regions (number 2 to number 8) is not mandatory. However, this order was defined in the Python script. It is also assumed that all independent body parts have been morphed before the remaining two steps (pelvis and remaining torso) can be performed.

Table 2: Morphing order of independent body parts

1. Upper Body Skin	1. Head and neck skin 2. Torso skin (Thorax, Abdomen, Pelvis)				
2. Head and Neck	1. Head bones 2. Remaining head 3. Neck bones 4. Remaining neck	3. Right leg	1. Femur r. 2. Leg skin r. 3. Foot with lower part of Tibia and Fibula r. 4. Fibula head r. 5. Fibula r. 6. Tibia head r. 7. Tibia r. 8. Patella r. 9. Soft tissue ankle r. 10. Soft tissue knee r. 11. Remaining lower leg r. 12. Remaining upper leg r.	4. Left leg	1. Femur l. 2. Leg skin l. 3. Foot with lower part of Tibia and Fibula l. 4. Fibula head l. 5. Fibula l. 6. Tibia head l. 7. Tibia l. 8. Patella l. 9. Soft tissue ankle l. 10. Soft tissue knee l. 11. Remaining lower leg l. 12. Remaining upper leg l.
5. Right arm	1. Arm skin r. 2. Remaining arm skin – torso connect r. 3. Clavicle, Scapula r. 4. Humerus r. 5. Ulna, Radius r. 6. Hand r. 7. Remaining arm r.	6. Left arm	1. Arm skin l. 2. Remaining arm skin – torso connect l. 3. Clavicle, Scapula l. 4. Humerus l. 5. Ulna, Radius l. 6. Hand l. 7. Remaining arm l.	7. Thorax	1. Thorax vertebra bones 2. Right R1 to R6 rib bones 3. Right R7 to T12 rib bones 4. Left R1 to R6 rib bones 5. Left R7 to T12 rib bones 6. Sternum bones 7. Ribcage external r. 8. Ribcage external l. 9. Intercostal muscles r. 10. Intercostal muscles l.
8. Abdomen	1. Abdomen vertebra bones				

As noted, the morphing steps listed in Table 3 cannot be performed until the eight body regions listed above have been completed. This is because different parts from different regions come together in these areas. For this, all nodes that have already been morphed before must be taken into account. Additionally, the pelvis must be completed before the morphing of the remaining Torso can start.

Table 3: Morphing order of dependent body parts

9. Pelvis	<ol style="list-style-type: none"> 1. Pelvis bones r. 2. Pelvis bones l. 3. Pelvic cavity 4. Hip ligament r. 5. Pelvic connect tissue r. 6. Hip ligament l. 7. Pelvic connect tissue l. 8. Pelvic soft tissue internals r. 9. Pelvic soft tissue internals l. 10. Pelvic soft tissue r. 11. Pelvic soft tissue l. 	10. Remaining Torso	<ol style="list-style-type: none"> 1. Thorax soft tissue r. 2. Thorax soft tissue l. 3. Abdomen cavity l. 4. Abdomen cavity r.
--------------	--	---------------------------	--

It should also be noted that although in the tables above a distribution of the morphing steps to exact parts is written, this is not implemented in reality. This is due to the fact that, as was already shown in chapter 1.4, some nodes can be assigned not only to one element, but to several. As a consequence, these elements can be assigned not only to a single part, but to several. For this reason, a sharp border between the body regions is not always possible. Consequently, nodes that actually belong to two different parts are morphed with the part that occurs first in the sequence. When these nodes have been morphed, they are not modified any more.

Figure 12 also shows the affiliation of the parts to the body regions listed above. On the left side (a), the skin parts originating from the respective region are visible. In the middle view (b), the skin parts have been hidden and the tissue that lies underneath is visible. On the right side (c), the tissue has also been hidden and the body structures underneath are revealed. The color scheme used is the same as the one introduced above.

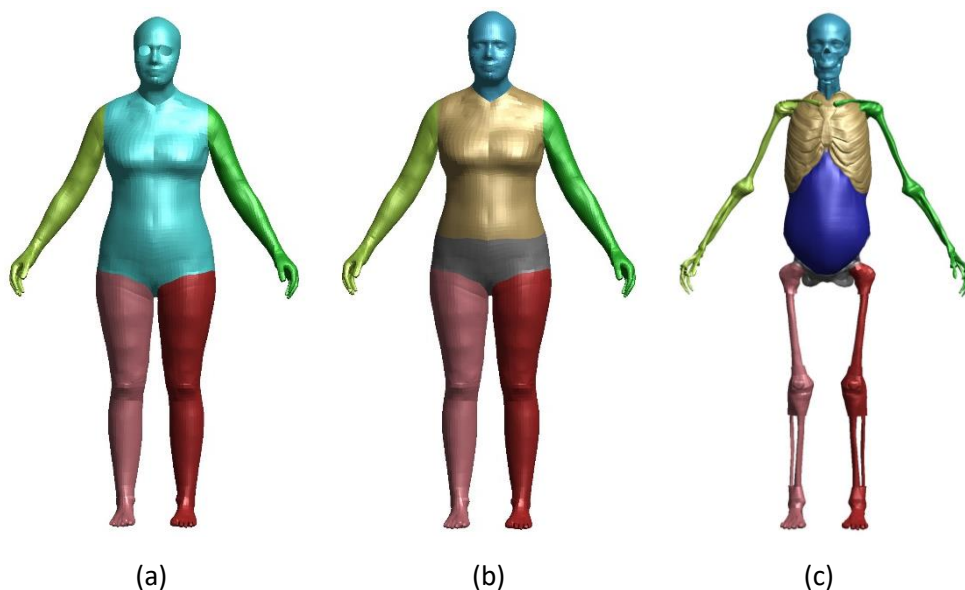


Figure 12: Overview of body regions

2.1 Integration of the VIVA+ model

Based on the data structure of the VIVA+ model presented in chapter 1.4, a Python script for the manipulation of the node coordinates was created. To access the nodes from the model that are needed for the script and to process them, two include files are essential: the original include file **nodes** and the include file **node-sets** that was created in the course of this work. The two relevant include files are highlighted in green in Figure 13. Also the newly created include file with the node sets was attached to the main file and is framed in red in Figure 13.

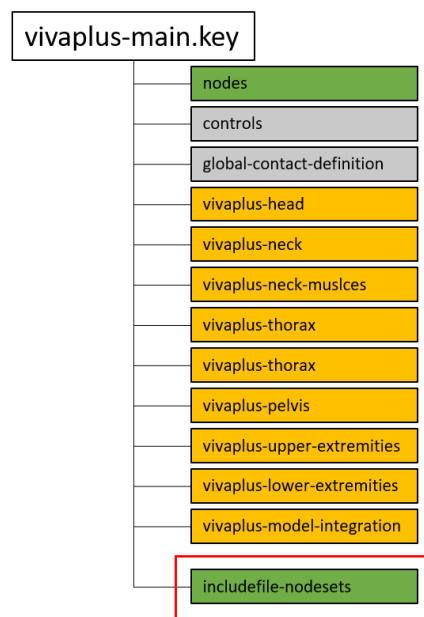


Figure 13: Relevant include files

In the first step, node sets for both model versions of the HBM were created in an FE pre-processor. The pre-processor 'Primer v.18.0' (<https://www.oasys-software.com/dyna/software/primer>) was used for this purpose. This resulted in a number of 63 sets in v. 0.2.5 and a number of 72 sets in v. 0.3.0. It should be noted that only the nodes with their corresponding coordinates are used for morphing. This means that only the geometry of the parts is changed. The material or the material properties are not changed by the morphing process. Likewise, no changes are made to the part section definition or the element definitions. No information about related nodes is used either. Since there is no assignment of the nodes to parts or elements, no contact conditions are considered during morphing. So only a geometrical manipulation of the node coordinates is performed. This also changes the geometry of the associated elements and parts.

2.2 Calculations for the transformation

For this work, an interpolation of nodal coordinates using the radial basis function was performed. This type of interpolation is already well described in the literature (see Carr et al., 1997). In addition, it has also been used for similar use cases. As already shown in chapter 1.3, Hwang et al. (2016) used it to quickly derive different models from a baseline model. The HBM THUMS 4.1 was used for this purpose. Also, Hu et al. (2016) considered the influence of height, age and BMI in frontal crashes and therefore morphed the GHBM mid-sized-male model. In addition, Hu et al. (2019) simulated 100 crashes with occupants of the real US population using surface interpolation with the radial basis function on the GHBM simplified male occupant model (M50-OS). Based on the literature sources mentioned above, an overview of the interpolation process using the radial basis function is given here.

$$s(x) = p(x) + \sum_{i=1}^n \lambda_i * \varphi * (||x - x_i||) \quad (1)$$

$s(x)$ radial basis function

$p(x)$low order polynomial

λ_iweighting coefficient

φ basis function

$|x-x_i|$... Euclidean distance between x and x_i

Equation (1) shows the general structure of the radial basis function. In it, $p(x)$ is a low order polynomial, λ is the weighting coefficient, φ is the basis function. In addition, the Euclidean distance is considered, which in this case represents the three-dimensional distance between two points and is calculated using equation (2).

$$r_{ij} = \sqrt{(x_i - x_j)^2 + (y_i - y_j)^2 + (z_i - z_j)^2} \quad (2)$$

Converting the radial basis function into matrix form gives equation (3). Therefore, the matrices of baseline and target landmark coordinates are used and given in equation (4) and (5). From it the weighting factors and the coefficients of the polynomial function ($p(x)$) can be calculated. The number of landmarks that occur in the baseline and target model is assumed to be n .

$$\begin{pmatrix} A + \alpha * I & B \\ B^T & 0 \end{pmatrix} \begin{pmatrix} \lambda \\ c \end{pmatrix} = \begin{pmatrix} T \\ 0 \end{pmatrix} \quad (3)$$

A n x n Matrix

$$A = \varphi(r_{ij})$$

α smoothing factor, $\alpha = 0$ generates exact interpolation

c constant

$$B = \begin{bmatrix} 1 & x_1 & y_1 & z_1 \\ \vdots & \vdots & \vdots & \vdots \\ 1 & x_n & y_n & z_n \end{bmatrix} \quad (4)$$

B ... n x 4 Matrix, with x, y, z are the coordinates of the baseline Landmarks

$$T = \begin{bmatrix} X_1 & Y_1 & Z_1 \\ \vdots & \vdots & \vdots \\ X_n & Y_n & Z_n \end{bmatrix} \quad (5)$$

T ... n x 4 matrix with X, Y, Z are the coordinates of the target landmarks

After the values for λ and c have been calculated, the matrix form can be rewritten from equation (3) to equation (6). With number of nodes in baseline Model assumed to be N the coordinates of the nodes in the morphed model (T') can be calculated. Therefore, equation (6) needs to be solved. The matrices used in it with the coordinates of the baseline and morphed model are given in equation (7) and (8).

$$\begin{pmatrix} T' \\ 0 \end{pmatrix} = \begin{pmatrix} A' + \alpha * I & B' \\ B'^T & 0 \end{pmatrix} \begin{pmatrix} \lambda \\ c \end{pmatrix} \quad (6)$$

A' ... N x n matrix

$$A = \varphi(r_{ij})$$

i number of nodes in the baseline model

j number of baseline landmarks

$$B' = \begin{bmatrix} 1 & x_1 & y_1 & z_1 \\ \vdots & \vdots & \vdots & \vdots \\ 1 & x_N & y_N & z_N \end{bmatrix} \quad (7)$$

B' ... N x 4 matrix with x, y, z are the coordinates of the baseline nodes

$$T' = \begin{bmatrix} X_1 & Y_1 & Z_1 \\ \vdots & \vdots & \vdots \\ X_N & Y_N & Z_N \end{bmatrix} \quad (8)$$

T' ... N x 3 matrix with X, Y, Z are the coordinates of the nodes in the morphed model

For the calculation of the interpolation a selection of basis functions is still missing. The used Python package PyGeM contains various functions. The functions included there are listed in Table 4. The formulas of the functions are also listed there. In this context the variable x describes the pairwise distances between two nodes. The parameter r (also called radius) represents a variation possibility of the functions. This parameter can be chosen freely and influences the calculated transformation.

Table 4: Implemented basis functions from PyGeM

Function name	Formula
Gaussian spline	$\varphi(x) = e^{\frac{-x^2}{r^2}}$
Multi quadratic biharmonic spline	$\varphi(x) = \sqrt{x^2 + r^2}$
Inverted multi quadratic biharmonic spline	$\varphi(x) = \frac{1}{\sqrt{x^2 + r^2}}$
Thin plate spline	$\varphi(x) = \left(\frac{x}{r}\right)^2$
Beckert wendland c2 basis	$arg = \frac{x}{r}$ if: $(1 - arg) > 0$ $first = (1 - arg)^4$ else: $first = 0$ $second = (4 * arg) + 1$ $\varphi(x) = first * second$
Polyharmonic spline	$arg = \frac{x}{r}$ if $arg < 1$: $\varphi(x) = arg^{k-1} * \log(arg^{arg})$ else: $\varphi(x) = arg^k * \log(arg)$

For this master's thesis, the basis function was selected based on previous experience by Dr. Johan Iraeus (Chalmers University of Technology). This information was gathered through internal communication at the institute. (Schneider, 2022) Accordingly, the basis function and the associated parameter were chosen as in Table 5. For use in the morphing script, this function was added locally in the PyGeM package.

Table 5: Selected basis function

Function name	Formula
func_added	if $x > 0$: $\varphi(x) = x$ else: $\varphi(x) = r$ with $r = 0.1$

To calculate the transformation of the morphing by means of the radial basis function, landmarks are needed as described above. These landmarks are defined points on the baseline geometry and the target geometry – this meant that these points and their coordinates must be known. For parts, for which the transformation is taken over from the model version 0.2.5, the landmarks are defined in this model version. Only the calculated transformation is then applied to the nodes of the new model generation. For parts whose transformation can be calculated directly in version 0.3.0, the landmarks are defined by already morphed nodes of the new model version.

An overview of the procedure is given in Figure 14. The numbering of the occurring labels used in it also matches that in Figure 15.

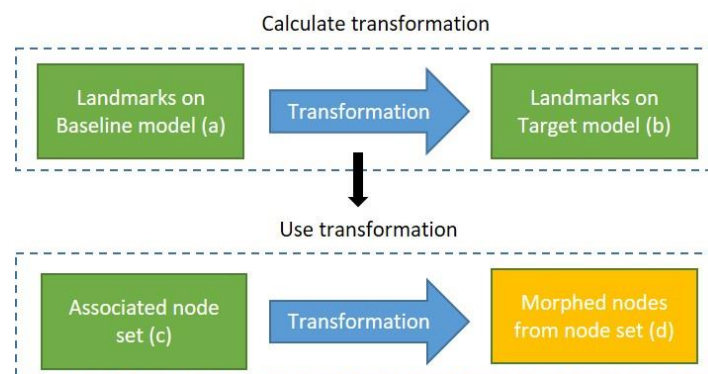


Figure 14: General morphing process

In addition to the schematic representation of the processing of the landmarks above, an example application is given below. In Figure 15 the baseline model is the 50F standing (a) and the target model is the 50F sitting (b). The landmarks are shown as an example on the right arm and as red dots. They must be present in the baseline and target model. The corresponding node set of the baseline model (c) is shown in blue. It should be noted here that in this example neither the number of landmarks nor the size and location of the associated node set corresponds to the combination used in the Python script. These serve only for an exemplary representation to describe the general process visually.

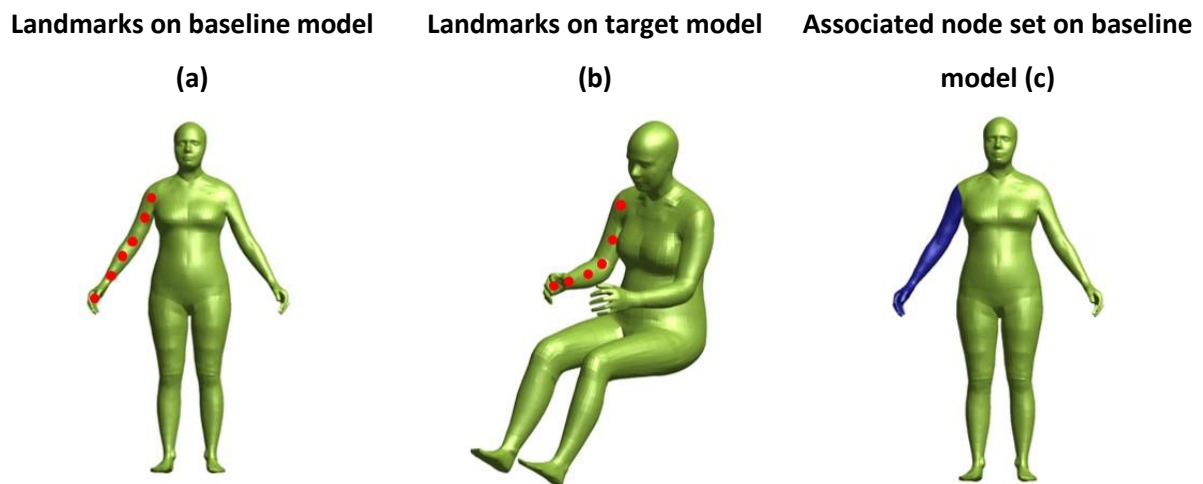


Figure 15: Landmarks with associated node set

Therefore, in this way the transformation is always formed from landmarks and then applied to an associated node set. As a consequence, a suitable selection and combination of landmarks for the respective node set is vital.

As already mentioned, only the coordinates of the nodes are included in the calculation and application of the transformation. This results in a change of the model geometry without changing any other model parameters.

In order to find suitable combinations of node sets and landmarks and to gain first experiences in dealing with model morphing several steps were performed in this work. These will be briefly explained here.

Initially, only a morphing of the femur head was attempted. For this purpose, the femoral head of the VIVA+ model series (in particular that of the 50F) was morphed onto a known femoral head bone. In order to determine which interpolation method was best suited for this purpose, several were investigated. The interpolation methods tested initially were the RBF, FFD and IDW.

When using FFD interpolation, it turned out that no landmark nodes could be used in it. This kind of node manipulation only allowed a very rough distortion of the initial geometry. The nodes in question were enclosed in a control box (red dots in Figure 16), which was then distorted at one or more corner points. The contained nodes were shifted according to the deformation of the control box. Figure 16 (a) shows the original nodes of the femoral head of the baseline model. On the right side (Figure 16 b), the position of the nodal points was distorted by moving one of the corner points of the control box (see Figure 16 b, upper right corner).

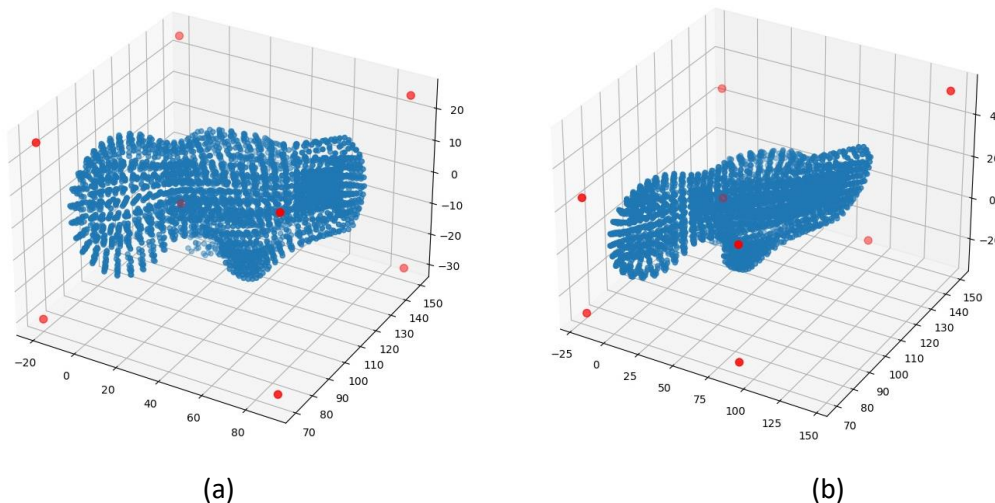


Figure 16: Using the free form deformation on femur head

Due to the fact that no landmarks could be considered by means of FFD and only all nodes within a control box were changed, this interpolation option was excluded for further use.

For the purpose of morphing the baseline femur head onto a known target femur head, landmarks on known CT bone images were assigned to the landmarks of the VIVA+ model. A total of 23 landmarks on the baseline and target femur were used for this procedure. Subsequently, different basis functions were tested and their input parameters were varied. Afterwards, the number of elements that did not meet the quality criteria was documented. The quality criteria used for this purpose have already been explained in chapter 1.4. Based on these values, a first comparison was made for further use. Figure 17 (a) shows the baseline femur head used for this purpose (50F seated) and Figure 17 (b) shows the target femur head used. From this step, experience was gained in dealing with landmark based morphing operations. The results using the two interpolation options (IDW and RBF) were compared.

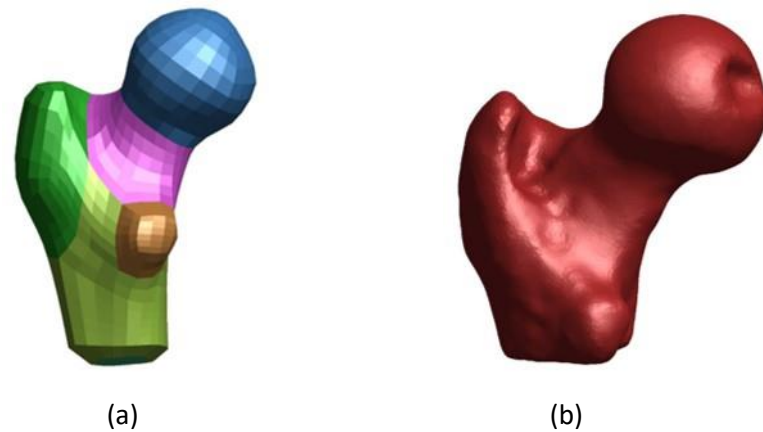


Figure 17: Baseline and CT image femur head

Further, Table 6 shows the values used for the quality criteria described in chapter 1.4. Any element that did not meet the listed values and was therefore beyond the quality criteria was designated as an 'off element'. This was done for shell and solid elements. When using different basis functions and function parameters, the respective number of off elements was then recorded. With these values, a comparison of different basis functions was performed. In chapter 3 Figure 26 and Figure 27 show the results of this step. The evaluation of the morphed element qualities was performed with the software ANSA v21 as described in chapter 1.4. In the VIVA+ model, a distinction is made between two levels of accuracy. The stricter accuracy (Table 6 right side, colored in red) was used for the comparison of the interpolation functions. These sensitive criteria were selected in order to detect subtle differences in the results.

Table 6: Femur mesh quality criteria - VIVA+ (VIVA+, 2022)

Femur solid mesh quality				
Criteria	Limit	% of failed elements	Limit - strict	% of failed elements
Aspect ratio	< 10	0	3	6.84
Skewness	> 60°	0.04	> 45°	3.26
Warping	< 15	0.09	< 10	0.67
Jacobian	< 0.3	0	> 0.7	1.56
Internal angle	> 160°	0.05	> 140°	2.71
	< 20°	0	< 30°	0.14
Femur shell mesh quality				
Criteria	Limit	% of failed elements	Limit - strict	% of failed elements
Aspect ratio	< 10	0	3	1.38
Skewness	> 60°	0	> 30°	10.6
Warping	< 15	0	< 7	1.77
Jacobian	< 0.3	0	> 0.7	0.22
Internal angle	> 160°	0	> 135°	2.76
	< 20°	0	< 45°	2.46

In addition to the number of solid and shell elements that did not meet the quality criteria listed, a visual comparison of the results obtained was performed. The morphing pass with IDW was varied with its input parameter (term power). The resulting course of off-elements is visible in chapter 3 Figure 27 (d). Despite the low number of off-elements in the best point (power=0), other problems occurred. It turned out that the IDW method was not well suited either, as it resulted in numerous unrealistic distortions of the elements. The graphical representation of the morphed femoral head using IDW and power=0 can be seen in Figure 18.



Figure 18: Femur head morphing using IDW and power=0

For the reasons given above, the interpolations using FFD and IDW were therefore excluded. In the following, only the interpolation by means of RBF was considered.

Based on the previous findings, a new Python script was created to morph model version 0.2.5 alone. In it, the entire model was morphed and not just the femoral head. The script was continuously revised and results obtained were evaluated. In it, the model of the 50F seated was morphed to the known 50F cyclist with the left leg down model. The already known model in the cyclist position was previously positioned using pre-simulation (conventional approach using PIPER and positioning simulation). Thereby it was possible to compare the morphed model with the conventionally positioned model. In this way, many suitable combinations of landmarks for calculating the transformation and associated nodes were found. During the creation and execution of this script, many problems with the first version of it were identified. For example, there were excessive memory requirements and very long computation times. These problems were significantly reduced by splitting the morphing calculations into several smaller parts (instead of entire body regions at once) and extensive use of NumPy arrays.

Another insight during these tests was the creation and inclusion of a custom include file. This contained node sets and thus the manual preparatory work for the morphing process was significantly reduced. Before this include file was inserted, a separate node file had to be created for the landmarks and one for the associated baseline nodes. This represented a large effort and was very time-consuming. Especially because the appropriate combinations had to be found first, an alternative approach was needed. This resulted in the additional include file to the VIVA+ main file. In it, landmarks and associated nodes could be specified together. Another advantage of this was that changed baseline and target models (and the associated changed coordinates of the nodes) could also be processed. In the previous approach with node files, the files had to be created manually for each model first.

By looking at the model version 0.2.5 individually, basic combinations of landmarks and node sets could be chosen. These were partially taken over directly when including the model version 0.3.0 in the Python script. For this purpose, case discrimination was performed in each case. In this distinction between the takeover of the computed transformation from v. 0.2.5 (see chapter 2.3) and the computation of the transformation directly in v. 0.3.0 (see chapter 2.4) was differentiated.

The basis of the combinations of landmarks and associated nodes were the previous findings in some cases, however, adjustments had to be made. These adjustments were mainly necessary in regions where new parts were added in the new model generation.

When considering the new model generation in the Python script, a different behavior with respect to the chosen basis function also emerged. As a result, the progressions of the off elements from the morphing experiments of the femur head could no longer be applied to the entire model. The pure consideration of shell and solid elements, which do not fulfill the quality criteria, was no longer sufficient. Intrusions or unrealistic nodal distortion also had to be taken into account. The occurrence and number of solid elements with negative volumes also had to be considered. As a result, the combination of landmarks and associated node sets iteratively changed significantly. The basis function used was also changed as a result. Due to the longer computing times per run, a re-evaluation of all available basis functions, as previously performed for the femoral head, was not considered again.

After the previous versions always used the seated 50F as baseline and the cyclist position of the 50F with left leg down as target, the script was also applied to other baseline and target poses. This also resulted in different combinations of landmark nodes and the corresponding node sets, depending on the models used. Accordingly, certain combinations were changed or added again in this context.

In order to perform further comparisons between morphed models and baseline models, defined criteria are needed. These are determined by the number of solid elements with negative volumes, occurring intrusions and by quality criteria of the FE mesh. The defined criteria are listed in Table 7. For the quality criteria aspect ratio, skewness, warping and Jacobian deviation, the same limit values now apply. In the quality criteria used from here on, there are also different limit values regarding the maximum and minimum internal element angles. In addition, a distinction is also made between the individual subcategories of solid and shell elements. Furthermore, the masses of the models and the number of internal penetrations were used for comparison. In chapter 3 several diagrams are presented, which show the comparison between the morphed models and their corresponding baseline and target models. It should be noted, however, that no direct comparison between models from v. 0.2.5 and v. 0.3.0 was feasible. Especially due to changed contact conditions and a changed number of elements and parts, no absolute statements could be made. This is especially true for the representations in chapter 3.2. In Figure 44 to Figure 47 (f in each case), the number of internal penetrations is shown respectively. There are clearly fewer internal penetrations in the v. 0.2.5 target model than in the models of v. 0.3.0. For the reasons given above, however, this will not be dealt with in the discussion later.

Table 7: Mesh quality criteria for comparison

Solid mesh quality criteria		Shell mesh quality criteria	
Criteria	Limit	Criteria	Limit
Aspect ratio	< 12	Aspect ratio	< 12
Skewness	> 70°	Skewness	> 70°
Warping	< 30	Warping	< 30
Jacobian	< 0.3	Jacobian	< 0.3
Min. angle Tetras	< 15°	Min. angle Quads	< 15°
Max. angle Tetras	> 160°	Max. angle Quads	> 170°
Min. angle Pentas	< 15°	Min. angle Trias	< 15°
Max. angle Pentas	> 160°	Max. angle Trias	> 160°
Min. angle Hexas	< 15°		
Max. angle Hexas	> 170°		

In the further course, the morphed models were compared to the respective baseline models. For this purpose, the baseline models were also checked for intrusions and solid elements with negative volume. However, no intrusions or solid elements with negative volume were thereby found.

In the following, a graphical representation is given to describe the comparisons made. These can be found in chapter 3. In chapter 3.1 comparisons between morphed models to their respective baseline model are shown. For this, starting from one baseline model, this was morphed to several target models. For example, for the comparison visible in Figure 29, the following models were considered. Starting from the 50F standing baseline model (Figure 19 a), the 50M standing rotated (Figure 19 b), the 50M standing (Figure 19 c), the 50F cyclist with left leg down (Figure 19 d) and the 50F pedestrian (Figure 19 e) were morphed. These were subsequently compared to their baseline model.

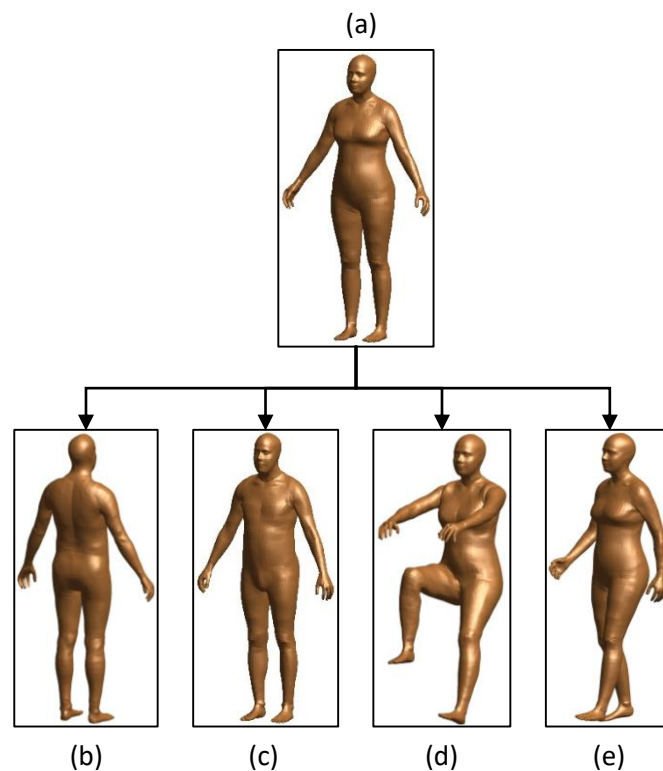


Figure 19: Model comparison approach in chapter 3.1

Another comparative approach was selected for chapter 3.2. Here, morphed models were compared, which were supposed to represent the same target model, but originated from different baseline models. For the comparison, which is presented in Figure 44, a graphical representation follows here as well. Figure 20 shows the models used for this purpose. All models were morphed to the target position of the 50F cyclist with left leg down. The baseline models used were the 50F standing (a), the 50F seated (b) and the 50F seated, which was first morphed to the 50F standing via an intermediate step (c).

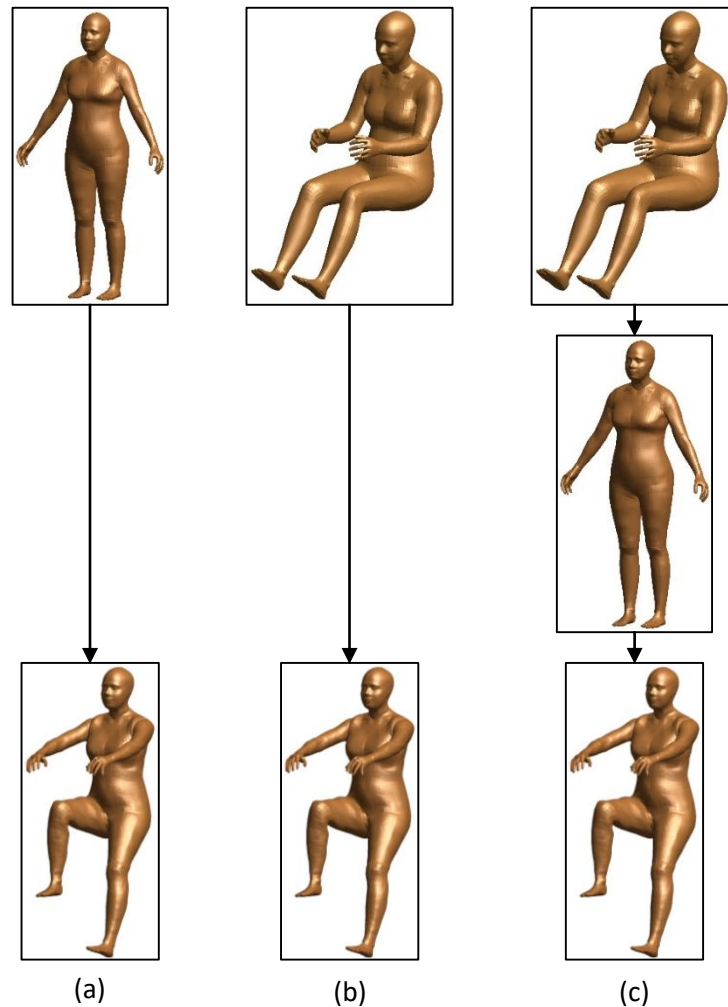


Figure 20: Model comparison approach in chapter 3.2

2.3 Applying transformation from version 0.2.5

In Figure 21 the schematic procedure for the calculation and use of the transformation for certain body parts is given (see Table 8). Several reasons can be relevant to adopt the transformation from v. 0.2.5:

- If the body part is a bone or skin, the transformation should be taken from the old model generation. The reason for this is that the new model is to be built using the landmarks of bone and skin.
- If there are no nodes which are already morphed in the surrounding of the body part, the transformation must also be adopted from the old generation.
- If a better quality is created by taking over the transformation from v. 0.2.5, it is used.

For the body parts which are listed in Table 8, a direct calculation of the transformation in the new model version is not possible. Here first the transformation is calculated from the changed position between the models of the version 0.2.5. The basis for this are the nodes with the corresponding coordinates in the baseline model (Figure 21 a) and in the target model (Figure 21 b). After the calculation of the transformation from model version 0.2.5, this is applied to the associated nodes of the baseline model of model generation 0.3.0. (Figure 21 c).

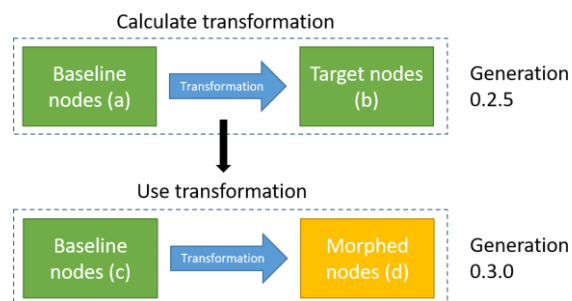


Figure 21: Scheme - Transformation from 0.2.5

The colour scheme in Figure 21 is intended to provide information about known and yet unknown models. The models shown in green (i.e. their nodal coordinates) are assumed to be known. These are the baseline and target models of the old model series and the baseline model of the new generation. The transformation, which is represented by the blue arrow, is calculated from the old model generation and applied to the new one. The final results are the morphed nodes (Figure 21 d), which subsequently create the new model series model in the desired target configuration.

Figure 22 shows an exemplary view of the bones of the pelvis and the lower extremities of the baseline (a) and target (b) configuration from version 0.2.5 and the baseline model from version 0.3.0 (c). Here, the baseline is the 50F seated and the target is the 50F cyclist with the left leg down. In each case, the

left femur is shown in red. The transformation is calculated from the change in the position of the femur between the models of the old model series. This is then subsequently applied to the femur bone of the baseline model of the new generation.

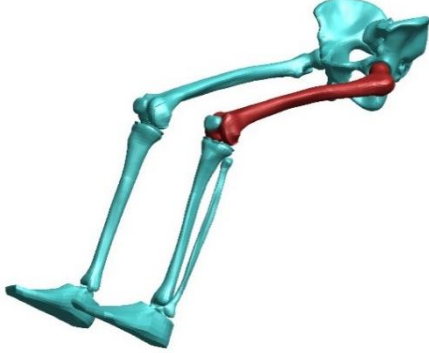


Version	Baseline	Positioned
0.2.5	 <p>(a)</p>	 <p>(b)</p>
0.3.0	 <p>(c)</p>	<p>?</p>

Figure 22: Exemplary representation le. femur

While Figure 22 showed both legs, Figure 23 only shows the left femur of the above models. A change in the angle of the target bone (b) compared to the baseline bones of models 0.2.5 (a) and 0.3.0 (c) can be seen. The elements shown here (the FE grid can be roughly seen) are created by the point coordinates of the assigned nodes. For a better representation, the elements are shown here and not only the point cloud underlying them. Strictly speaking, only the vertices (nodes) of the elements are used for the calculation of the transformation. Information about points related to an element is not considered. Consequently, when morphing skin and bone, the landmark nodes are given by the surface nodes of these parts. In this case, for example, a three-dimensional rotation was applied to the femur.


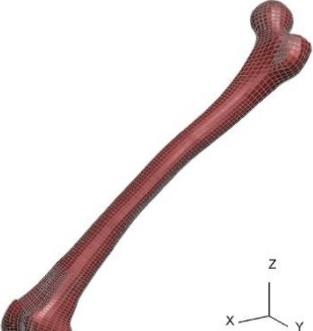

Version	Baseline	Positioned
0.2.5	 <p>(a)</p>	 <p>(b)</p>
0.3.0	 <p>(c)</p>	<p>?</p>

Figure 23: Exemplary representation le. femur - detailed

An overview is given in Table 8, which divides the body parts into subparts. The parts listed therein are morphed by the procedure described in this chapter.

Table 8: Parts that apply a transformation from v. 0.2.5

Body region	Parts included
Upper body skin	Head and neck skin, Torso skin
Head and neck	Head bones, Neck bones
Right leg	Femur, Leg skin, Fibula head, Tibia head, Patella, LX-Soft-knee
Left leg	Femur, Leg skin, Fibula head, Tibia head, Patella, LX-Soft-knee
Right arm	Arm skin, Clavicle and Scapula, Humerus, Ulna and Radius
Left arm	Arm skin, Clavicle and Scapula, Humerus, Ulna and Radius
Thorax	Thorax vertebra bones, Rib bones, Sternum bone
Abdomen	Abdomen vertebra bones
Pelvis	Pelvic bones, Hip ligament left and right

In addition to the body parts listed in the table above, more specific details on their structure are shown in Table 9 and Table Appendix A.1-1 to Table Appendix A.1-8. These tables provide information about the application of the transformation calculated in version 0.2.5 to the individual parts of different body regions. They contain information about which nodes are used for the calculation of the transformation (v. 0.2.5) and to which nodes it is then applied (v. 0.3.0). The number of nodes used as landmarks and the number of nodes to which the transformation was applied are also visible. In the created Python script, the respective nodes are identified by the specified node sets.

Table 9: Apply a calculated transformation from v. 0.2.5 to v. 0.3.0 in upper body skin

Region	Landmarks for transformation in v. 0.2.5	# of landmark nodes	Baseline in v. 0.3.0	# of baseline nodes
Head and neck skin	All nodes from head and neck skin	5019	All nodes from head and neck	5019
Torso skin completed	All nodes from Torso skin	4163	All nodes from Torso skin	10104

An example of the contents of these tables, which adopt the transformation from v. 0.2.5, is shown in Table 9. The first row describes the considered nodes in the morphing process of the skin of head and neck. The first column (Landmarks for transformation in v. 0.2.5) lists which nodes are used for the computation of the transformation. In column two (# of landmark nodes) the number of landmark nodes described in the first column is given. Column three (Baseline in v. 0.3.0) describes to which nodes of the current model generation the just calculated transformation is applied, i.e. which nodes are to be morphed. Column four (# of baseline nodes) contains the number of nodes to be morphed. This explanation can also be applied to the other tables, which can be found in the appendix.

2.4 Calculating the transformation directly in version 0.3.0

In contrast to adopting the transformation from the previous model generation, as described in chapter 2.3, the transformation can also be calculated directly in the new model generation. The schematic sequence of this procedure is shown in Figure 24. In order to be able to carry this out, however, already morphed nodes must exist. These already morphed nodes have to be created by previous steps where the transformation of v. 0.2.5 was taken over. Starting from these previously morphed nodes, the change in coordinates between the baseline model (Figure 24 a) and the previously morphed nodes (Figure 24 b) is used to calculate the transformation. This transformation can then subsequently be applied to body parts of the corresponding region in the remaining baseline model (Figure 24 c). The output is the remaining morphed body parts of the corresponding region (Figure 24 d). It should be noted that all models used are already in version 0.3.0. Once again, the color scheme is intended to provide information about known and unknown models. Fields in green represent known models or parts of it. In this case, these are the baseline model and the previously morphed nodes. The transformation, in blue, is calculated from this. The searched model, in this case the remaining nodes, are shown in yellow.

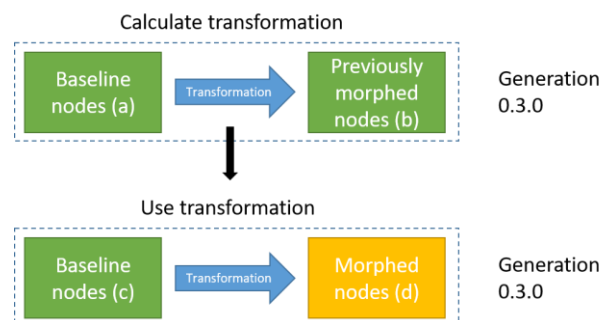


Figure 24: Scheme - Transformation from 0.3.0

For example, with already morphed nodes of the bones and the associated skin of a body part, the tissue that lies between these parts can be morphed.

When morphing directly in version 0.3.0, the landmarks are defined by previously morphed nodes. In the Python script, the respective nodes are identified by the specified node sets. Subsequently, it is checked whether the currently used node set already contains morphed nodes. If there are corresponding nodes, the transformation is calculated on the basis of these. The nodes that have already been morphed are also removed from the sets and are not subsequently modified. Thus, they are only used for the computation of the transformation for the remaining nodes from the set.

Figure 25 shows an example of the nodes required for the procedure on the left thigh. For this purpose, the nodes of bone and skin of the lower extremities and pelvis have already been morphed beforehand. The procedure from chapter 2.3 was used for this. In order to be able to morph the

remaining nodes of the soft tissue, the corresponding node set is first searched for nodes that have already been morphed. The nodes found were used to calculate the transformation between baseline and current state. Subsequently, this transformation was applied to the remaining nodes of the set.

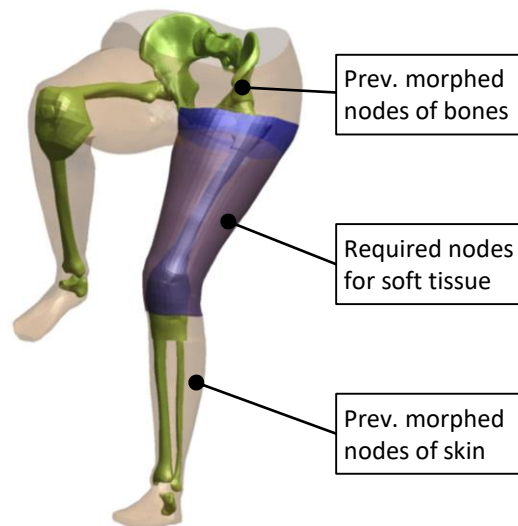


Figure 25: Previously morphed nodes on the left thigh

Body parts and their associated parts which are morphed in this way are listed in Table 10.

Table 10: Parts that calculate a transformation directly in v. 0.3.0

Body region	Parts included
Head and neck	Remaining head, Remaining neck
Right leg	Foot with ankle, Fibula, Tibia, LX-Ankle soft, Lower leg, Upper leg
Left leg	Foot with ankle, Fibula, Tibia, LX-Ankle soft, Lower leg, Upper leg
Right arm	Arm skin – torso connection, Hand, Remaining arm
Left arm	Arm skin – torso connection, Hand, Remaining arm
Thorax	Ribcage external left and right, Intercostal muscles left and right
Pelvis	Pelvic cavity, pelvis connect left and right, pelvic soft tissue internals left and right, pelvic soft tissue left and right
Remaining torso	Thorax soft tissue left and right, Abdominal cavity left and right

Additionally to the overview given above, more detailed information about these body regions is given in Table 11 and Table Appendix A.1-9 to Table Appendix A.1-15. In addition, the association of the parts to the different body regions is also visible. Further, information about the number and location of the landmark nodes as well as the number of the remaining baseline nodes is also listed.

Table 11: Transformation for v. 0.3.0 from prev. morphed nodes in head and neck

Region	Landmarks for transformation in v 0.3.0	# of landmark nodes from prev. morphed	Baseline in v. 0.3.0	# of baseline nodes
Remaining head	Prev. morphed nodes of head skin and bones	7197	All nodes of remaining head	18721 (11524 remaining)
Remaining neck	Prev. morphed nodes of head, neck and bones	2398	All nodes of remaining neck	7621 (5223 remaining)

An explanation of the contents of these tables, which calculate and adopt the transformation directly in v. 0.3.0, will be given as an example using Table 11. The first row describes the nodes involved, which are relevant for the morphing of the remaining nodes of the head (everything except head skin and bones – these were previously morphed using transformation from v. 0.2.5). Column one (Landmarks for transformation in v. 0.3.0) describes which nodes are used to calculate the transformation. Column two (# of landmark nodes from prev. morphed) specifies the number of landmark nodes described in column one. Column three (Baseline in v. 0.3.0) describes to which nodes of the current model generation the transformation just calculated is applied, i.e. which nodes are to be morphed. Column four (# of baseline nodes) contains the number of nodes to be morphed. The explanation of the contents of this table can also be applied to the other tables, which can be found in the appendix.

3 RESULTS

Figure 26 shows the first four courses of tested basis functions. These are from the femoral head morphing experiment described in chapter 2.2. Shown are the numbers of solid and shell elements that did not meet the quality criteria. Shell elements are coloured in blue and solid elements in orange. The number of off elements in the base model (VIVA+ 50F) is shown in dashed lines. The curve was obtained by varying the input parameter (called 'radius' in the following, or short 'r'). The parameter was varied in the interval $r=-100$ to $r=100$ in step size of $r=5$. This range with associated step size was chosen to describe the wide function course. The final use of the value $r=0.1$ was built in only in the later course of the work.

In Figure 26 (a) the result curve when using the added basis function in PyGeM is visible. It can be seen that over a wide range the shell off elements are insignificantly higher than those of the baseline model. From a value of approx. $r=5$, however, the curves begin to differ significantly. Only at values of the radius greater than $r=70$ do the curves come closer again.

The Gaussian spline function (Figure 26 b) showed a symmetrical course of the off-elements in this test. As can be seen, there is a small area where the curves come close to the baseline level. At $r=0$, there is a spike in off elements. As the value of the radius increases or decreases, the number of off-elements increases.

Figure 26 (c) shows the progression when using the thin plate spline. It can be seen that the number of off elements is constant over a wide range and that their level changes at a value around $r=5$. From this transition on, their number also remains constant again.

Next, the Beckert Wendland C2 base function (Figure 26 d). In the area of negative values of the radius, a transition from constant number of off elements, to non-constant and increased number of them is visible. In the positive range of the radius a slow increase of their number is visible.

Results

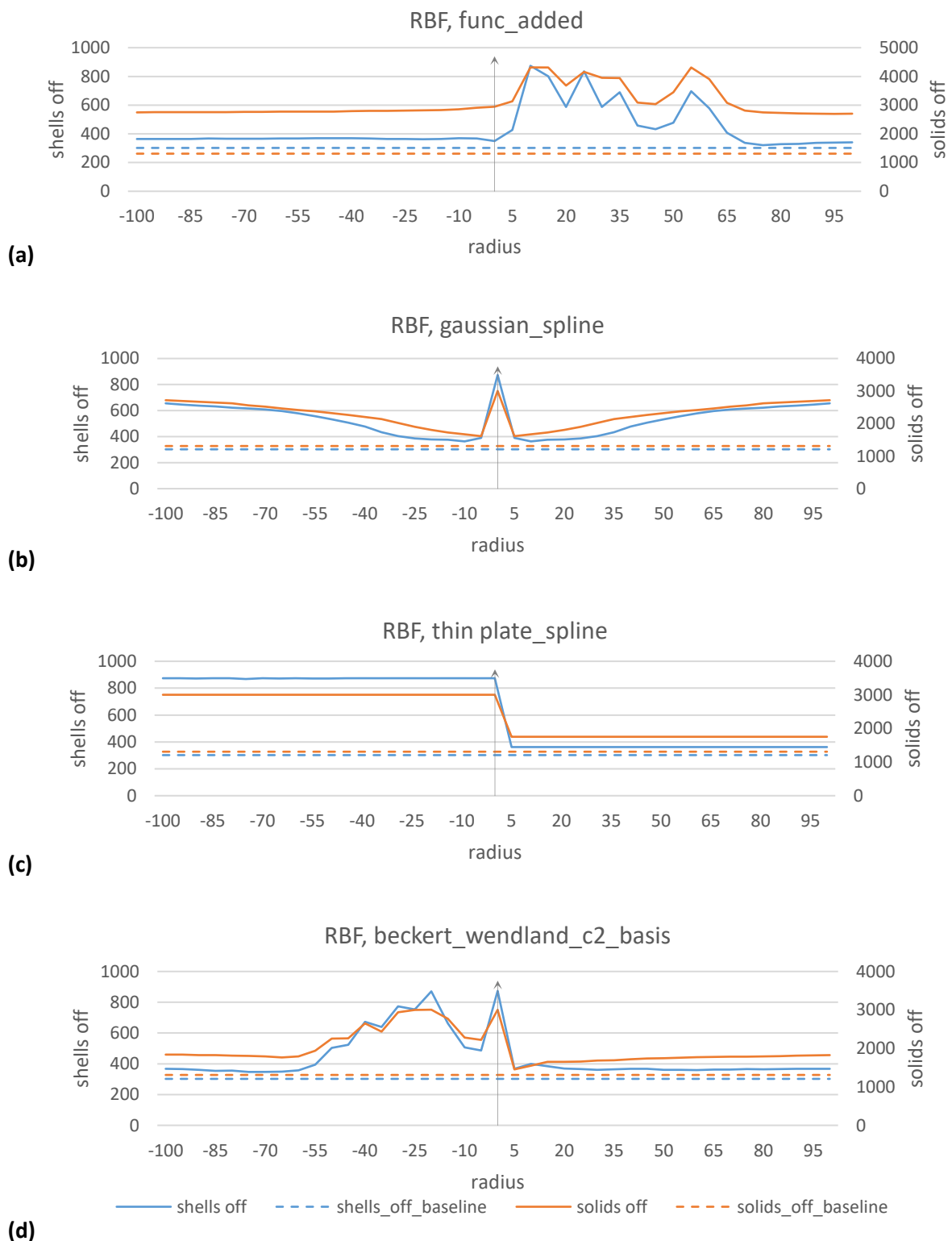


Figure 26: Results from first approach on femur head 1/2

Figure 27 shows further curves with differently selected basis function and variation of the input parameter.

For the curve with inverted multi quadratic biharmonic spline (Figure 27 a) a variation of the parameter 'r' different from the previous one was performed. With this function, an missi appeared in the morphing algorithm when using $r=0$. With this value of the radius, division by zero occurred during the calculation. To avoid this cause of error, an interval from $r=-100$ to $r=104$ with step size of $r=6$ was chosen. The curve shows a symmetrical appearance around the zero point. The level of the solid elements that do not meet the quality criteria is consistently above that of the shell elements.

The course of the multi quadratic biharmonic spline (Figure 27 b) also shows a symmetrical course around the zero point. Over a wide range, the curves of the solid and shell off elements have a similar shape, but differ in their values.

When using the polyharmonic spline (Figure 27 c), a step-like progression was detected. The step occurs between the values $r=0$ and $r=5$. Outside of this transition, a constant course of the off elements is visible.

Figure 27 d shows the progression when IDW interpolation is used. The parameter used is called 'power'. This was varied from -20 to +20 in steps of 1. The level of the off-elements is consistently high except for a low point, which is at $\text{power}=0$.

Results

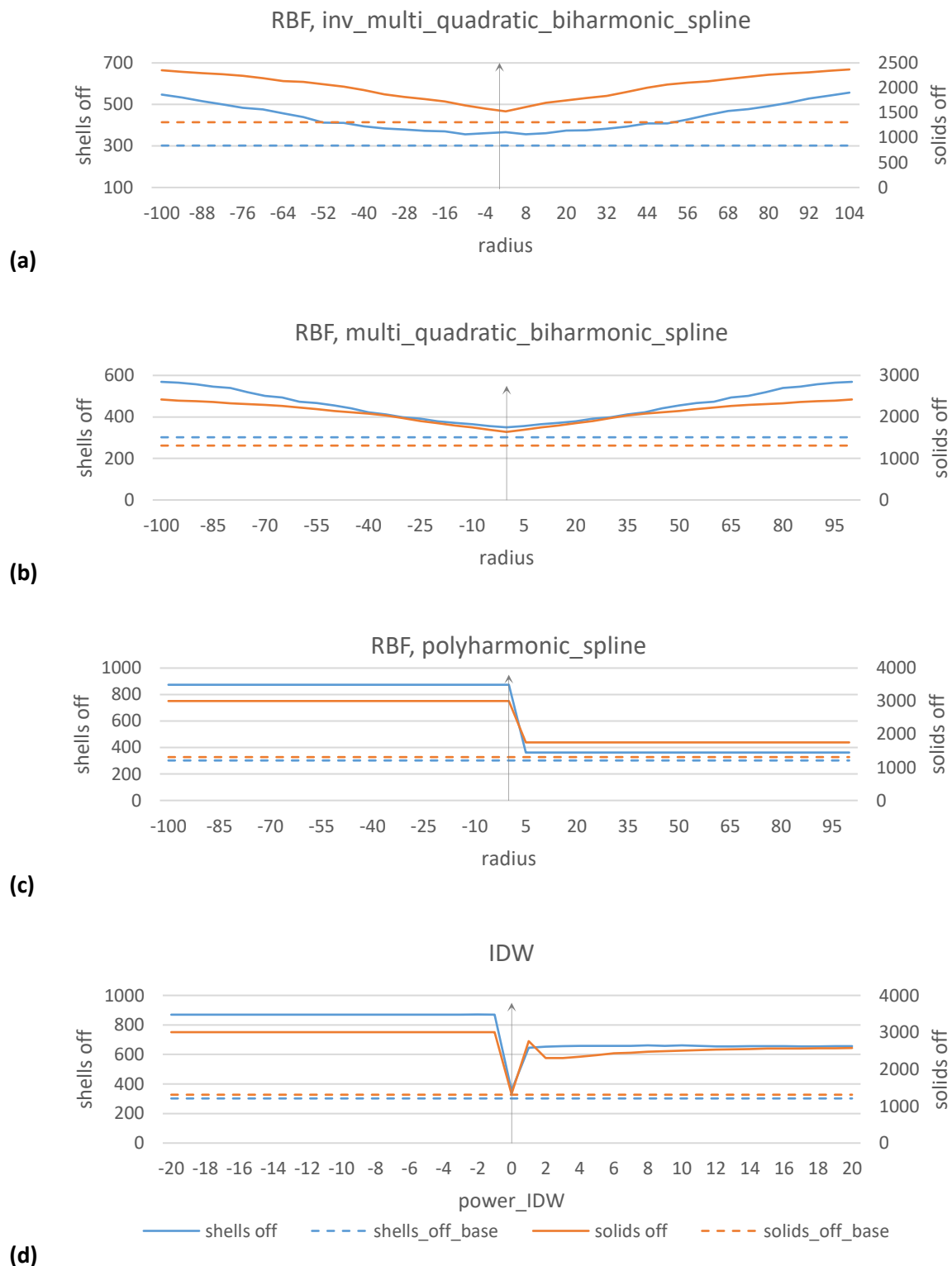


Figure 27: Results from first approach on femur head 2/2

3.1 Comparison to initial model

In this section, results of morphing runs of the whole model are presented. In each case, the baseline models of v. 0.3.0 were morphed to the selected target model of v. 0.2.5. The baseline model was kept constant and target positions were varied. Afterwards a comparison of the morphed model to the baseline model was performed. A further explanation was given in chapter 2.2 (see also Figure 19).

Exemplary results of morphed models are given on the following pages. In Figure 29 the 50F standing position and in Figure 32 the 50F seated position was chosen as baseline model. Similarly, Figure 36 displays results when using the 50M standing position as baseline model. In Figure 40 the 50M seated position was used as the baseline model for morphing. Figure 28 shows the just mentioned baseline models of v. 0.3.0. The standing positions of the average female (a) and the average male (c) as well as the seated position of the 50F (b) and 50M (d) is shown therein. Based on these different baseline models, a selection of models were generated with landmark based interpolation using the radial basis function as it was described in chapter 2.

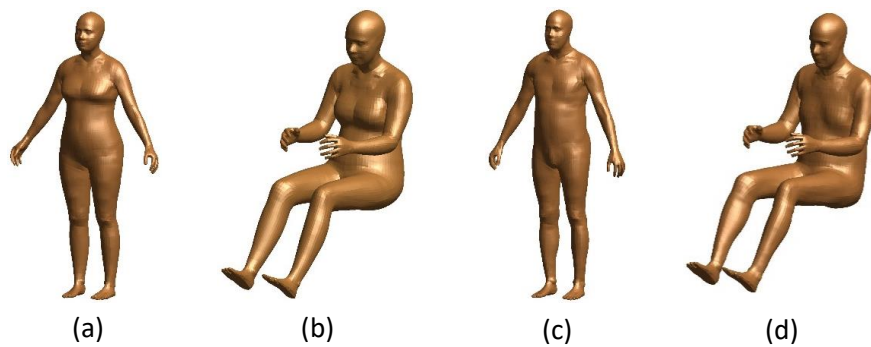


Figure 28: Baseline models of v. 0.3.0

Comparison criteria between baseline and morphed model were the number of solid elements with negative volumes, the number of solid and shell elements not fulfilling the quality criteria presented in chapter 2.2 (Table 7), the masses of the respective models and intrusions that occurred. The determination of the masses was performed in the FE preprocessor Visual Crash DYNA 16.5.2 (<https://www.esi-group.com>). In all diagrams, the results of the morphed models were plotted relative to the values of the used baseline model. The detailed morphing results can be found in the appendix in Table Appendix A.2-1 to Table Appendix A.2-6. Furthermore, this chapter also graphically depicts the intrusions that occurred during morphing.

The model positions selected for this purpose were chosen to cover a wide range of different postures. Moreover, target model positions were also selected according to which ones were already used and required in v. 0.2.5. In addition, the baseline models were morphed to the target positions once from a sitting and once from a standing baseline position. This was to allow a comparison of the morphed model in terms of quality based on different baseline configurations. These comparisons are presented in chapter 3.2.

Results

Figure 29 shows results using the 50F standing as the baseline. This was morphed to the 50M standing with viewing direction in negative x-axis (180° rotated relative to the baseline) and viewing direction in positive x-axis. In addition, the model was morphed to the 50F cyclist position with left leg down and the 50F pedestrian position according to TB024. The position of the target pedestrian position in v. 0.2.5 was performed according to Euro NCAP (see Euro NCAP, 2021).

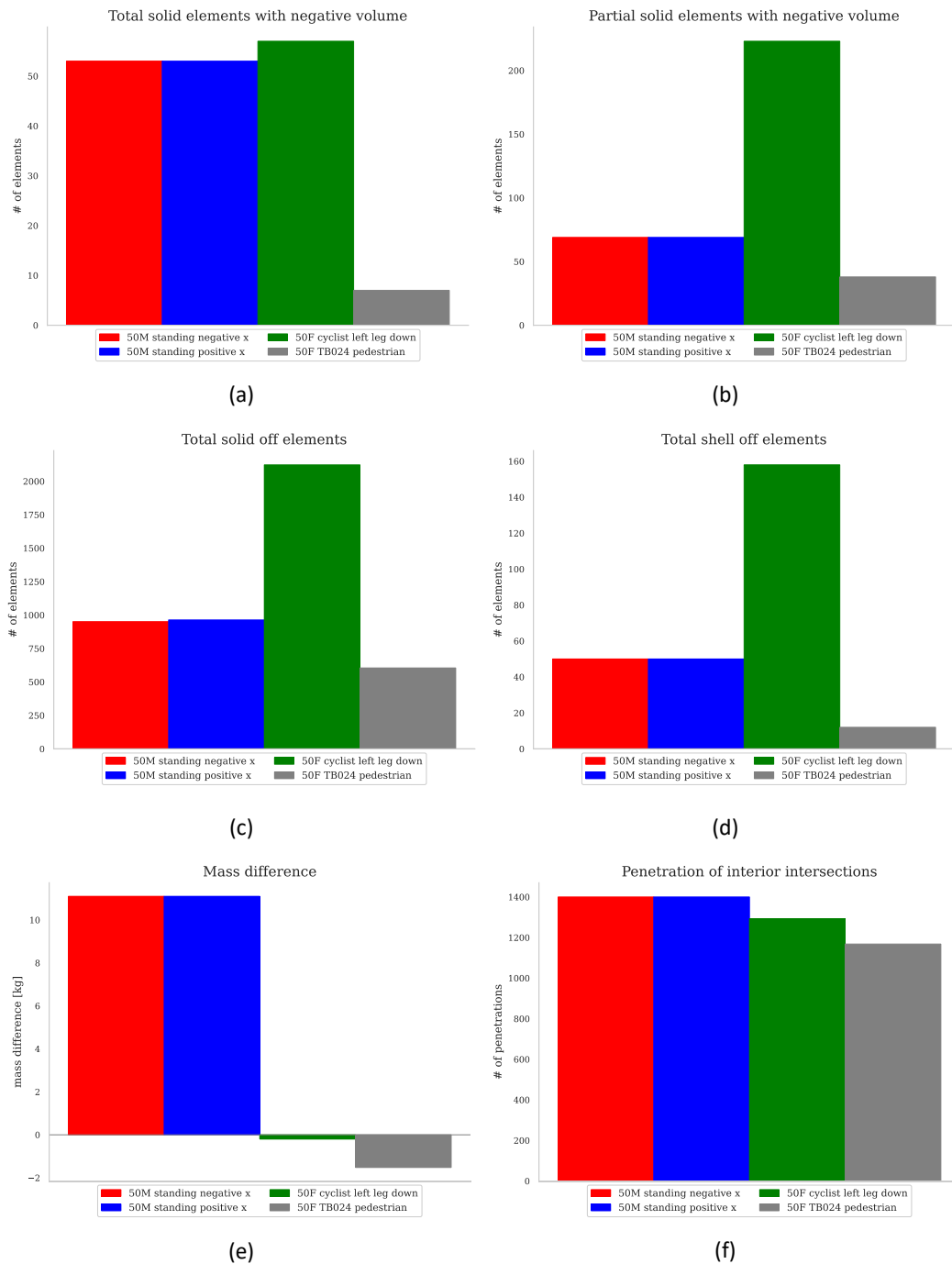


Figure 29: Morphing the 50F standing baseline model

During the morphing process from 50F standing to 50M standing, intrusions occurred in the area of the knee. These are visible in Figure 30 (a). This is a posterior view of the legs. In it, the intrusions of the femur through the knee LX soft tissue are visible. Changing the orientation of the target model did not have a major impact on the results. Morphing the 50F standing to the 50F pedestrian position created intrusions on the anterior aspect of the knee. These were caused by penetration of the knee LX soft tissue through the tibial bone. This is shown in Figure 30 (b).

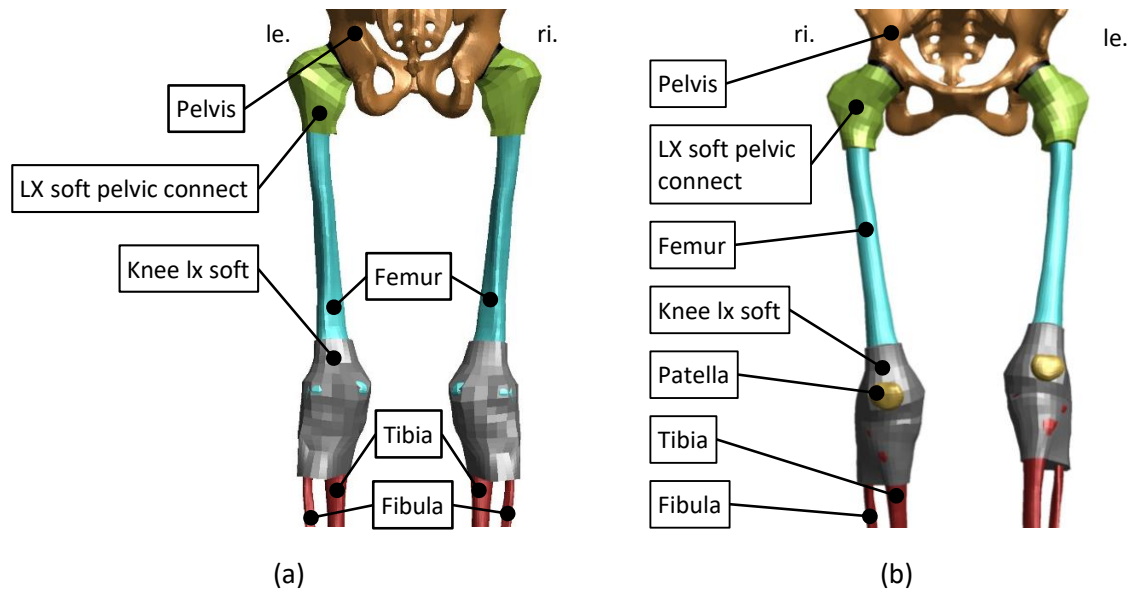


Figure 30: Morphed 50F standing to 50M standing and 50F TB024 pedestrian

Intrusions occurred at the 50F cyclist position generated in the process starting from the 50F standing. These occurred at the knee LX soft tissue anteriorly through femur and tibia (Figure 31 a), at the caudal pelvis through penetration of pelvis bone through tissue (Figure 31 b) and at the proximal humerus posterior (Figure 31 c).

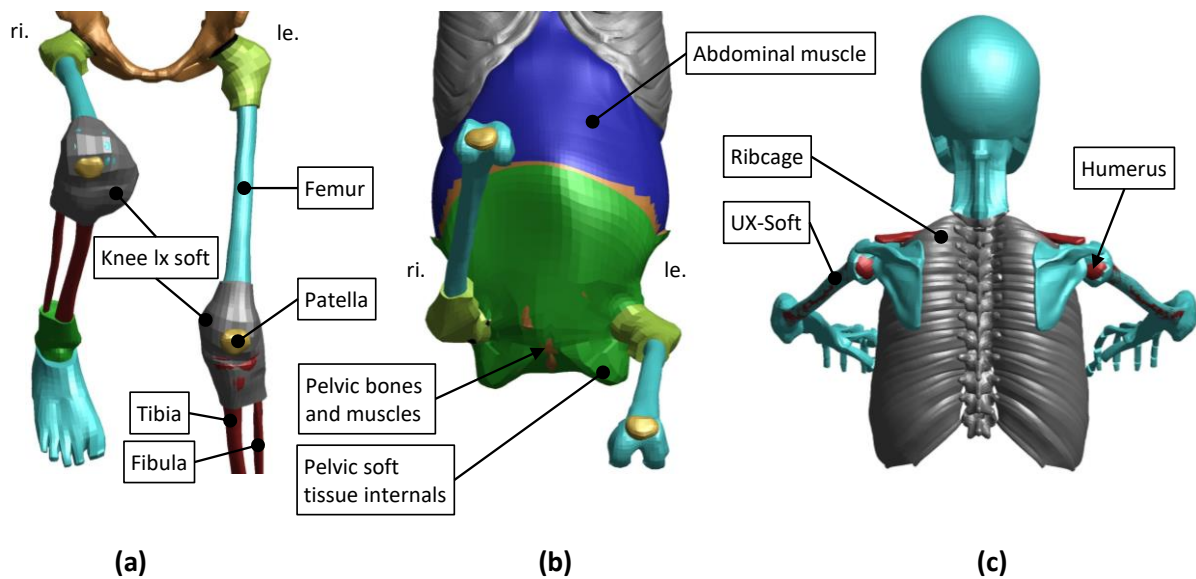


Figure 31: Morphed 50F standing to 50F cyclist left leg down

Results

Figure 32 shows results using the 50F seated as the baseline model. This was morphed to the 50M seated, 50F cyclist with left leg down, 50F TB024 pedestrian and the 50F standing.

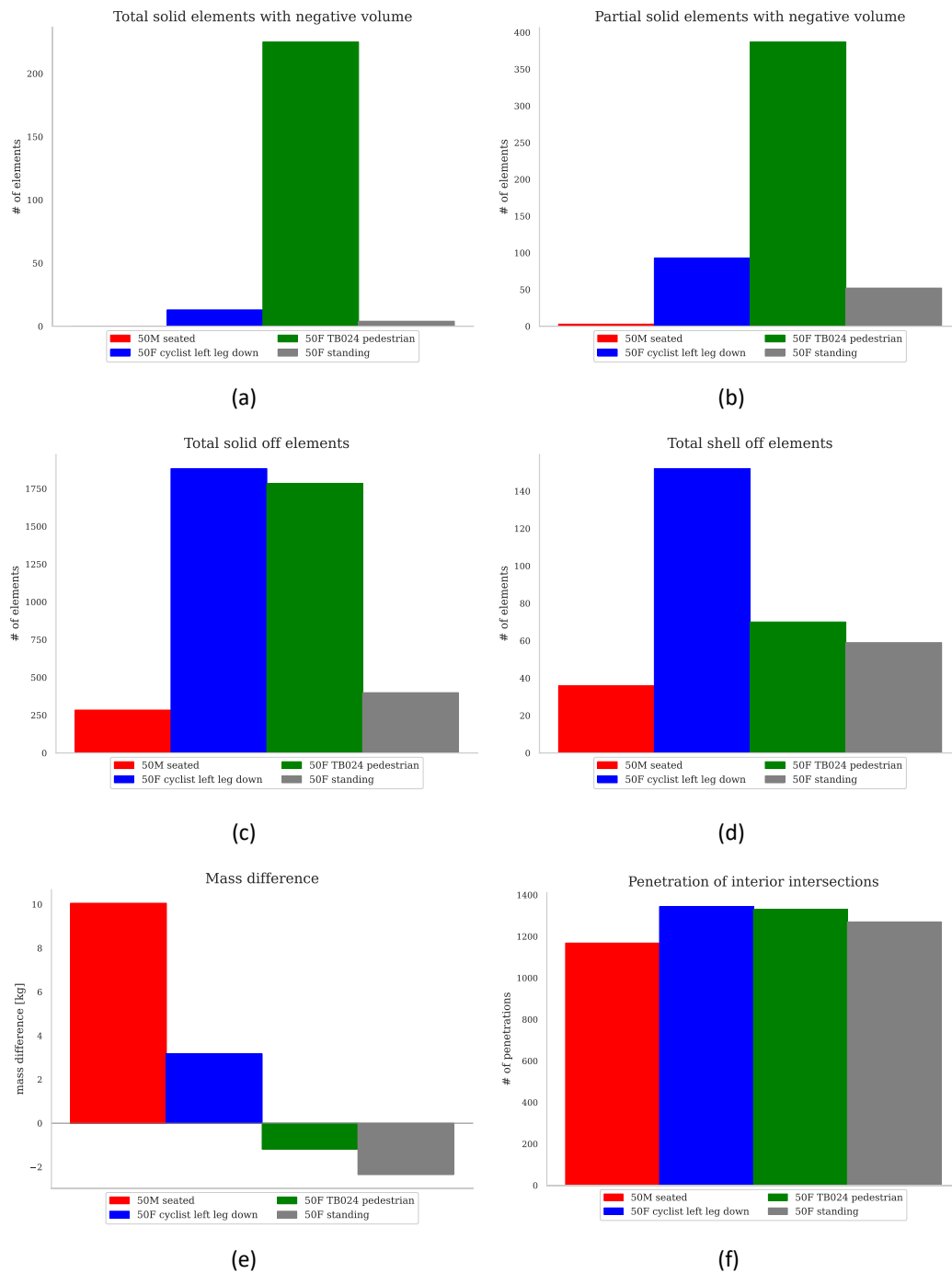


Figure 32: Morphing the 50F seated baseline model

The morphed cyclist model of the 50F with left leg down starting from the 50F seated contained intrusions. These occurred at the knee anteriorly between knee LX soft, femur and tibia (Figure 33 a), at the caudal pelvis between tissue and pelvis bone (Figure 33 b) and at the proximal humerus posterior (Figure 33 c).

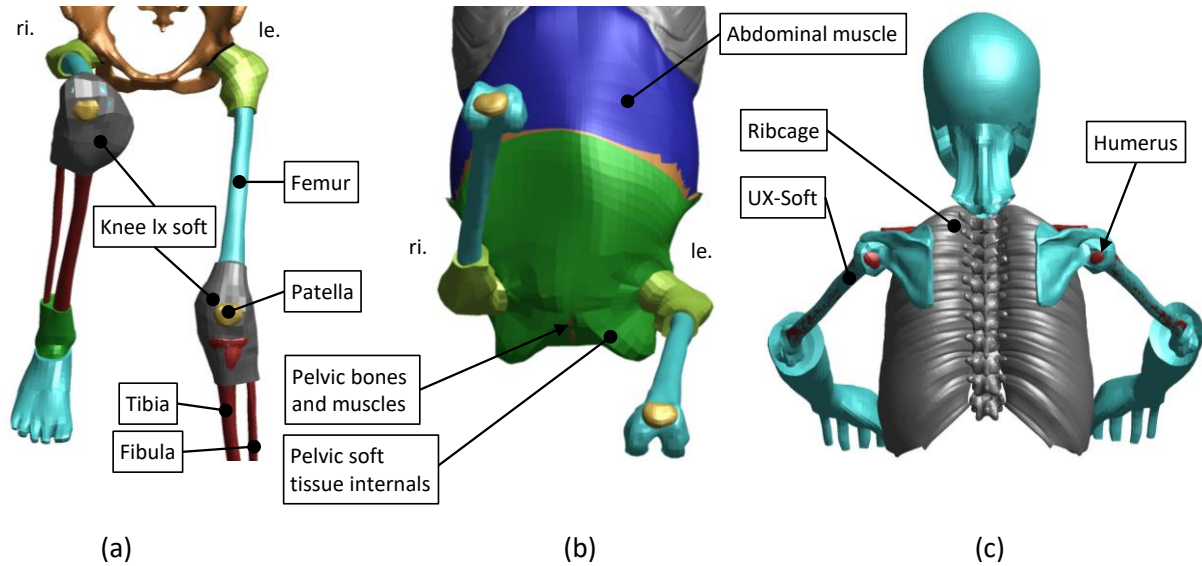


Figure 33: Morphed 50F seated to 50F cyclist left leg down

Intrusions at the morphed 50F in pedestrian position starting from the 50F seated position are shown in Figure 34. Skin penetration occurred on the left lower leg anteriorly (Figure 34 a) and on the left forearm posteriorly (Figure 34 b). At the knee LX soft anteriorly, intrusions with the tibia bone occurred on both sides (Figure 34 c). At the anterior junction of the pelvis to the femur bone, there was intrusion between the LX soft pelvic connective tissue and the hip ligament on both sides (Figure 34 d).

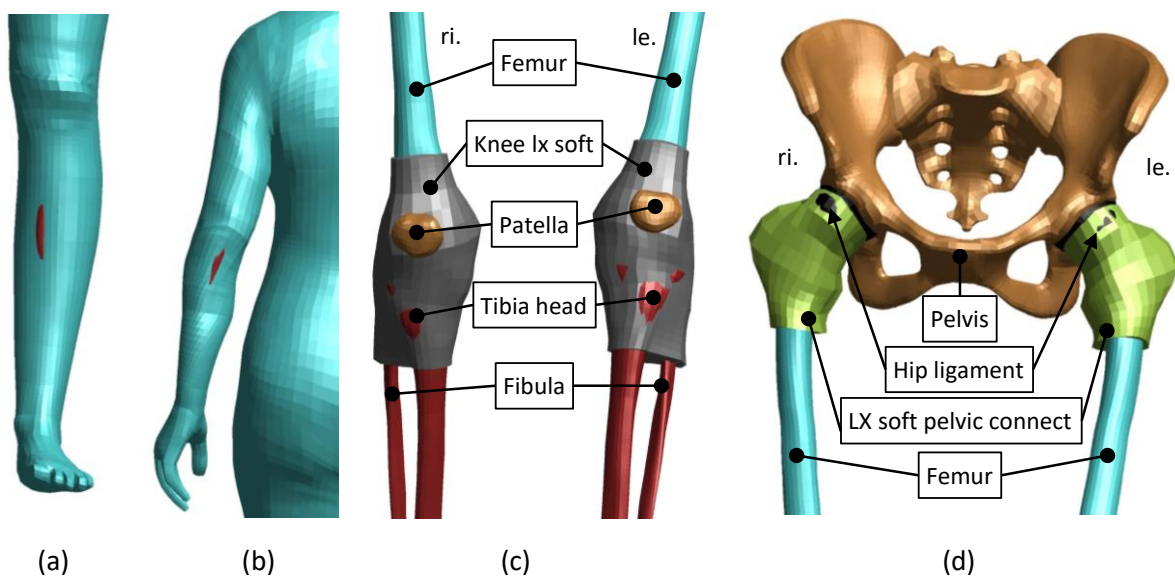


Figure 34: Morphed 50F seated to 50F TB024 pedestrian

Results

Morphing of the 50F seated to the 50F standing resulted in intrusions at the anterior side of both ends of the humerus. Additionally, intrusions occurred anterior between the pelvis and femur. There, overlap between the hip ligament and the LX soft pelvic connection tissue emerged. These are illustrated in Figure 35.

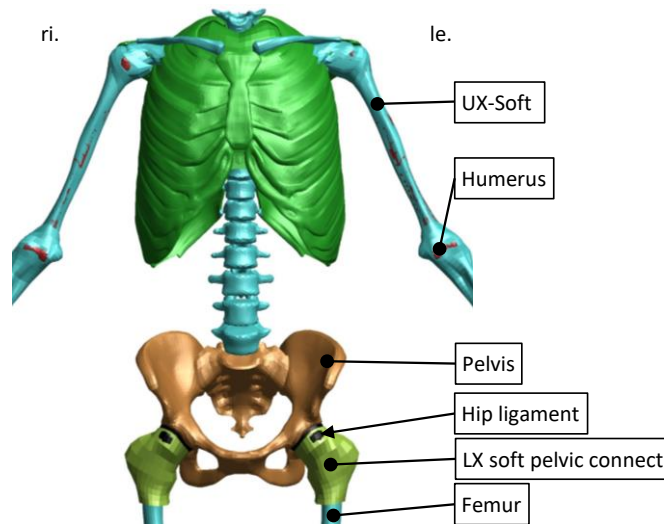


Figure 35: Morphed 50F seated to 50F standing

Results using the 50M standing baseline model for morphing to 50F standing, the 50M pedestrian and the 50M cyclist with left leg down are shown in Figure 36.

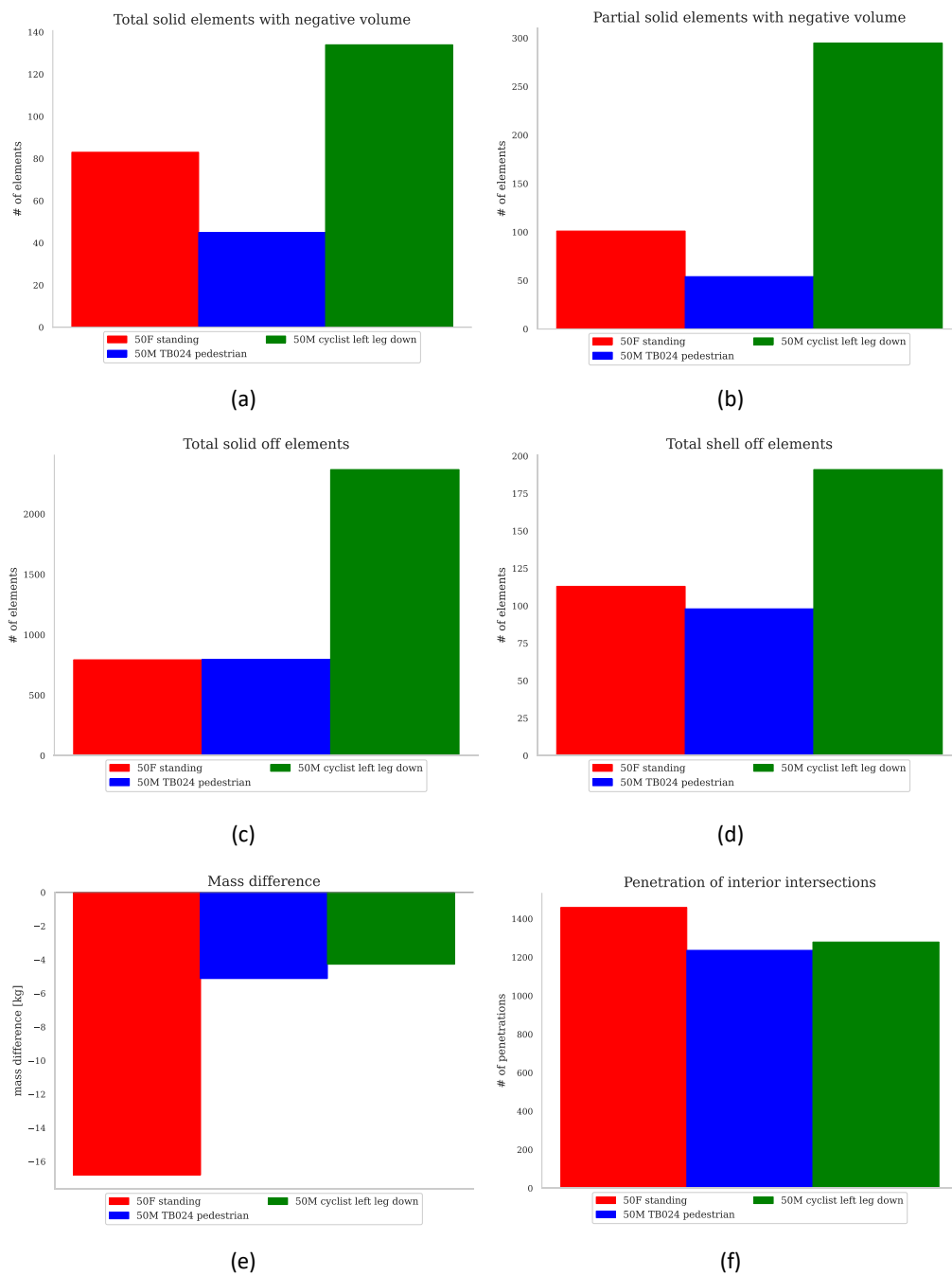


Figure 36: Morphing the 50M standing baseline model

Figure 37 shows body sites with intrusions when morphing from 50M standing to 50F standing. Especially the penetrations between pelvic soft tissue and abdominal muscle anterior (Figure 37 a) and between posterior thorax skin and scapula (Figure 37 b) are clearly visible.

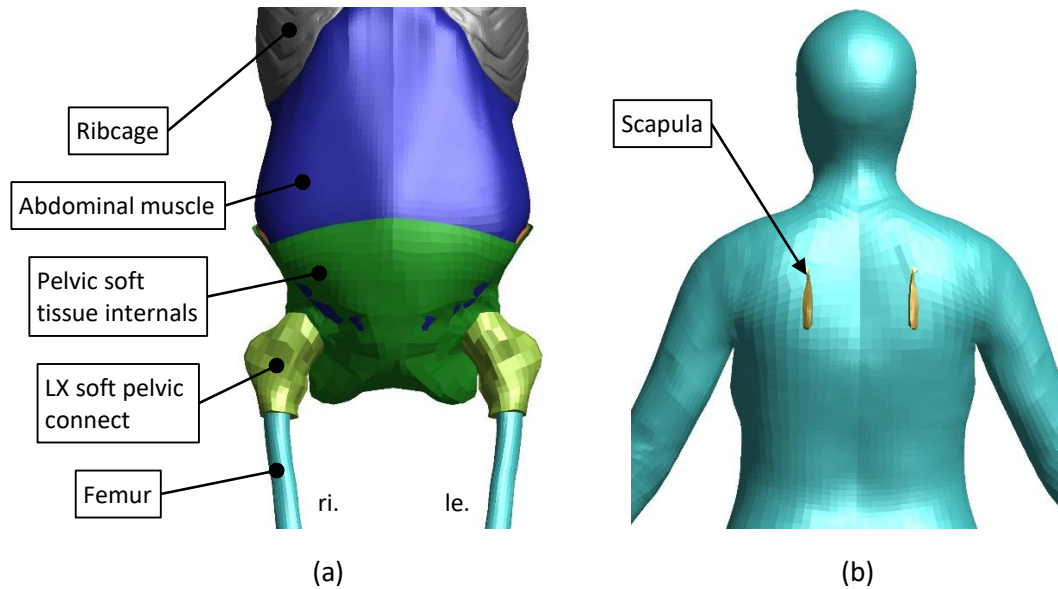


Figure 37: Morphed 50M standing to 50F standing

The result of the 50M standing morphed onto the 50M pedestrian is shown in Figure 38. This shows intrusions at the pelvic soft tissue anteriorly (Figure 38 a) and at the left LX soft knee anteriorly (Figure 38 b).

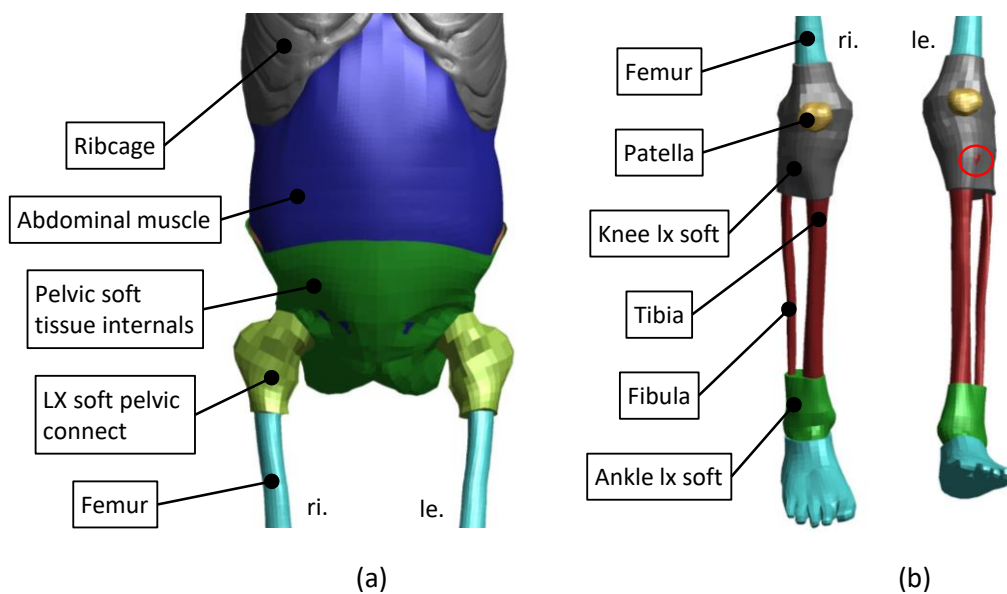


Figure 38: Morphed 50M standing to 50M TB024 pedestrian

The intrusions that occurred when morphing the 50M standing baseline model to the 50M cyclist with left leg down are shown in Figure 39. There were intersections of the pelvic soft tissue internally with abdominal muscle anteriorly and the right knee LX soft with the femur anteriorly (Figure 39 a). In addition, there were intrusions between the LX soft pelvic connect and hip ligament, and the pelvic soft tissue internals with pelvic bone and muscle cranial (Figure 39 b).

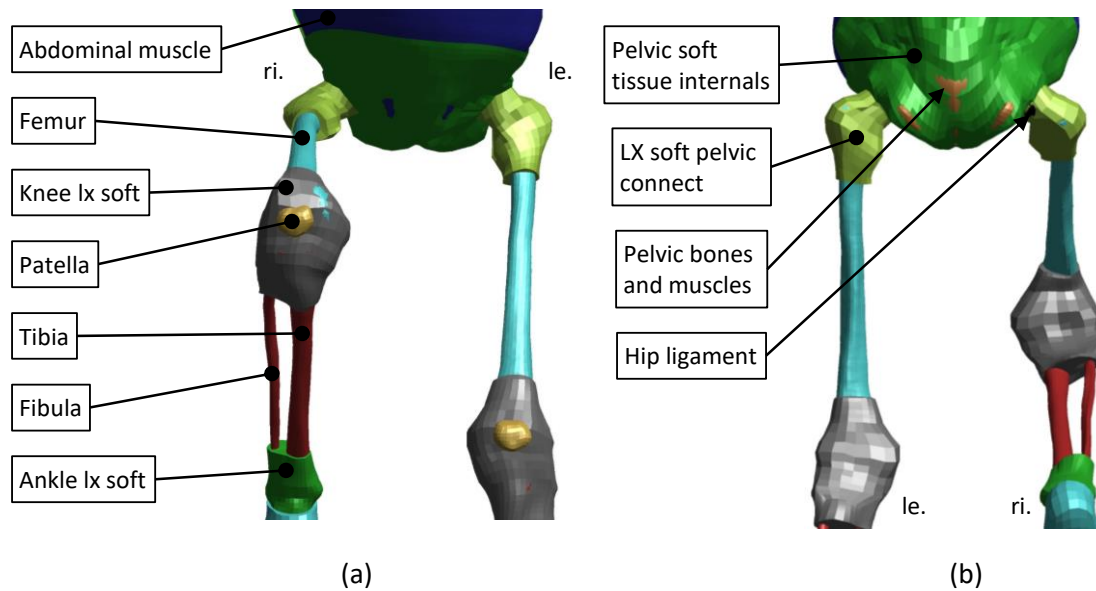


Figure 39: Morphed 50M standing to 50M cyclist left leg down

Results

Starting from the 50M seated baseline model, the 50F seated, the 50M pedestrian, and the 50M bicyclist were morphed with the left leg down. The resulting data is shown in Figure 40.

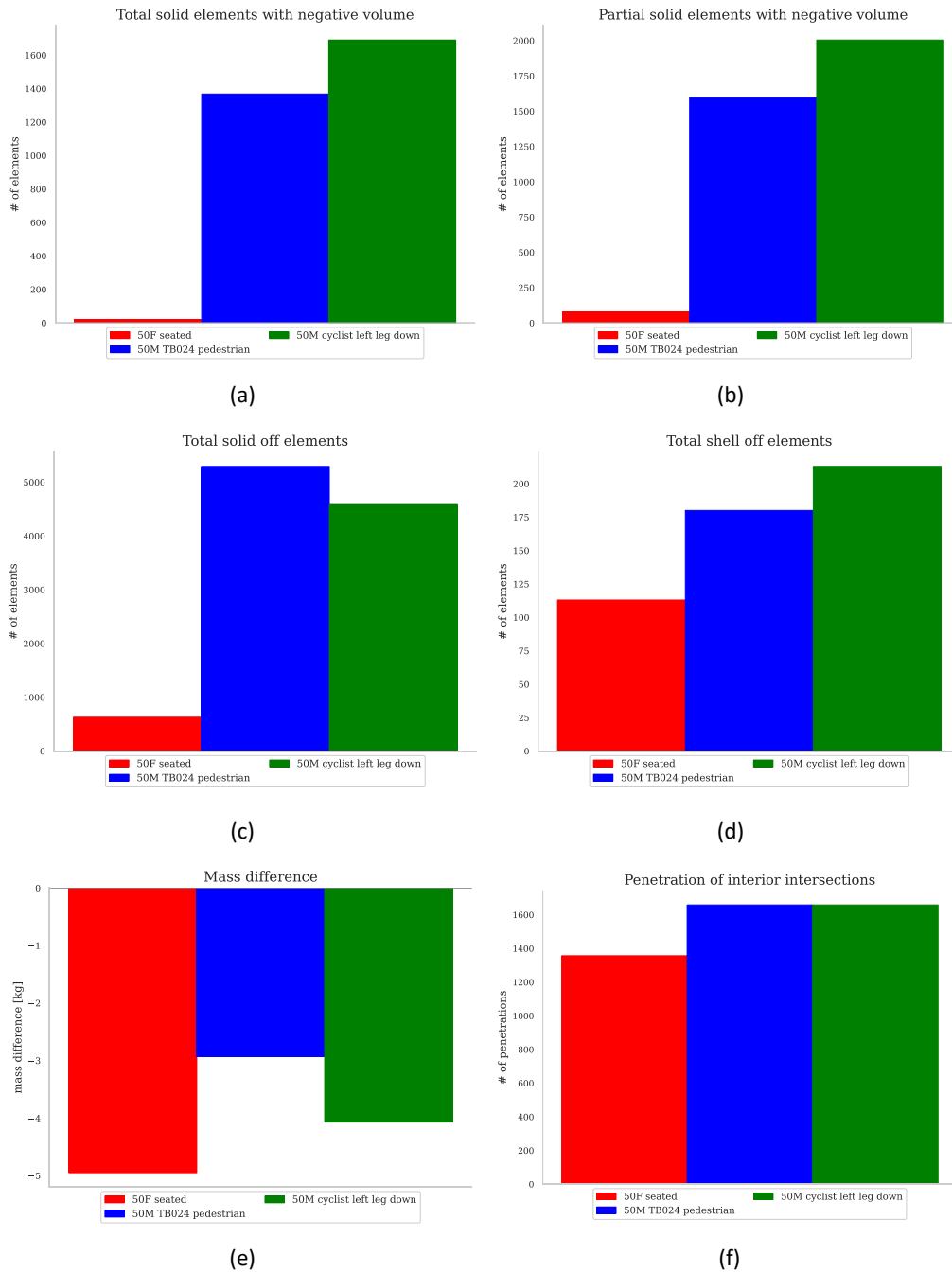


Figure 40: Morphing the 50M seated baseline model

In Figure 41, intrusions are visible on both sides of the anterior knee LX soft through the tibia bone (Figure 41 a) and on the anterior side of the thoracic skin through the clavicle bone and second rib (Figure 41 b). These were created during morphing of the 50M seated to the 50F seated.

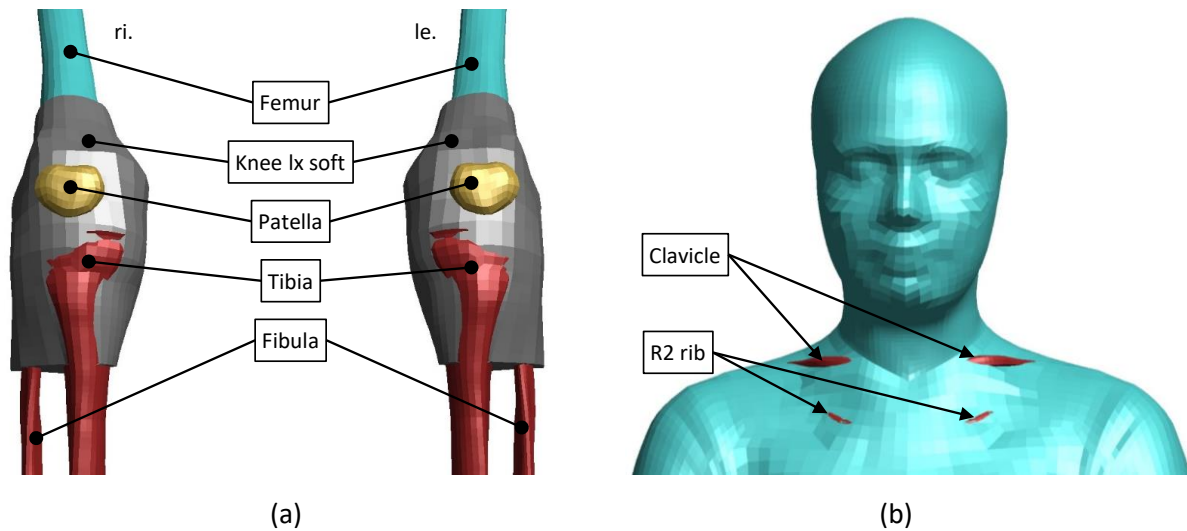


Figure 41: Morphed 50M seated to 50F seated

During morphing of the 50M seated to the 50M pedestrian, significant intrusions of the anterior knee LX soft and the leg skin through the tibia bone occurred on the lower leg (Figure 42 a). Furthermore, there were overlaps of the anterior humerus bone both with the UX soft tissue (Figure 42 b). At the anterior thoracic skin there was also overlap with the clavicle bone (Figure 42 c).

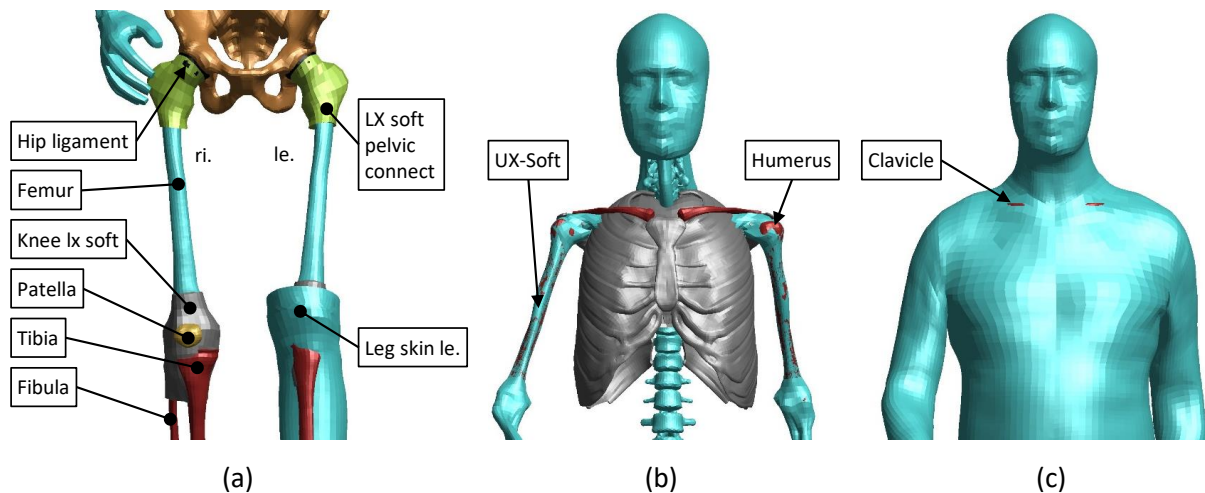


Figure 42: Morphed 50M seated to 50M TB024 pedestrian

Results

When the 50M seated was morphed onto the 50M cyclist with left leg down, intrusions occurred on the anterior lower legs. This caused the tibial bone to penetrate the knee LX soft tissue and skin of the lower legs on both sides (Figure 43 a and b). In addition, overlaps occurred on both sides of the posterior humerus with the UX soft tissue.

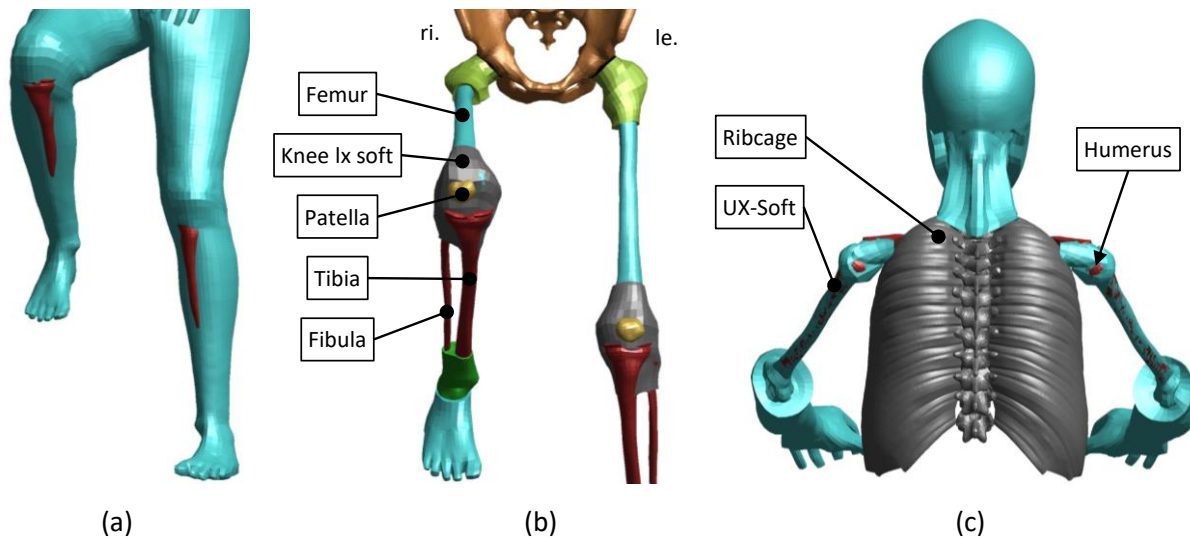


Figure 43: Morphed 50M seated to 50M cyclist left leg down

3.2 Comparison of different positions and body proportions

Using the morphed models from the previous chapter, comparisons were made here about results depending on the selected baseline model. For this purpose, the respective morphed models are compared to their target model of v. 0.2.5 and the conventionally positioned model of v. 0.3.0 in Figure 44 to Figure 47. For this purpose, the desired target model was kept constant and the baseline models were varied. A further explanation was given in chapter 2.2 (see also Figure 20Figure 19).

The number of solid elements with negative volume, the number of solid and shell off elements as well as masses were compared. In any case, manual reworking is required for all models where solid elements with negative volume have finally appeared. This applies to all morphed models. The conventional positioning of the target models of v. 0.2.5 as well as the positioning of the models in v. 0.3.0 were carried out by means of PIPER and positioning simulations using LS-DYNA, as briefly mentioned in chapter 1.1. It should be noted here that the number of positioning steps required can vary greatly. Depending on whether prior knowledge of the required joint angles of the HBM is known or not, this can greatly reduce the number of iterations required. For the positions used here, no prior knowledge of this was available, which is why the number of iterations to the final positioning was relatively high in some cases. For these positioning simulations a computational cluster was used. This cluster used Intel Xeon E5-2640 processors and a total of 1,180 CPU cores were available. There were 8 GB RAM per CPU core respectively 160 GB RAM per node. Each positioning iteration was simulated with two computational nodes and a total of 40 processors. The used solver version was LS-Dyna R9.3.0 mpp single precision. Each simulation took between 10 to 12 hours. The manual preparation and post-processing for a new iteration usually took about 30 minutes each. When checking the internal contact conditions of the model, more initial penetrations also occurred in the morphed model than in the conventionally positioned model.

Figure 44 shows a comparison for the 50F cyclist position. In it, the 50F standing and the 50F seated are selected as baseline positions. In addition, the 50F seated was morphed to the 50F standing and then further morphed to the cyclist position for comparison. The conventional positioning of the v. 0.2.5 target model and the v. 0.3.0 comparison model each required four iterations to achieve the desired result. The morphed models each used the recommended basis function called 'func_added' in the Python script and a function parameter of $r=0.1$. It can be seen throughout that the number of solid elements with negative volume as well as the number of solid and shell off elements are significantly higher than in the conventionally positioned v. 0.3.0 model. In some morphed models, a similar number of solid and shell off elements resulted as in the v. 0.2.5 target model used.

Results

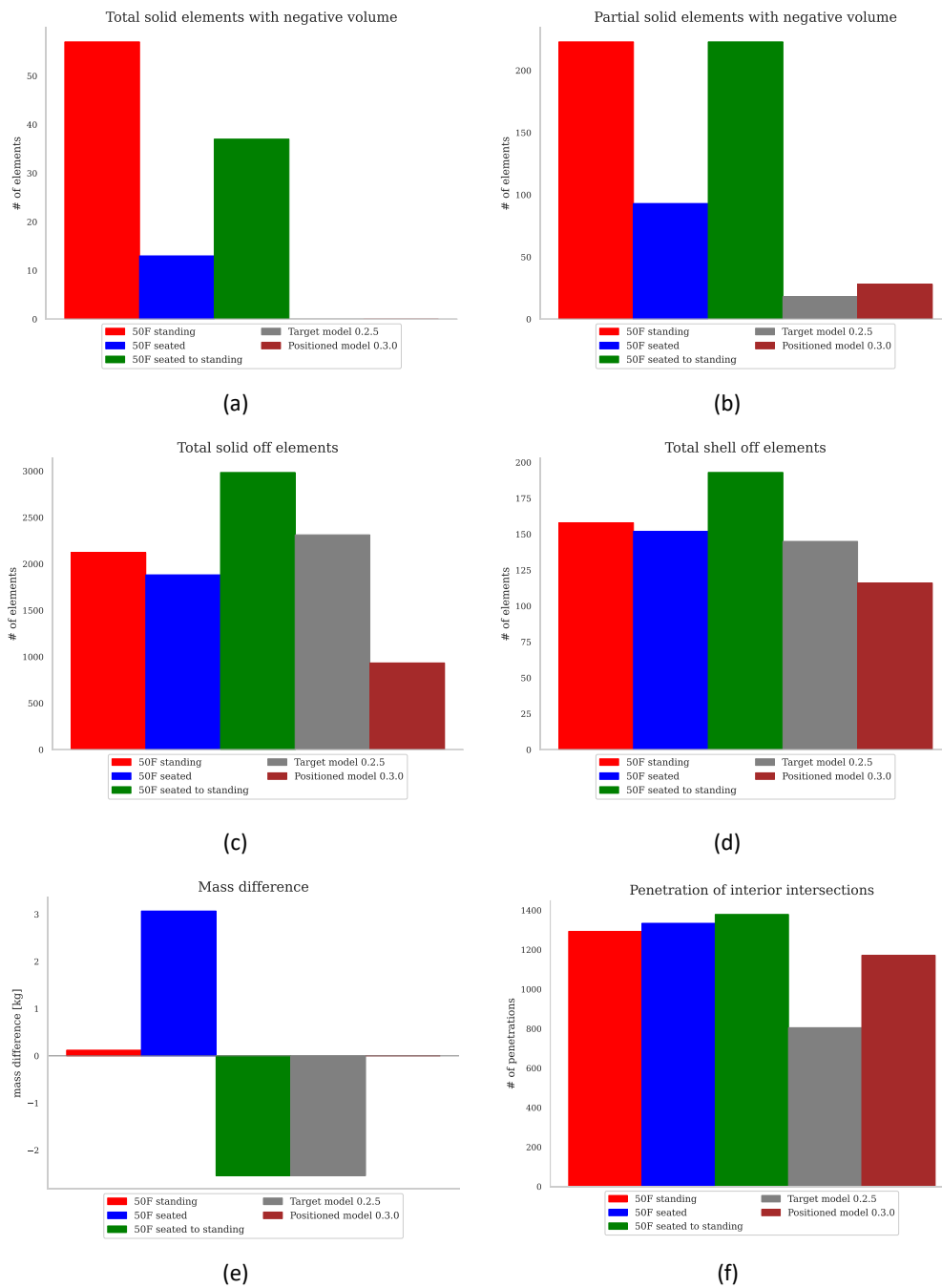


Figure 44: Comparison of morphed 50F cyclist model with regards to baseline models

Comparative values of the morphed 50F in pedestrian position are given in Figure 45. As before, once the 50F sitting, once the 50F standing and once the 50F morphed from sitting to standing were used as baseline models. The conventional positioning of the v. 0.2.5 target model required three iterations and that of the v. 0.3.0 comparison model required two iterations. The morphed models again contained solid elements with negative volume, which must be corrected by manual rework in any case. The element qualities of the conventionally positioned comparison model of the v. 0.3.0 generation were also better than with the morphed models. However, the quality of the v. 0.2.5 target model could be reached or partly exceeded.

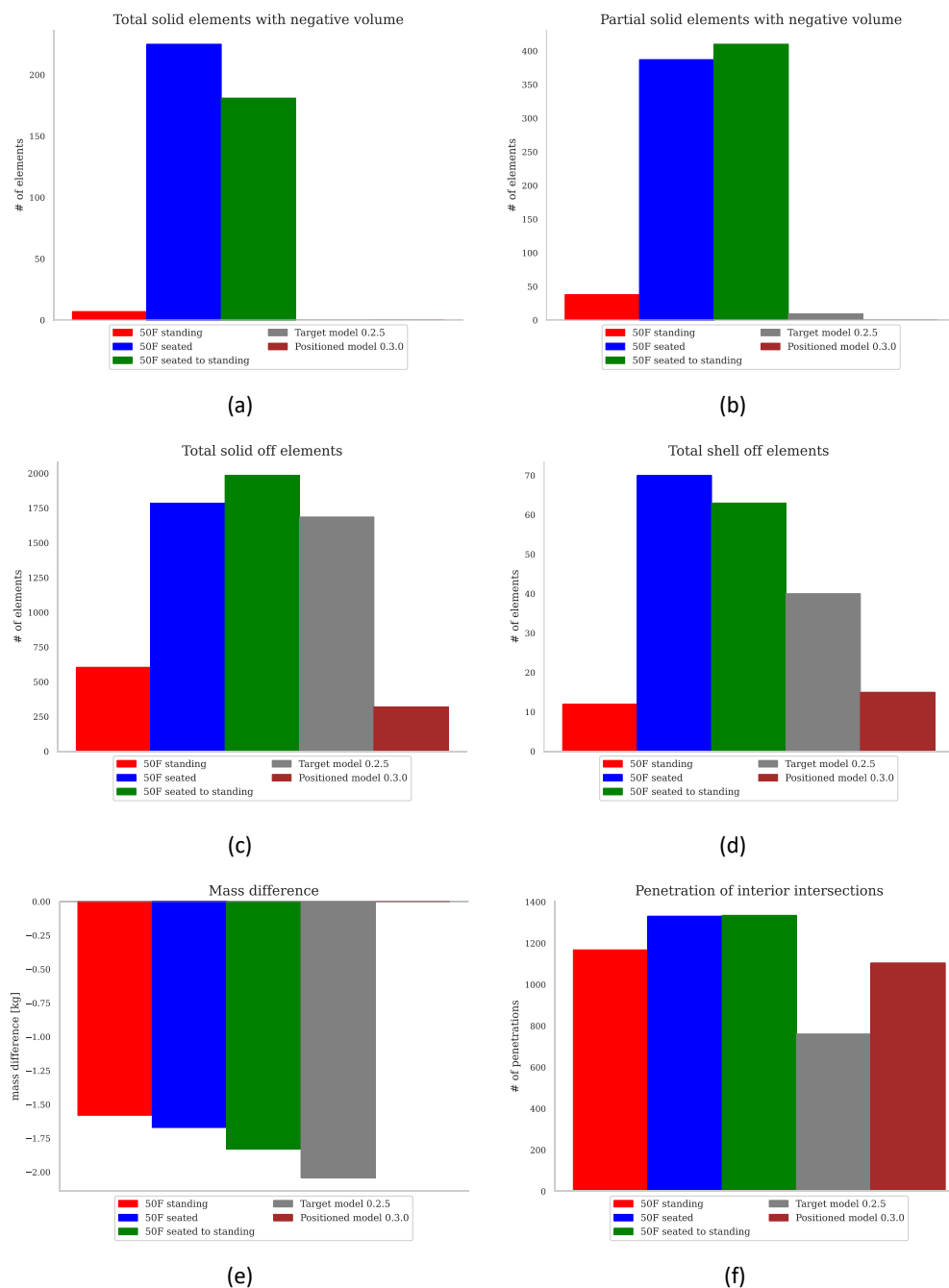


Figure 45: Comparison of morphed 50F TB024 model with regards to baseline models

Results

In the two comparative cases shown, where the 50F sitting was first morphed to the 50F standing and subsequently morphed to the desired target position, the results were each worse than when morphing directly from a baseline configuration.

Figure 46 and Figure 47 show, analogous to those above, the results for morphing to the target models of the 50M cyclist with left leg down and the 50M pedestrian. Both times the baseline models of the 50M were compared in sitting and standing baseline configurations. Again, the conventionally positioned model outperformed the morphed models in the relevant comparison criteria.

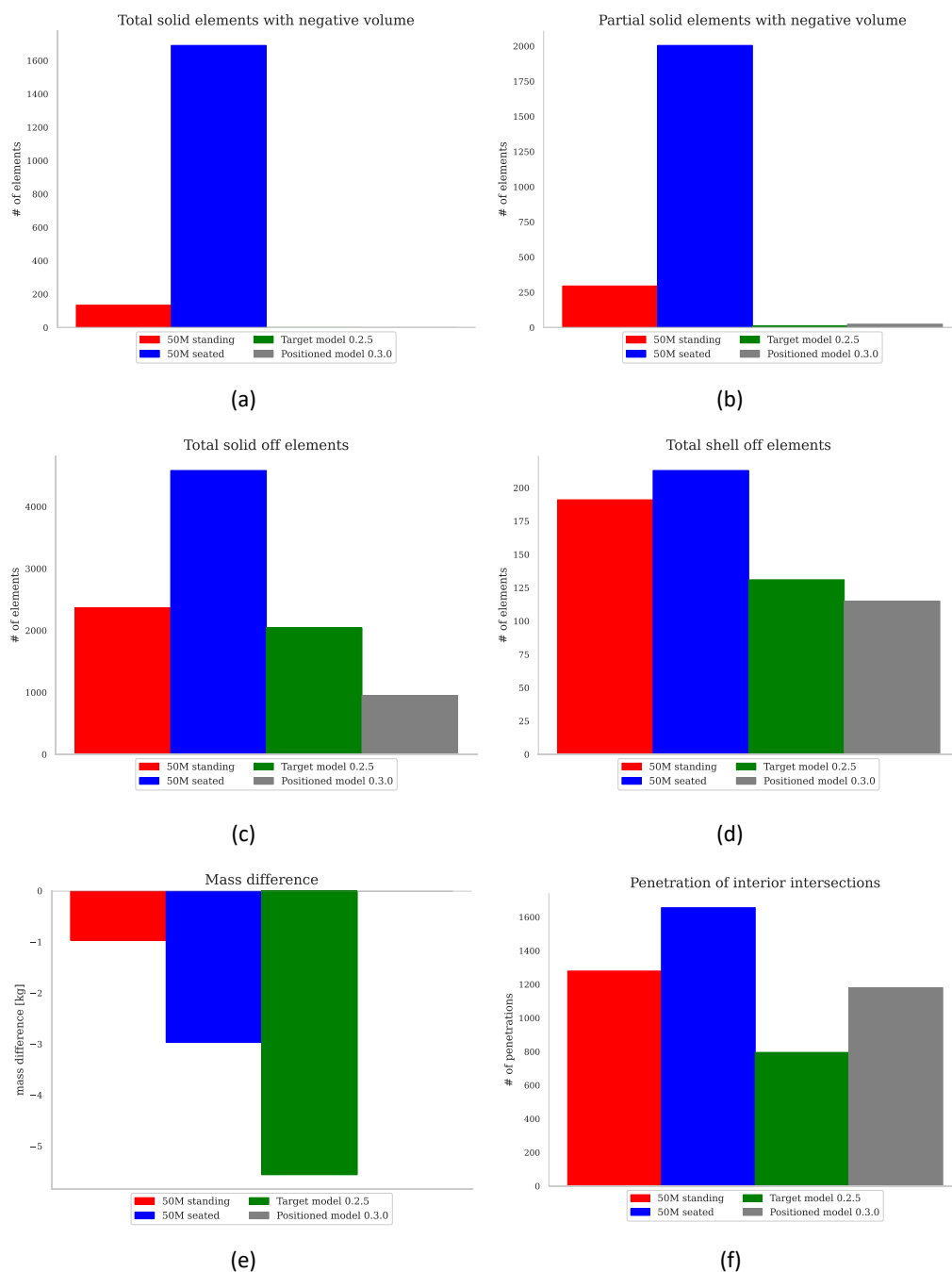


Figure 46: Comparison of morphed 50M cyclist model with regards to baseline models

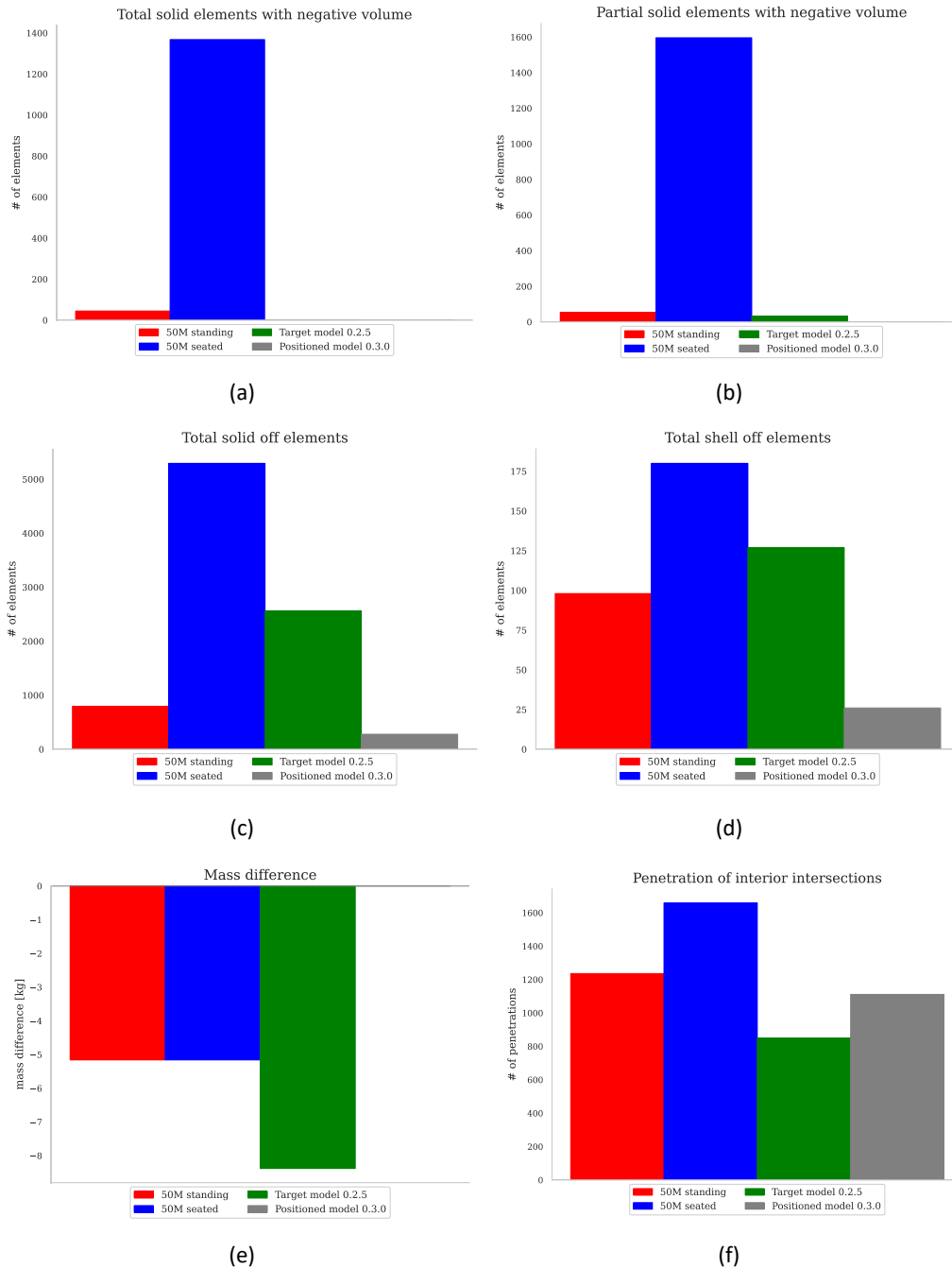


Figure 47: Comparison of morphed 50M TB024 model with regards to baseline models

In Figure 46 (e) and Figure 47 (e), a high mass difference between the v. 0.3.0 baseline and the v. 0.2.5 target model can be seen. This will be discussed further in chapter 4.2. In addition, it can be seen that significantly worse results were obtained when using the 50M seated as baseline than when using the 50M standing. In Figure 46 and Figure 47 the numbers of solid elements with total (a) and partial (b) negative volumes, as well as the number of solid off elements (c) were significantly higher when using the 50M seated as baseline.

3.3 Use of different PC systems

The behavior of the final Python script was tested on two different computer systems. For this, the 50F seated was morphed to the 50F cyclist with left leg down. On each PC several runs were performed. This allowed comparison between two different systems and reproducibility of a single system. On both test systems, the Python code used and the Python interpreter (Python 3.8) were identical. Baseline and target node files, as well as the required node sets were also the same. Run time, mass as well as element qualities were recorded. The evaluation of the elements was also performed with ANSA v22.0.1. The various PC specifications are listed in Table 12.

Table 12: PC systems for comparison

Criteria	System 1	System 2
Central Procession Unit (CPU)	Intel® Core™ i5-8500	AMD Ryzen 5 2600
CPU cores/threads	6/6	6/12
CPU base/max. frequency	3.00 GHz/4.10 GHz	3.4 GHz/3.9 GHz
Random Access Memory (RAM)	8 GB, single channel used	32 GB, quad channel used
RAM speed	2666 MHz	2933 MHz
Operating system	Microsoft Windows 10 Enterprise	Microsoft Windows 10 Pro
Version	10.0.19044 Build 19044	10.0.19044 Build 19044
System type	64-Bit	64-Bit
Outsourcing to the SSD in RAM shortage	Yes	No
Normal PC usage possible during morphing	No, temporarily excessive RAM utilization.	Yes

Table 13 shows the results of the test runs of both computer systems. It turned out that the results were identical for the two tested systems. Even when repeated several times on the same PC, the results remained constant. The change in time requirements is due to the simultaneous use of the PC for other tasks during the program runtime.

Table 13: Results from several morphing passes

Criteria	System 1			System 2			
Run	1	2	3	1	2	3	4
Duration	50 min 23 s	51 min 17 s	48 min 18 s	52 min 49 s	51 min 02 s	50 min 55 s	50 min 48 s
Mass	65.32 kg						
Solid elem. with neg. volume	13 Total 93 Partial						
Total solids off	1882 (0.359%)						
Total shells off	152 (0.062%)						

Several passes of a conventional positioning step were also performed for comparison. For this, only the lower extremities were brought into the desired end position in the almost completed 50F cyclist position with the left leg down. Small angle changes were applied in PIPER to the left hip joint, right knee, and right ankle. Subsequently, the same positioning simulation was performed with different hardware resources. For this purpose, one node with 20 CPUs, two nodes with 40 CPUs and three nodes with 60 CPUs were used. All other input parameters remained identical. It should be noted that this should only be a trend estimate. For an improved comparison, the entire model would have to be positioned completely with the respective hardware configuration. However, only the last positioning step was performed for a more efficient comparison. Using one computational node with a total of 20 CPUs, the shortest computing time was achieved. The results thus obtained gave the same amount of solid elements of negative volume as well as masses that hardly differed. The number of solid off elements differed between maximum and minimum values by 10% and that of shell off elements by 7.2%. The results when using different hardware configuration for the last positioning iteration are given in Table 14.

Table 14: Results using different cluster configurations

Criteria	Simulation 1	Simulation 2	Simulation 3
# of nodes	1	2	3
# of CPUs	20	40	60
Duration	15 hours 59 min	10 hours 1 min	11 hours 9 min
Mass	62.24 kg	62.30 kg	62.24 kg
Solid elem. with neg. volume	0 Total 28 Partial		
Total solids off	874 (0.167%)	796 (0.152%)	884 (0.169%)
Total shells off	111 (0.045%)	103 (0.042%)	107 (0.044%)

4 DISCUSSION

Experiences concerning the research question how morphing based on previously positioned models can be used for model maintenance have been found. It turned out that the free form deformation and inverse distance weighting approaches were not suitable for the required demands. Only an interpolation by means of a radial basis function provided satisfactory results. Also within this interpolation approach, different influencing variables were found. Thus, different results were obtained when varying the used basis function and the corresponding function parameter. In order to reduce the required calculations to the point where they can be performed by a standard computer, the morphing process had to be divided into several steps. However, by adding a new include file with the node sets used, these steps could be handled well.

Regarding the differences between morphed and conventionally positioned models, some findings can now be summarized. Conventionally positioned models showed the clear advantage of not having any elements with negative volume in them. These occurred in all morphed models, making manual reworking mandatory for them. In addition, a better mesh quality was achieved with the conventional approach. The model processing by means of morphing required almost no manual preparation and the computation times were also significantly lower than with the conventional simulations. It was also shown that using a single morphing step yielded better results than when split into two. This is shown in Figure 44 and Figure 45. The 50F seated was thereby first morphed to the 50F standing and only then to the searched target position. The results obtained were in any case worse than the direct morphing of the 50F standing to the respective target position (except for the solid elements with total negative volume, see Figure 44 a). Consequently, according to the current state of the landmarks and node sets used, major position changes should be performed in one morphing run. Intrusions do occur, but when the process is divided into several steps, these and other quality criteria are generally degraded. The manual post-processing effort is therefore strongly dependent on the resulting model quality after morphing. However, this varied significantly depending on the baseline model used. Therefore, a morphing attempt starting from different baseline models should be considered. If the resulting model quality of the morphed model was not significantly worse than that of the conventionally positioned model, an experienced user could correct it in a short time. However, if significant intrusions and poor model quality occurred, or if the user was not yet skilled in manual rework, significantly longer working times were required than with the conventional approach. However, in addition to the possible increased effort in manual rework and the associated expenditure of time, another problem arose. For the most part of the manual rework process, this step was not

automated, but the user manually moved nodes, e.g. to avoid intrusions or to improve element qualities. Since this manual node shifting by different users is not uniform, a repeatable model creation could not be guaranteed. In addition, it is also not possible to guarantee that even the same user would manually rework different models in the same way.

By model morphing using the radial basis function, the results from chapter 3 were obtained. Based on these results, some topics needed to be addressed. Especially intrusions, mesh quality and solid elements with negative volume were essential. Furthermore, the comparison between conventionally positioned models and morphed models was of great interest.

4.1 Intrusions, mesh quality and elements with negative volume

For the selected target positions, there were different results of model qualities with regards to intrusions and element quality of morphed models. At first sight, all conventionally positioned models of v. 0.3.0 appeared better than the respective morphed ones. There were no intrusions in them. In comparison, significant intrusions occurred in the morphed models, which have already been presented in chapter 3.1. Additionally, the mesh quality was also consistently better in the conventionally positioned models. This can exemplarily be seen in Figure 48. The comparison of different baseline models for the desired target model of the 50F cyclist with left leg down is shown below. Figure 48 (a) shows that the conventionally positioned model of v. 0.3.0 has significantly less solid off elements than the respective morphed models. The same applies to the number of shell off elements, which can be seen in Figure 48 (b).

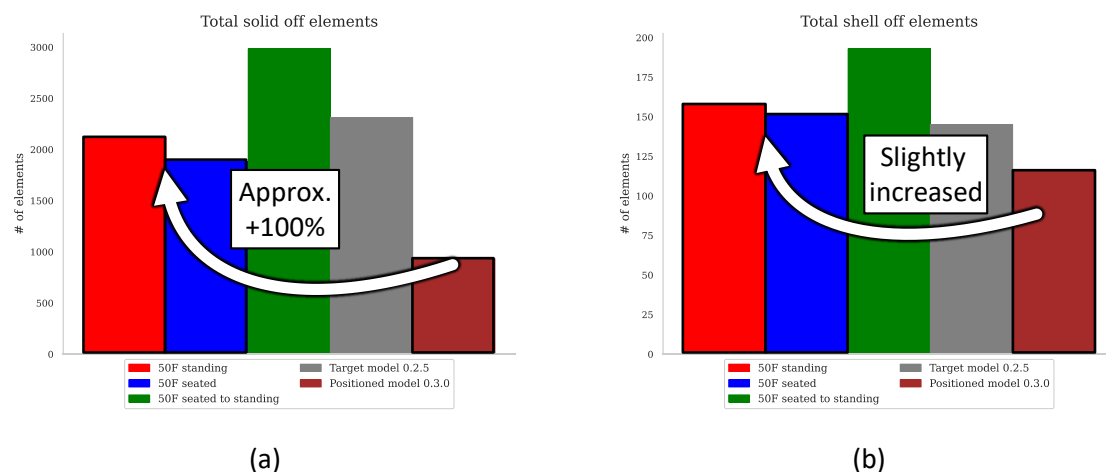


Figure 48: Mesh quality of 50F cyclist with left leg down

Nevertheless, morphed models outperformed some v. 0.2.5 target models. This can be shown exemplarily in Figure 49 when considering the 50F pedestrian. In it, the morphing of the 50F seated produced significantly fewer solids (Figure 49 a) and shell (Figure 49 b) off elements than in the corresponding target model of v. 0.2.5. One possible reason for this would be that no suitable control cards were used in the conventional positioning simulations. It is also possible that no internal damping was used during the simulations or that the selected simulation time was too short.

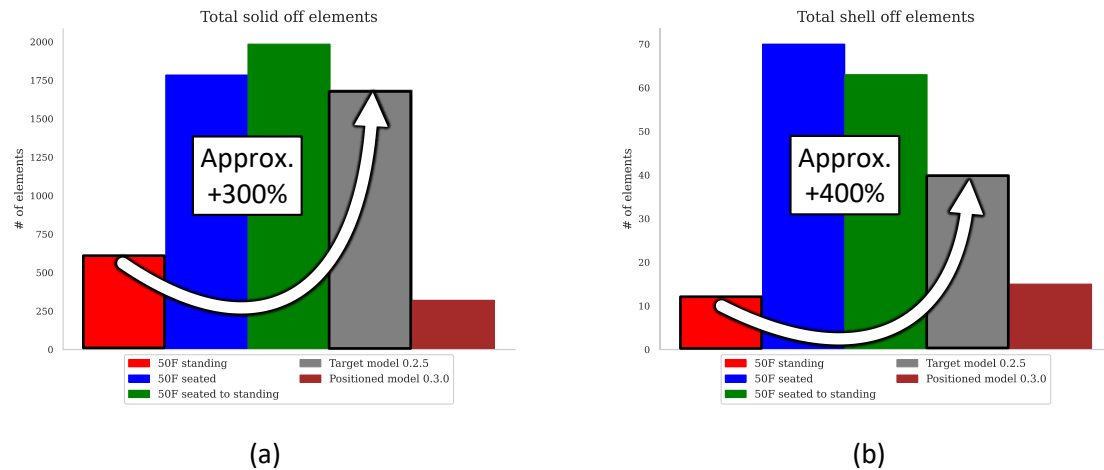


Figure 49: Mesh quality of 50F TB024 pedestrian

Besides the increased number of solid and shell off elements (see Figure 48 a and b), other issues occurred with morphed models compared to the conventionally positioned model. The most significant point in which morphed models were worse than conventionally positioned models concerns the solid elements with negative volume. Looking at Figure 50 in addition to Figure 48, the clear difference is visible. This shows that in the conventionally positioned models no solid elements with total negative volume occurred at all (Figure 50 a). In addition, there occurred also only a few solid elements with partial negative volume (Figure 50 b). In comparison, the morphed models show significantly higher numbers. Therefore, for all morphed results, mandatory rework was required with respect to solid elements with negative volume.

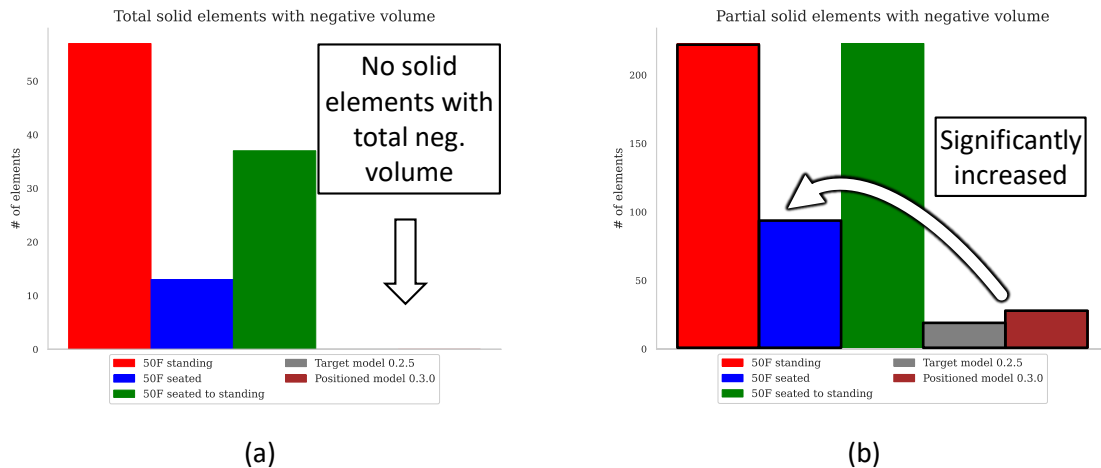


Figure 50: Solid elements with total/partial negative volume in 50F cyclist left leg down

When checking the models for internal contact violations, possibilities for improvement were also noticed. In some cases, positioning simulations of the conventionally positioned models were not feasible. Problems occurred due to initial penetration from the previous iteration step. This had the consequence that conventionally positioned models of v. 0.3.0 had also to be reworked manually in this respect. If this was not done, the models could possibly experience instabilities when used in simulations. Besides, all the morphed models had to be reworked manually with respect to internal contact conditions to further ensure a stable simulation process too. However, fewer initial penetrations occurred in the models positioned by simulations than in the morphed models. Therefore, less manual rework was necessary in the conventionally positioned models. Figure 51 shows the initial penetrations of the morphed cyclist positions of the 50F (a) and the 50M (b). It can be seen that the initial penetrations in the conventionally positioned models are in any case lower than those of the morphed models. Depending on the baseline model used, this difference can be larger or smaller. For example, when using the 50M seated as baseline model for morphing the 50M cyclist positions, significantly more penetration occurred than when using the 50M standing (see Figure 51 b).



Figure 51: Initial penetrations in the morphed left leg down cyclist position of 50F (a) and 50M (b)

The effort for manual rework with respect to intrusions strongly depended on their extent. The size and number of intrusions varied depending on the baseline model used. For example, significantly fewer intrusions occurred when morphing the 50F standing to the 50F pedestrian position than when using the 50F seated as baseline. Figure 52 shows the intrusions created using the mentioned baseline models. It can be seen that when morphing the 50F standing, intrusions at the knee between LX soft and tibia were created (Figure 52 left side). When using the 50F seated as baseline (Figure 52 right side), intrusions also occurred at the same location, but more severe. In addition, intrusions were created at the hip ligament, the left tibia and the left forearm. Accordingly, the manual rework to revise these intrusions would take significantly more time than starting from the 50F standing model. One possible reason could be the large change in posture on the relevant body parts. The posture of the arms and legs differs significantly more between seated and pedestrian position than between standing and pedestrian position. Since this is exactly where additional intrusions occurred, this could reinforce the possible cause. Another reason could be inappropriate selected combinations of landmarks and associated node sets of these body regions. In addition, an incorrect morphing sequence and thus incorrect prioritization of the landmarks of bone and skin could have led to this poorer result. This possibility will be discussed in more detail in chapter 4.2.

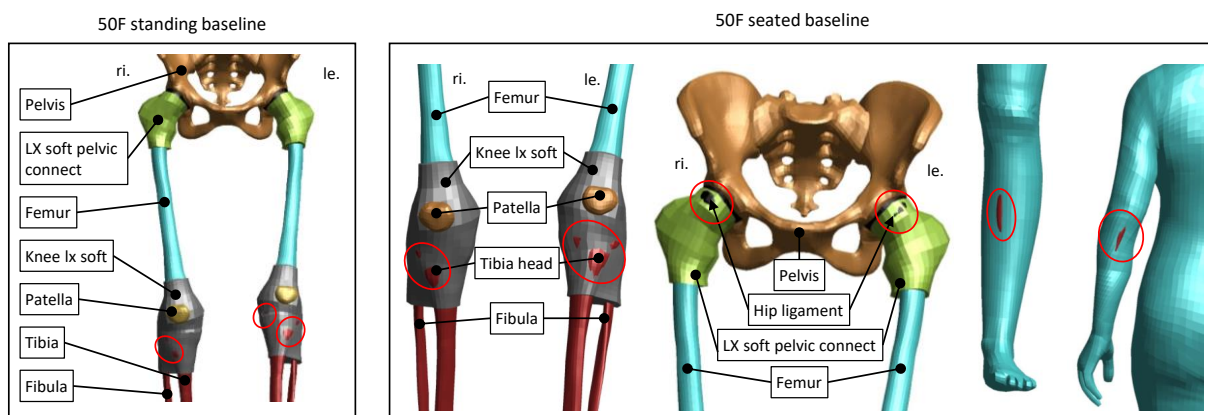


Figure 52: Morphed 50F TB024 pedestrian from 50F seated and standing baseline models

Certain conclusions can be drawn from the results above. Depending on the baseline model used, different qualities of the morphed model can arise. Here, the result of the morphed 50F cyclist position was best when created from the 50F seated baseline position. In contrast, the result of the 50F pedestrian positions was best when morphed from the 50F standing baseline position. In contrary, for the male target models, the results were better when morphed from the 50M standing baseline position. This can be explained by the unchanged use of the combinations of landmarks and associated node sets for all morphing runs. This means that for all combinations of baseline and target models, always the same morphing parameters were used. For the creation of the morphing script, mainly the combination of 50F seated baseline and 50F cyclist target was considered. Based on this, a large

number of landmarks with associated node sets were created. Later on, by considering other baseline and target configurations, these combinations were modified or new ones were added. Consequently, this may account for a difference in the use of male and female models. In order to describe this circumstance more precisely, further adjustments and optimizations of the selected combinations should be made. Since the selection of the landmarks and their associated node sets are based on experiments, a further improvement through testing could potentially be achieved. Possibly, combinations could be found which provide equally good results for all baseline and target configurations.

During the compilation of the results of this thesis, new optimization approaches have been noticed. These are explained in more detail in the following section.

4.2 Limitations and outlook

From the results presented above and experience of model handling by morphing using a landmark based radial basis function, several peculiarities can be noted. With the exemplary results given in chapter 3 the use of morphing for small as well as for large geometry changes between baseline and target model was shown. This could be done in one calculation step using the resulting Python script. The use of a separate include file with the corresponding node sets made the handling with different models much easier and saved time. This also resulted in the possibility to use different baseline models and different target models. The total duration of morphing a complete model only took about 50 minutes. Compared to a single simulation step that took around 10 to 12 hours a time saving was achieved. Therefore, multiple models could also be processed in a relatively short time. Reproducibility also proved to be a positive feature of the morphing approach. The results were not only repeatable on one computer system, but could also be repeated on a second test system. In contrast to this, however, the need for manual reworking was in some cases significantly high. This not only greatly increased the total time required, but also severely limited reproducibility. The conventional positioning method using simulation showed comparatively high fluctuations in results (see chapter 3.3). Especially when using different hardware configurations. In this experiment, only the last positioning step was performed with different hardware configuration, so the results cannot be compared directly. For a better comparison, a completely positioned model with each hardware configuration should have been used. However, possible fluctuations in the results were shown with changing the hardware configurations only for the last simulation step. Nevertheless, the resulting values should not be seen as absolute. To minimize the influence of different hardware configurations the input control cards could be optimized and the number of nodes and CPUs used could be fixed. The largest limiting factor for morphed models was the model quality. The baseline models could be changed much faster than with conventional approaches. However, significantly more manual rework

was required to compensate for the lost model quality. This effort strongly depended on the respective final result. As also noted in chapter 4.1, the intrusions that occurred varied greatly. One possible reason for this could be that no perfect combination of landmarks and node sets could be found that gives good results for all combinations of baseline and target models. Especially for strongly differing baseline and target configurations intrusions occurred. From this, it could be concluded that with the current morphing script, smaller differences in posture can be better represented than large ones. For further improvement, significantly more target models would have to be tested. Consequently, the node sets would have to be adapted again for the implementation of a new target model.

To enable a possible additional improvement of the results, a further variation of the basis function would also be conceivable. Analogous to the results presented in chapter 3 regarding the femoral head, a variation of the basis function for the full model would be possible. In this way, the course of the model quality could be recorded depending on the selected basis function and the associated function parameter 'r'. Due to the time-consuming nature of this step, it was not performed in this work.

Another limitation of this approach is that a baseline and a target model of v. 0.2.5 must be available in any case. This also means that a model of v. 0.3.0 can only be brought to positions that were already created manually in the previous model series. Consequently, to create a model of v. 0.3.0 using the resulting morphing script to a new position, a model of v. 0.2.5 would first have to be positioned to that in the conventional way. Instead of spending this amount of time, however, one could also directly move the v. 0.3.0 model into the desired position using a conventional approach.

Along with the problem that target models of v. 0.2.5 must be available, there was also another issue discovered. By morphing the baseline model to a known target model, an attempt is made to reach the target position. However, if there were areas in the baseline model that had changed in the new model generation, these may not have been morphed correctly. Exemplarily this can be shown by the change of the masses. In v. 0.2.5 the 50F standing had a weight of 59.99 kg and in v. 0.3.0 it has 62.57 kg. As can be seen in Figure 53, all morphed models have a lower mass than the conventionally positioned model of the 50F TB024 pedestrian. This is because the target model of v. 0.2.5 already had a lower weight of 60.59 kg. The masses of the morphed models came close to the weight of the target model.

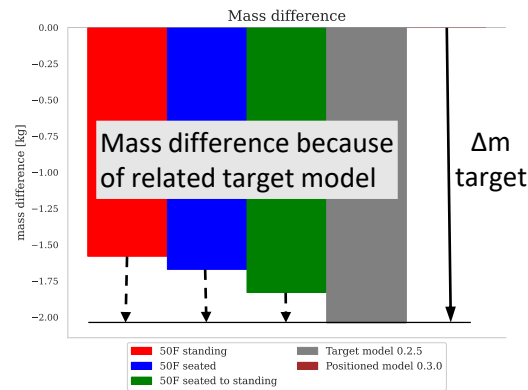


Figure 53: Mass difference compared to conventional positioned model

Another peculiarity of morphing applies to the problem of the emerging mass difference mentioned above. As described in chapter 2.1, only the geometry of the baseline model is changed by morphing. Thereby, three-dimensional displacements of the nodes of the model occur. These nodes define elements. The resulting elements build up the parts of the model. With this procedure, it can result in significant changes of the volume of a part. Since the material properties (e.g. density) are not changed or taken into account by morphing, this can also lead to a change in weight.

As briefly mentioned before, new optimization approaches were found during the preparation of the results. These arose mainly from the order of the body parts to be morphed. In addition, the choice of the landmark nodes from v. 0.2.5 could still have significant influences on occurring intrusions. Two concrete examples are given for this. The former is about the morphing of the 50F seated to the 50F TB024 pedestrian position. This resulted in significant intrusions on the left lower leg anteriorly and the left forearm posteriorly (see Figure 34). Accompanying these intrusions was a relatively high number of solid elements with negative volume. The second example is about the morphing process of the 50M seated to the 50F seated. There was significant overlap between clavicle bone, second rib bone and thoracic skin anteriorly (see Figure 41). Besides the two examples given, the following solution approach could be helpful for all intrusions between bone and outer skin. For this, it might make sense to change the morphing order and thus the priority of the landmark nodes. In the current version of the morphing script, landmarks of skin and bone are given equal importance. This means that after morphing the skin, it is assumed to be locally fixed. Therefore, the nodes of the skin are also locally fixed. The same applies to the bones and their associated nodes. Only after the skin and bones have been morphed, the parts in between can be changed. However, it turned out to be problematic if there were already overlaps between bones and skin. For this reason, a new approach with differently weighted landmarks could remedy the situation. One possibility would be to morph the bones first and only then the skin. For the morphing process of the skin, already created bone surfaces could be considered afterwards. Consequently, the landmarks of the bones would have a higher

importance than those of the skin. So the skeleton has to be created first and all further steps have to consider this for the calculation of the respective local transformations. In the current version of the morphing script, these interactions are not taken into account.

In addition to the problematic overlap of bone and skin, another issue was identified. The second problem lies in the procedure of morphing itself. In it, namely, only the geometry of the model is taken into account. As already explained, no information internal to the model is considered. Therefore, no contact conditions or node affiliation to different parts are recognized and respected. For this reason, it is not recognizable for the current script whether the computed transformation results in an intrusion or not. For this detection, affiliations to different body parts would have to be known. This information could be considered in the future. The knowledge about the affiliation of the nodes could be used to treat different parts more separately from each other and thus to separate transitions between them more sharply. It could also be used to shift intrusions after the morphing process is completed. This subsequent penetration check would also be conceivable in addition in the Python script. Two options could be considered for this. Either a subsequent penetration check could verify the morphed model after it has been fully morphed. In this case, any intrusions that may have occurred could be corrected by subsequently moving the nodes. On the other hand, even after smaller morphing steps (e.g. after an arm has been completed), this body region could be checked individually. Furthermore, it would be conceivable that this kind of checking could also be done after each sub-step within a body part. In this way, after each morphed sub-part, any intrusions that may already have occurred could be corrected. A comparison of the mentioned possibilities on their effect would be of great interest and could be treated in future research.

With the current morphing script, fast processing is possible. However, the poor model quality of the morphed models is a major drawback of this approach. Significantly more target positions would have to be tested and at the same time the node sets used would have to be adjusted iteratively. This could enable an improvement of the model quality and reduce occurring intrusions. Alternatively, one could also specialize on a certain combination of baseline and target. In this case, the optimization of the node sets would be more straightforward.

Within the scope of this work, the models created were mainly checked for their geometric quality. No validation simulations with the morphed models were performed. In order to make further statements about the usability of the morphing approach, additional steps should be carried out. The morphed models should further be compared to conventionally positioned models. For example, the morphed 50F pedestrian could be compared to the conventionally positioned model of v. 0.3.0 when used in the same simulation. This would allow results and model behavior to be recorded and compared during simulation.

In addition to further improvements and comparison when used in simulations, other future research questions are conceivable. Currently, an already created model from v. 0.2.5 is always required for the calculation of the transformation for v. 0.3.0. However, not all nodes are required from the model of the previous generation, but only the relevant landmarks. Therefore, it would be conceivable not to use a complete model as a target, but only one that contains the relevant landmarks. For this purpose, a generically generated model consisting only of the skeletal surface and nodes of the skin would be sufficient. This reduced model could be adapted to the desired position in advance. In doing so, a pure rigid-body movement of the bones would be possible by means of transformations. This model could then serve as a target model for morphing. This would allow the current generation model to be positioned without the need of a complete predecessor model.

5 CONCLUSIONS

From the results obtained, the following conclusions were drawn. The interpolation using the radial basis function proved to be most suitable. Thus, models of the VIVA+ from v. 0.3.0 could be positioned using models of v. 0.2.5. Adding a new include file to the VIVA+ model, with the node sets used for morphing, significantly reduced the manual workload. The quality of the morphed models varied greatly. Depending on the baseline models used, better or worse results were obtained. Solid elements with negative volume were present in all morphed models and needed manual correction. The morphed models had consistently lower model quality than conventionally positioned models by default. In addition, significant intrusions occurred in some cases. This resulted in a considerably increased manual reworking effort. Since the need for manual rework also occurred with conventionally positioned models, this aspect does not make morphed models unsuitable for the task of model modification. Taking the reduced necessary preparation and computation time into account (compared to the conventional approach), morphing has the potential to reduce the overall time for repositioning. Nevertheless, manual rework not only increases the total time required, it also inherently reduces the achievable reproducibility, which was one of the advantages of the morphing approach in the first place.

Especially large rotations are challenging for the morphing algorithm and cause more manual work. In cases with minor posture changes (e.g. standing to pedestrian), the developed script with the fine-tuned algorithms worked very well.

In the future, further improvements could be achieved by optimizing the node sets used. In particular, intrusions could be further reduced by considering new target models. Taking model-internal information into account could also bring improvements. This would make it possible to determine the node affiliation to elements and parts and to counteract intrusions and elements with negative volumes. These additional measures to check the morphed model for internal penetrations could be addressed in future investigations.

Furthermore, additional comparisons between conventionally positioned models and morphed models would be useful. The behaviour of the two models as well as the generated results when used in the same simulation environment should be evaluated in future studies.

6 REFERENCES

- Ansys LS DYNA (2022). *Ansys LS DYNA / Crash Simulation Software*. Accessed April 12, 2022, <https://www.ansys.com/products/structures/ansys-ls-dyna#tab1-2>
- BETA CAE Systems (2021). ANSA User Guide: ANSA version 22.0.x User Guide. Updated in September 2021.
- Boin, M. (2018). "Occupant Protection in Alternative Seating Positions," in *15th German LS-DYNA Forum*, ed. DYNAmore.
- Bose, D., Segui-Gomez, M., and Crandall, J. R. (2011). Vulnerability of Female Drivers Involved in Motor Vehicle Crashes: An Analysis of US Population at Risk. *Am J Public Health* 101, 2368–2373. doi: 10.2105/AJPH.2011.300275
- Carr, J. C., Fright, W. R., and Beatson, R. K. (1997). Surface interpolation with radial basis functions for medical imaging. *IEEE Trans Med Imaging* 16, 96–107. doi: 10.1109/42.552059
- Consumer Reports (2019). *The Crash Test Bias: How Male-Focused Testing Puts Female Drivers at Risk*. Accessed March 09, 2022.926Z, <https://www.consumerreports.org/car-safety/crash-test-bias-how-male-focused-testing-puts-female-drivers-at-risk/>
- Decker,, W., Koya, B., and Gayzik, S. F. (2018). "Validation of Detailed Organ Modularity in a Simplified Human Body Model," in *2018 IRCOBI Conference Proceedings*, ed. International Research Council on the Biomechanics of Injury (IRCOBI), 342–354.
- Economic Commission for Europe of the United Nations (2011). *UN Regulation No 95 - Uniform provisions Concerning the Approval of Vehicles with regard to the protection of the occupants in the event of a lateral collision: UN Regulation No 95*.
- Economic Commission for Europe of the United Nations (2012a). *Regulation No 94 - Uniform provisions concerning the approval of vehicles with regard to the protection of the occupants in the event of a frontal collision: UN Regulation No 94*.
- Economic Commission for Europe of the United Nations (2012b). *UN Regulation No 127 - Uniform provisions concerning the approval of motor vehicles with regard to their pedestrian safety performance: UN Regulation No 127*.
- Economic Commission for Europe of the United Nations (2015). *UN Regulation No. 135 - Uniform provisions concerning the approval of vehicles with regard to their Pole Side Impact performance: UN Regulation No. 135*.
- Economic Commission for Europe of the United Nations (2020). *UN Regulation No 137 – Uniform provisions concerning the approval of passenger cars in the event of a frontal collision with focus on the restraint system [2020/]: UN Regulation No 137*.

Euro NCAP (2021). TB 024 - Pedestrian Human Model Certification v3.0: Version 3.0.

Euro NCAP | Roadmap 2025.

Fu, W., Lee, J., and Huang, H. (2021). How has the injury severity by gender changed after using female dummy in vehicle testing? Evidence from Florida's crash data. *Journal of Transport & Health* 21, 101073. doi: 10.1016/j.jth.2021.101073

GHBMC (2022). *About Us - GHBMC*. Accessed March 10, 2022.186Z, <http://www.ghbmc.com/about-us/>

Górniak, A., Matla, J., Górniak, W., Magdziak-Tokłowicz, M., Krakowian, K., Zawislak, M., et al. (2022). Influence of a Passenger Position Seating on Recline Seat on a Head Injury during a Frontal Crash. *Sensors (Basel)* 22. doi: 10.3390/s22052003

Hu, J., Fanta, A., Neal, M. O., Reed, M. P., and Wang, J.-T. (2016). "Vehicle Crash Simulations with Morphed GHBMC Human Models of Different Stature, BMI, and Age," in *Proceedings of the 4th International Digital Human Modeling Symposium (DHM2016)*, ed. International Digital Human Modeling Symposium (Montréal, Québec, Canada).

Hu, J., Zhang, K., Reed, M. P., Wang, J.-T., Neal, M., and Lin, C.-H. (2019). Frontal crash simulations using parametric human models representing a diverse population. *Traffic Inj Prev* 20, S97-S105. doi: 10.1080/15389588.2019.1581926

Humanetics (2022). *Home*. Accessed March 09, 2022.475Z, <https://humanetics.humaneticsgroup.com/>

Hwang, E., Hallman, J., Klein, K., Rupp, J., Reed, M., and Hu, J. (2016). "Rapid Development of Diverse Human Body Models for Crash Simulations through Mesh Morphing," in *SAE Technical Paper Series* (SAE International 400 Commonwealth Drive, Warrendale, PA, United States).

Hynd, D., Page, M., Bortenschlager, K., Been, B., van Ratingen, M., Pastor, C., et al. (2004). *Status of side impact dummy developments: WorldSID development*. Report number: EEVC WG12 doc 252.

Iwamoto, M., Nakahira, Y., and Kimpara, H. (2015). Development and Validation of the Total HUMAN Model for Safety (THUMS) Toward Further Understanding of Occupant Injury Mechanisms in Precrash and During Crash. *Traffic Inj Prev* 16 Suppl 1, 48. doi: 10.1080/15389588.2015.1015000

John, J., Klug, C., Kranjec, M., Svenning, E., and Iraeus, J. (2022). *Hello, World! VIVA+: A Human Body Model lineup to evaluate Sex-Differences in Crash Protection*.

Kato, D., Nakahira, Y., Atsumi, N., and Iwamoto, M. (2018). "Development of Human-Body Model THUMS Version 6 containing Muscle Controllers and Application to Injury Analysis in Frontal Collision after Brake Deceleration," in *2018 IRCOBI Conference Proceedings*, ed. International Research Council on the Biomechanics of Injury (IRCOBI).

- Kimpara, H., Nakahira, Y., and Iwamoto, M. (2016). Development and validation of THUMS version 5 with 1D muscle models for active and passive automotive safety research. *Conf Proc IEEE Eng Med Biol Soc* 2016, 6022–6025. doi: 10.1109/EMBC.2016.7592101
- Kitagawa, Y., and Yasuki, T. (2014). Development and Application of THUMS Version 4. *5th International Symposium: "Human Modeling and Simulation in Automotive Engineering"*.
- Kullgren, A., and Krafft, M. (2010). "Gender analysis on whiplash seat effectiveness: Results from real-world crashes," in *2010 IRCOBI Conference Proceedings*, ed. International Research Council on the Biomechanics of Injury (IRCOBI), 17–28.
- Linder, A., Davidse, R. J., Iraeus, J., John, J. D., Keller, A., Klug, C., et al. (2020). "VIRTUAL - a European approach to foster the uptake of virtual testing in vehicle safety assessment," in *Transport Research Arena*, ed. TRA, accepted.
- Livermore Software Technology Corporation (2016). *LS-DYNA Keyword User's Manual: Volume I*. LS-DYNA R9.0. Livermore, California.
- Matplotlib — *Visualization with Python* (2022). Accessed March 16, 2022.473Z, <https://matplotlib.org/>
- National Highway Traffic Safety Administration (2008). *FMVSS Test Procedure 208-14 - Appendix A: Part 572E (50th Male) Dummy Performance Calibration Test Procedure*.
- NumPy (2022). Accessed March 16, 2022.348Z, <https://numpy.org/>
- Östmann, M., and Jakobsson, L. (2016). "An Examination of Pre-crash Braking Influence on Occupant Crash Response using an Active Human Body Model," in *2016 IRCOBI Conference Proceedings*, ed. International Research Council on the Biomechanics of Injury (IRCOBI), 275–283.
- Park, G., Kim, T., Panzer, M. B., and Crandall, J. R. (2016). Validation of Shoulder Response of Human Body Finite-Element Model (GHBMC) Under Whole Body Lateral Impact Condition. *Ann Biomed Eng* 44, 2558–2576. doi: 10.1007/s10439-015-1546-6
- Protocols | Euro NCAP (2022). Accessed March 09, 2022.791Z.
- PyGeM 2.0.3 documentation (2021). Accessed March 16, 2022.489Z, <https://mathlab.github.io/PyGeM/>
- Ressi, F., Sinz, W., Geisler, C., Öztürk, A., D'Addetta, G. A., and Freienstein, H. (2019). "Estimating Preliminary Occupant Injury Risk Distributions for Highly Automated Vehicles with Respect to Future Seat Configurations and Load Directions," in *The 26th ESV Conference Proceedings*, ed. NHTSA (NHTSA).
- Safe System Principles | Road Safety Manual - World Road Association (PIARC) (2022). Accessed March 09, 2022.418Z, <https://roadsafety.piarc.org/en/road-safety-management-safe-system-approach/safe-system-principles>
- Schneider, B. (2022). Information about morphing approach. e-mail message, May 15.

Schneider, L. W., Robbins, D. H., and Pflüg, M.A., Snyder, R.G. (1983). Anthropometry of Motor Vehicle Occupants: Procedures, summary findings and appendices. *The University of Michigan - Transportation Research Institute*.

THUMS | Toyota Motor Corporation (2021). Accessed March 10, 2022.897Z,
<https://www.toyota.co.jp/thums/about/>

VIVA+ (2021). *VIVA+ Human Body Models*. Accessed March 04, 2022.677Z,
<https://vivaplus.readthedocs.io/en/latest/>

VIVA+ (2022). *Lower Extremities - VIVA+ Human Body Models*. Accessed April 11, 2022,
<https://vivaplus.readthedocs.io/en/latest/model/body-region/lower-extremities/>

WHO (2018). *Global status report on road safety 2018*. Geneva.

A APPENDIX

Table Appendix A.1-1: Apply a calculated transformation from v. 0.2.5 to v. 0.3.0 in head and neck bones	2
Table Appendix A.1-2: Apply a calculated transformation from v. 0.2.5 to v. 0.3.0 in right leg	2
Table Appendix A.1-3: Apply a calculated transformation from v. 0.2.5 to v. 0.3.0 in left leg	2
Table Appendix A.1-4: Apply a calculated transformation from v. 0.2.5 to v. 0.3.0 in right arm	2
Table Appendix A.1-5: Apply a calculated transformation from v. 0.2.5 to v. 0.3.0 in left arm.....	3
Table Appendix A.1-6: Apply a calculated transformation from v. 0.2.5 to v. 0.3.0 in thorax.....	3
Table Appendix A.1-7: Apply a calculated transformation from v. 0.2.5 to v. 0.3.0 in abdomen	3
Table Appendix A.1-8: Apply a calculated transformation from v. 0.2.5 to v. 0.3.0 in pelvis	3
Table Appendix A.1-9: Transformation for v. 0.3.0 from prev. morphed nodes in right leg	4
Table Appendix A.1-10: Transformation for v. 0.3.0 from prev. morphed nodes in left leg.....	4
Table Appendix A.1-11: Transformation for v. 0.3.0 from prev. morphed nodes in right arm.....	4
Table Appendix A.1-12: Transformation for v. 0.3.0 from prev. morphed nodes in left arm.....	5
Table Appendix A.1-13: Transformation for v. 0.3.0 from prev. morphed nodes in thorax	5
Table Appendix A.1-14: Transformation for v. 0.3.0 from prev. morphed nodes in pelvis	5
Table Appendix A.1-15: Transformation for v. 0.3.0 from prev. morphed nodes in remaining torso	6
Table Appendix A.2-1: Morphing the 50F standing baseline model 1/2.....	6
Table Appendix A.2-2: Morphing the 50F standing baseline model 2/2.....	7
Table Appendix A.2-3: Morphing the 50F seated baseline model 1/2.....	7
Table Appendix A.2-4: Morphing the 50F seated baseline model 2/2.....	8
Table Appendix A.2-5: Morphing the 50M standing baseline model	9
Table Appendix A.2-6: Morphing the 50M seated baseline model	10

A.1 Node sets and landmarks for morphing

Body regions and parts that apply the calculated transformation from v. 0.2.5:

Table Appendix A.1-1: Apply a calculated transformation from v. 0.2.5 to v. 0.3.0 in head and neck bones

Region	Landmarks for transformation in v. 0.2.5	# of landmark nodes	Baseline in v. 0.3.0	# of baseline nodes
Head bones	Surface nodes of head bones	6857	All nodes of head bones	6990
Neck bones	Surface of neck bones	12239	All nodes of Neck bones	32327

Table Appendix A.1-2: Apply a calculated transformation from v. 0.2.5 to v. 0.3.0 in right leg

Region	Landmarks for transformation in v. 0.2.5	# of landmark nodes	Baseline in v. 0.3.0	# of baseline nodes
Femur r.	Right femur surface	4243	All nodes of right femur	17945
Leg skin r.	All nodes of right leg skin	5008	All nodes of right leg skin	8939
Fibula head r.	Surface of right Fibula	2522	All Nodes of right Fibula head	1255
Tibia head r.	Surface of right Tibia	2826	All Nodes of right Tibia head	2124
Patella r.	Surface of right Patella	182	All nodes of right Patella	435
LX soft Knee r.	All nodes of right LX soft knee	1001	All nodes of right LX soft knee	917

Table Appendix A.1-3: Apply a calculated transformation from v. 0.2.5 to v. 0.3.0 in left leg

Region	Landmarks for transformation in v. 0.2.5	# of landmark nodes	Baseline in v. 0.3.0	# of baseline nodes
Femur l.	Left femur surface	4243	All nodes of left femur	17945
Leg skin l.	All nodes of left leg skin	5007	All nodes of left leg skin	8939
Fibula head l.	Surface of left Fibula	2522	All Nodes of left Fibula head	1255
Tibia head l.	Surface of left Tibia	2826	All Nodes of left Tibia head	2124
Patella l.	Surface of left Patella	182	All nodes of left Patella	435
LX soft Knee l.	All nodes of left LX soft knee	1001	All nodes of left LX soft knee	917

Table Appendix A.1-4: Apply a calculated transformation from v. 0.2.5 to v. 0.3.0 in right arm

Region	Landmarks for transformation in v. 0.2.5	# of landmark nodes	Baseline in v. 0.3.0	# of baseline nodes
Right arm skin	All nodes of right arm skin + nodes from torso skin	6191	Right arm skin without torso connection skin and partial lower arm skin nodes	3992
Clavicle Scapula r.	Surface nodes of right clavicle and scapula	3642	All nodes of right clavicle and scapula	5176
Humerus r.	Surface nodes of right Humerus	2566	All nodes of right Humerus	7837
Ulna Radius r.	Surface nodes of right Ulna and Radius + prev. morphed nodes of wrist skin	2423	All nodes of right Ulna and Radius	7618

Table Appendix A.1-5: Apply a calculated transformation from v. 0.2.5 to v. 0.3.0 in left arm

Region	Landmarks for transformation in v. 0.2.5	# of landmark nodes	Baseline in v. 0.3.0	# of baseline nodes
Left arm skin	All nodes of left arm skin	6043	Left arm skin without torso connection skin and partial lower arm skin nodes	3840
Clavicle Scapula l.	Surface nodes of left clavicle and scapula	3644	All nodes of left clavicle and scapula	5176
Humerus l.	Surface nodes of left Humerus	2622	All nodes of left Humerus	7839
Ulna Radius l.	Surface nodes of left Ulna and Radius + prev. morphed nodes of wrist skin	2423	All nodes of left Ulna and Radius	7618

Table Appendix A.1-6: Apply a calculated transformation from v. 0.2.5 to v. 0.3.0 in thorax

Region	Landmarks for transformation in v. 0.2.5	# of landmark nodes	Baseline in v. 0.3.0	# of baseline nodes
Thorax vertebra bones	Surface nodes of thorax vertebra bones	6703	All nodes of thorax vertebra bones	10321
Right R1 to R6 bones	Surface nodes of right R1 to R6 rib bones	8336	All nodes of right R1 to R6 rib bones	12432
Right R7 to R12 bones	Surface nodes of right R7 to R12 rib bones	8864	All nodes of right R7 to R12 rib bones	13224
Left R1 to R6 bones	Surface nodes of left R1 to R6 rib bones	8336	All nodes of left R1 to R6 rib bones	12431
Left R7 to R12 bones	Surface nodes of left R7 to R12 rib bones	8864	All nodes of left R7 to R12 rib bones	13224
Thorax sternum bone	Surface nodes of sternum bone	2158	All nodes of sternum bone	4162

Table Appendix A.1-7: Apply a calculated transformation from v. 0.2.5 to v. 0.3.0 in abdomen

Region	Landmarks for transformation in v. 0.2.5	# of landmark nodes	Baseline in v. 0.3.0	# of baseline nodes
Abdomen vertebra bones	Surface nodes of abdomen vertebra bones	3575	All nodes of abdomen vertebra bones	6450

Table Appendix A.1-8: Apply a calculated transformation from v. 0.2.5 to v. 0.3.0 in pelvis

Region	Landmarks for transformation in v. 0.2.5	# of landmark nodes	Baseline in v. 0.3.0	# of baseline nodes
Pelvic bones r.	Surface of right pelvic bones	5306	All Nodes of right pelvic bones + connections	14912
Pelvic bones l.	Surface of left pelvic bones	5316	All Nodes of left pelvic bones + connections	14788
Hip Ligament r.	All nodes of right hip ligament	428	All nodes of right hip ligament	380
Hip Ligament l.	All nodes of left hip ligament	404	All nodes of left hip ligament	380

Body regions and parts that calculate the transformation directly in v. 0.3.0:

Table Appendix A.1-9: Transformation for v. 0.3.0 from prev. morphed nodes in right leg

Region	Landmarks for transformation in v 0.3.0	# of landmark nodes from prev. morphed	Baseline in v. 0.3.0	# of baseline nodes
Foot with ankle r.	Prev. morphed nodes of right leg skin	1487	All nodes of right foot + lower ends of tibia and fibula	5092 (3605 remaining)
Fibula r.	Prev. morphed nodes of upper and lower ends of Fibula	1445	All Nodes of right Fibula	8467 (7022 remaining)
Tibia r.	Prev. morphed nodes of upper and lower ends of Tibia	2310	All Nodes of right Tibia	8875 (6565 remaining)
LX Ankle Soft r.	Prev. morphed nodes of right foot, Tibia, Fibula and leg skin.	1559	All nodes of right LX Ankle soft	2176 (617 remaining)
Lower right leg	All prev. morphed surface-nodes of right lower leg	9593	All nodes of remaining right lower leg	31706 (22113 remaining)
Upper right leg	All prev. morphed surface-nodes of right upper leg	4883	All nodes of remaining right upper leg	17203 (12320 remaining)

Table Appendix A.1-10: Transformation for v. 0.3.0 from prev. morphed nodes in left leg

Region	Landmarks for transformation in v 0.3.0	# of landmark nodes from rev. morphed	Baseline in v. 0.3.0	# of baseline nodes
Foot with ankle l.	Prev. morphed nodes of left leg skin	1487	All nodes of left foot + lower ends of tibia and fibula	5100 (3613 remaining)
Fibula l.	Prev. morphed nodes of upper and lower ends of Fibula	1462	All Nodes of left Fibula	8467 (7005 remaining)
Tibia l.	Prev. morphed nodes of upper and lower ends of Tibia	2262	All Nodes of left Tibia	8837 (6575 remaining)
LX Ankle Soft l.	Prev. morphed nodes of left foot, Tibia, Fibula and leg skin.	1559	All nodes of left LX Ankle soft	2176 (617 remaining)
Lower left leg	All prev. morphed surface-nodes of left lower leg	9523	All nodes of remaining left lower leg	31555 (22032 remaining)
Upper left leg	All prev. morphed surface-nodes of left upper leg	4748	All nodes of remaining left upper leg	17219 (12471 remaining)

Table Appendix A.1-11: Transformation for v. 0.3.0 from prev. morphed nodes in right arm

Region	Landmarks for transformation in v 0.3.0	# of landmark nodes from rev. morphed	Baseline in v. 0.3.0	# of baseline nodes
Right arm skin Torso connection	Prev. morphed nodes of right arm skin and torso skin	268	Remaining nodes of right arm skin	371 (103 remaining)
Right hand	Prev. morphed nodes of right arm skin	1656	All nodes of right hand	5588 (3932 remaining)
Right lower arm skin	Prev. morphed nodes of right arm skin, ulna and radius	3027	All nodes of right lower arm skin	3567 (540 remaining)
Remaining right arm	Prev. morphed nodes of right arm	7933	All remaining nodes of right arm	17284 (9351 remaining)

Table Appendix A.1-12: Transformation for v. 0.3.0 from prev. morphed nodes in left arm

Region	Landmarks for transformation in v 0.3.0	# of landmark nodes from rev. morphed	Baseline in v. 0.3.0	# of baseline nodes
Left arm skin Torso connection	Prev. morphed nodes of left arm skin and torso skin	222	Remaining nodes of left arm skin	369 (147 remaining)
Left hand	Prev. morphed nodes of left arm skin	1656	All nodes of left hand	5588 (3932 remaining)
Left lower arm skin	Prev. morphed nodes of left arm skin, ulna and radius	2892	All nodes of left lower arm skin	3432 (540 remaining)
Remaining left arm	Prev. morphed nodes of left arm	8006	All remaining nodes of left arm	17487 (9481 remaining)

Table Appendix A.1-13: Transformation for v. 0.3.0 from prev. morphed nodes in thorax

Region	Landmarks for transformation in v 0.3.0	# of landmark nodes from rev. morphed	Baseline in v. 0.3.0	# of baseline nodes
Thorax ribcage external r.	Prev. morphed nodes of right ribs	404	All nodes of ribcage cartilage external r.	5312 (4908 remaining)
Thorax ribcage external l.	Prev. morphed nodes of left ribs	404	All nodes of ribcage cartilage external l.	5312 (4908 remaining)
Right intercostal muscles	Prev. morphed nodes of right side thorax bones (without skin)	9440	All nodes of right side intercostal muscles	24862 (15422 remaining)
Left intercostal muscles	Prev. morphed nodes of left side thorax bones (without skin)	9740	All nodes of left side intercostal muscles	24863 (15123 remaining)

Table Appendix A.1-14: Transformation for v. 0.3.0 from prev. morphed nodes in pelvis

Region	Landmarks for transformation in v 0.3.0	# of landmark nodes from rev. morphed	Baseline in v. 0.3.0	# of baseline nodes
Pelvic Cavity	Prev. morphed node of pelvic bones	7741	All nodes of Pelvic cavity	22560 (14819 remaining)
Pelvis Connect Null r.	Prev. morphed nodes of pelvic and right femur bone + hip ligament	996	All nodes of pelvis connect null r.	1092 (96 remaining)
Pelvis Connect Null l.	Prev. morphed nodes of pelvic and left femur bone + hip ligament	1026	All nodes of pelvis connect null l.	1122 (96 remaining)
Pelvis soft tissue internals r.	Prev. morphed nodes of pelvic bones of right side	5010	All nodes of pelvic soft tissue internal null r.	5768 (758 remaining)
Pelvis soft tissue internals l.	Prev. morphed nodes of pelvic bones of left side	4778	All nodes of pelvic soft tissue internal null l.	5499 (721 remaining)
Pelvic soft tissue r.	Prev. morphed nodes of Pelvis	4377	Remaining nodes of pelvic soft tissue r.	11701 (7324 remaining)
Pelvic soft tissue l.	Prev. morphed nodes of Pelvis	4145	Remaining nodes of pelvic soft tissue l.	11288 (7143 remaining)

Table Appendix A.1-15: Transformation for v. 0.3.0 from prev. morphed nodes in remaining torso

Region	Landmarks for transformation in v 0.3.0	# of landmark nodes from rev. morphed	Baseline in v. 0.3.0	# of baseline nodes
Thorax soft tissue r.	Prev. morphed nodes of thorax	17364	Remaining nodes of thorax soft r.	23371 (6007 remaining)
Thorax soft tissue l.	Prev. morphed nodes of thorax	17462	Remaining nodes of thorax soft l.	23309 (5667 remaining)
Abdominal cavity l.	Prev. morphed nodes of thorax	2327	Remaining nodes of abdominal cavity l.	22690 (20363 remaining)
Abdominal cavity r.	Prev. morphed nodes of thorax	2312	Remaining nodes of abdominal cavity r.	21925 (19613 remaining)

A.2 Detailed morphing results

Table Appendix A.2-1: Morphing the 50F standing baseline model 1/2

Criteria	Baseline model	Morphed model	Morphed model
	50F standing positive x	50M standing negative x	50M standing positive x - rotated
Morphing parameters	-	RBF, func_added, r=0.1	RBF, func_added, r=0.1
Solid elem. with neg. volume	0	53 Total 69 Partial	53 Total 69 Partial
Solid OFF-elements			
Aspect ratio	-	115 (0.022%)	115 (0.022%)
Warping	-	123 (0.023%)	123 (0.023%)
Skewness	-	499 (0.095%)	499 (0.095%)
Jacobian	-	91 (0.017%)	91 (0.017%)
Tetras angle off	-	111 (0.021%)	111 (0.021%)
Pentas angle off	-	8 (0.002%)	8 (0.002%)
Hexas angle off	-	674 (0.129%)	705 (0.135%)
Total solids off	0	951 (0.182%)	964 (0.184%)
Shell OFF-elements			
Aspect	-	12 (0.005%)	12 (0.005%)
Skewness	-	24 (0.010%)	24 (0.010%)
Warping	-	13 (0.005%)	13 (0.005%)
Jacobian	-	2 (0.001%)	2 (0.001%)
Quads angle off	-	3 (0.001%)	3 (0.001%)
Trias angle off	-	12 (0.005%)	12 (0.005%)
Total shells off	0	50 (0.020%)	50 (0.020%)
Mass	62.57 kg (v. 0.3.0)	73.67 kg (v. 0.2.5) target 79.34 kg	73.67 kg (v. 0.2.5) target 79.34 kg
Intrusions	no	See Figure 30 (a). Knee LX-Soft posterior.	See Figure 30 (a). Knee LX-Soft posterior.

Table Appendix A.2-2: Morphing the 50F standing baseline model 2/2

Criteria	Baseline model	Morphed model	Morphed model
	50F standing	50F cyclist left leg down	50F TB024 Pedestrian
Morphing parameters	-	RBF, func_added, r=0.1	RBF, func_added, r=0.1
Solid elem. with neg. volume	0	57 Total 223 Partial	7 Total 38 Partial
Solid OFF-elements			
Aspect ratio	-	485 (0.093%)	57 (0.011%)
Warping	-	347 (0.066%)	52 (0.012%)
Skewness	-	834 (0.159%)	270 (0.052%)
Jacobian	-	355 (0.068%)	70 (0.013%)
Tetras angle off	-	0 (0.000%)	0 (0.000%)
Pentas angle off	-	16 (0.003%)	2 (0.000%)
Hexas angle off	-	2265 (0.433%)	613 (0.117%)
Total solids off	0	2123 (0.405%)	605 (0.116%)
Shell OFF-elements			
Aspect	-	56 (0.023%)	1 (0.000%)
Skewness	-	66 (0.027%)	5 (0.002%)
Warping	-	41 (0.017%)	4 (0.002%)
Jacobian	-	17 (0.007%)	2 (0.001%)
Quads angle off	-	77 (0.031%)	5 (0.002%)
Trias angle off	-	3 (0.001%)	0 (0.000%)
Total shells off	0	158 (0.065%)	12 (0.005%)
Mass	62.57 kg (v. 0.3.0)	62.37 kg (v. 0.2.5 target 59.71 kg)	61.05 kg (v. 0.2.5 target 60.59 kg)
Intrusions	no	See Figure 31. Knee LX-soft anterior (a), pelvis cranial (b), humerus posterior (c)	See Figure 30 (b). Knee LX-soft anterior

Table Appendix A.2-3: Morphing the 50F seated baseline model 1/2

Criteria	Baseline model	Morphed model	Morphed model
	50F seated	50M seated	50F cyclist left leg down
Morphing parameters	-	RBF, func_added, r=0.1	RBF, func_added, r=0.1
Solid elem. with neg. volume	0	0 Total 3 Partial	13 Total 93 Partial
Solid OFF-elements			
Aspect ratio	-	80 (0.015%)	484 (0.092%)
Warping	-	28 (0.005%)	112 (0.021%)
Skewness	-	44 (0.008%)	816 (0.156%)
Jacobian	-	11 (0.002%)	189 (0.036%)
Tetras angle off	-	8 (0.002%)	14 (0.003%)
Pentas angle off	-	8 (0.002%)	16 (0.003%)
Hexas angle off	-	189 (0.036%)	2060 (0.393%)
Total solids off	0	284 (0.054%)	1882 (0.359%)
Shell OFF-elements			
Aspect	-	10 (0.004%)	60 (0.025%)
Skewness	-	9 (0.004%)	62 (0.025%)
Warping	-	16 (0.007%)	16 (0.007%)
Jacobian	-	1 (0.000%)	13 (0.005%)
Quads angle off	-	4 (0.002%)	62 (0.025%)
Trias angle off	-	4 (0.002%)	3 (0.001%)
Total shells off	0	36 (0.015%)	152 (0.062%)
Mass	62.15 kg (v. 0.3.0)	72.20 kg (v. 0.2.5 target 73.98 kg)	65.32 kg (v. 0.2.5 target 59.71 kg)
Intrusions	no	no	See Figure 33. Knee LX-soft anterior (a), pelvis cranial (b), humerus posterior (c)

Table Appendix A.2-4: Morphing the 50F seated baseline model 2/2

Criteria	Baseline model	Morphed model	Morphed model
	50F seated	50F TB024 Pedestrian	50F Standing
Morphing parameters	-	RBF, func_added, r=0.1	RBF, func_added, r=0.1
Solid elem. with neg. volume	0	225 Total 387 Partial	4 Total 52 Partial
Solid OFF-elements			
Aspect ratio	-	86 (0.016%)	22 (0.004%)
Warping	-	86 (0.016%)	46 (0.009%)
Skewness	-	650 (0.124%)	87 (0.017%)
Jacobian	-	502 (0.096%)	87 (0.017%)
Tetras angle off	-	15 (0.003%)	15 (0.003%)
Pentas angle off	-	1 (0.000%)	0 (0.000%)
Hexas angle off	-	3123 (0.596%)	607 (0.116%)
Total solids off	0	1784 (0.341%)	399 (0.076%)
Shell OFF-elements			
Aspect	-	26 (0.011%)	43 (0.018%)
Skewness	-	23 (0.009%)	0 (0.000%)
Warping	-	17 (0.007%)	14 (0.006%)
Jacobian	-	7 (0.003%)	4 (0.002%)
Quads angle off	-	22 (0.009%)	4 (0.002%)
Trias angle off	-	0 (0.000%)	0 (0.000%)
Total shells off	0	70 (0.029%)	59 (0.024%)
Mass	62.15 kg (v. 0.3.0)	60.96 kg (v. 0.2.5 target 60.59 kg)	59.80 kg (v. 0.2.5 target 62.57 kg)
Intrusions	no	See Figure 34. Left lower leg anterior (a), left lower arm posterior (b), LX soft knee both sides anterior (c), LX-Soft pelvic connect anterior (d)	See Figure 35. Humerus both sides anterior, LX-Soft pelvic connect anterior

Table Appendix A.2-5: Morphing the 50M standing baseline model

Criteria	Baseline model	Morphed model	Morphed model	Morphed model
	50M standing	50F standing	50M TB024 pedestrian	50M cyclist left leg down
Morphing parameters	-	RBF, func_added, r=0.1	RBF, func_added, r=0.1	RBF, func_added, r=0.1
Solid elem. with neg. volume	0	83 Total 101 Partial	45 Total 54 Partial	134 Total 295 Partial
Solid OFF-elements				
Aspect Ratio	-	73 (0.014%)	87 (0.017%)	282 (0.054%)
Warping	-	112 (0.021%)	96 (0.018%)	479 (0.091%)
Skewness	-	366 (0.070%)	372 (0.071%)	915 (0.175%)
Jacobian	-	147 (0.028%)	84 (0.016%)	492 (0.094%)
Tetras angle off	-	142 (0.027%)	167 (0.032%)	1 (0.00%)
Pentas angle off	-	24 (0.005%)	1 (0.000%)	1 (0.00%)
Hexas angle off	-	482 (0.092%)	369 (0.076%)	2379 (0.454%)
Total solids off	0	793 (0.151%)	796 (0.152%)	2368 (0.452%)
Shell OFF-elements				
Aspect	-	41 (0.017%)	42 (0.017%)	83 (0.034%)
Skewness	-	41 (0.017%)	21 (0.009%)	63 (0.026%)
Warping	-	21 (0.009%)	14 (0.006%)	34 (0.014%)
Jacobian	-	1 (0.000%)	12 (0.005%)	14 (0.006%)
Quads angle off	-	17 (0.007%)	24 (0.010%)	70 (0.029%)
Trias angle off	-	34 (0.014%)	31 (0.013%)	2 (0.001%)
Total shells off	0	113 (0.046%)	98 (0.040%)	191 (0.078%)
Mass	79.34 kg (v. 0.3.0)	62.54 kg (v. 0.2.5 target 62.57 kg)	74.22 kg (v. 0.2.5 target 71.00 kg)	75.07 kg (v. 0.2.5 target 70.48 kg)
Intrusions	no	See Figure 37. Pelvic soft tissue anterior (a), scapula posterior (b)	See Figure 38. Pelvic soft tissue anterior (a), LX soft knee left sides anterior (b)	See Figure 39. LX soft knee right side and pelvic soft tissue anterior (a), LX-Soft pelvis connect posterior and pelvis cranial (b)

Table Appendix A.2-6: Morphing the 50M seated baseline model

Criteria	Baseline model	Morphed model	Morphed model	Morphed model
	50M seated	50F seated	50M TB024 pedestrian	50M cyclist left leg down
Morphing parameters	-	RBF, func_added, r=0.1	RBF, func_added, r=0.1	RBF, func_added, r=0.1
Solid elem. with neg. volume	0	20 Total 78 Partial	1368 Total 1596 Partial	1691 Total 2005 Partial
Solid OFF-elements				
Aspect ratio	-	13 (0.002%)	449 (0.086%)	527 (0.101%)
Warping	-	49 (0.009%)	163 (0.031%)	274 (0.053%)
Skewness	-	383 (0.073%)	2468 (0.471%)	1711 (0.327%)
Jacobian	-	109 (0.021%)	1736 (0.332%)	2176 (0.416%)
Tetras angle off	-	3 (0.001%)	968 (0.185%)	243 (0.046%)
Pentas angle off	-	32 (0.006%)	4 (0.001%)	1 (0.000%)
Hexas angle off	-	692 (0.132%)	4923 (0.94%)	5319 (1.016%)
Total solids off	0	631 (0.121%)	5295 (1.011%)	4584 (0.876%)
Shell OFF-elements				
Aspect	-	64 (0.026%)	46 (0.019%)	79 (0.032%)
Skewness	-	31 (0.013%)	46 (0.019%)	101 (0.041%)
Warping	-	16 (0.007%)	13 (0.005%)	26 (0.011%)
Jacobian	-	2 (0.001%)	5 (0.002%)	3 (0.001%)
Quads angle off	-	20 (0.008%)	25 (0.010%)	55 (0.022%)
Trias angle off	-	2 (0.001%)	97 (0.040%)	37 (0.015%)
Total shells off	0	113 (0.046%)	180 (0.074%)	213 (0.087%)
Mass	77.15 kg (v. 0.3.0)	72.20 kg (v. 0.2.5 target 73.98 kg)	74.22 kg (v. 0.2.5 target 71.00 kg)	73.08 kg (v. 0.2.5 target 70.48 kg)
Intrusions	no	See Figure 41. LX soft knee both sides anterior (a), clavicle and R2 rib bone anterior (b)	See Figure 42. Tibia both sides anterior and LX-Soft pelvis connect anterior (a), humerus anterior (b), clavicle anterior (c)	See Figure 43. Tibia both sides anterior (a), LX soft knee both sides anterior (b), humerus posterior (c)